Utilization of Computational Techniques in the Development of Functional Materials

by

Marisa E. Gliege

A Dissertation Presented in Partial Fulfillment
of the Requirements for the Degree
Doctor of Philosophy

Approved July 2021 by the
Graduate Supervisory Committee:

Lenore Dai, Co-Chair
Agnes Derecskei-Kovacs, Co-Chair
Heather Emady
Christopher Muhich
Houlong Zhuang

ARIZONA STATE UNIVERSITY

August 2021

ABSTRACT

Functional materials can be characterized as materials that have tunable properties and are attractive solutions to the improvement and optimization of processes that require specific physiochemical characteristics. Through tailoring and altering these materials, their characteristics can be fine-tuned for specific applications. Computational modeling proves to be a crucial methodology in the design and optimization of such materials. This dissertation encompasses the utilization of molecular dynamics simulations and quantum calculations in two fields of functional materials: electrolytes and semiconductors.

Molecular dynamics (MD) simulations were performed on ionic liquid-based electrolyte systems to identify molecular interactions, structural changes, and transport properties that are often reflected in experimental results. The simulations aid in the development process of the electrolyte systems in terms of concentrations of the constituents and can be invoked as a complementary or predictive tool to laboratory experiments. The theme of this study stretches further to include computational studies of the reactivity of atomic layer deposition (ALD) precursors. Selected aminosilane-based precursors were chosen to undergo density functional theory (DFT) calculations to determine surface reactivity and viability in an industrial setting. The calculations were expanded to include the testing of a semi-empirical tight binding program to predict growth per cycle and precursor reactivity with a high surface coverage model. Overall, the implementation of computational methodologies and techniques within these applications improves materials design and process efficiency while streamlining the development of new functional materials.

DEDICATION

To My Grandfather, Hervin E. Gliege

For his love, caring spirit, and appreciation

ACKNOWLEDGEMENTS

This dissertation would not be possible without the guidance from Dr. Lenore Dai and Dr. Agnes Derecskei. Dr. Dai, I cannot thank you enough for picking me to join your lab, pushing me to be the best researcher I can be, and showing compassion and caring for me as a person. Dr. Derecskei, although you became a co-chair halfway through my PhD study, your role has been tremendous. Thank you for taking an interest in me, helping me tap into my potential as a researcher and become a well-rounded scientist. I would also like to thank my committee members Dr. Heather Emady, Dr. Christopher Muhich, and Dr. Houlong Zhuang.

None of this would be possible without my wonderful lab mates, Dr. Yifei Xu, Wendy Lin, Dr. Ryan Gunckel, Mu-Tao Chen, and Christopher Whitney. Specifically, I'd like to thank Dr. Yifei Xu who never ran out of project ideas and taught me how to be a better writer by reading all of my rough drafts, and Wendy Lin who has a wealth of knowledge and is a delight to spend hours in lab with. I'd also like to thank Taylor Davis, my best friend in graduate school who was my support system and got coffee with me when I needed a break.

I want to thank my family and friends who have been incredibly supportive through my academic career. I chose to become a chemical engineer when I was 16. I moved across the state of Washington to pursue my Bachelors degree, before moving to Arizona to pursue my Ph.D. My family has been there every step of the way and supportive of my decisions, despite being farther in life and taking care of their own families. I want to specially thank my mom, Madeline Gliege. My selfless mother helped me move around

the U.S. for all my internships and first days at new universities for the past 8 years. She has been my cheerleader and always taken an interest in what I am doing. I love you, mom.

To my close friends, thank you for sticking by my side and being there for me. I know it has been a long road, but your encouragement and support has kept me going. I could not have finished this journey without you.

Finally, I owe a huge thank you to my wonderful, loving, kind, compassionate, and incredible fiancé, Patrick O'Leske. Patrick, you have been there for me through almost all my PhD study. You have celebrated my achievements and comforted me through my failures and frustrations. Thank you, my love.

Deciding to pursue a Ph.D. is no small decision. My Ph.D. has been filled with countless twists and turns and through all of it I have always had these people to support me. I very much look forward to passing that support along in my career the same way it has been given to me.

I would like to acknowledge the financial support that made all of this possible. Specifically, the National Aeronautics and Space Administration, grant number NNX17AF70G, Arizona State University's Dean's Fellowship Award, and the EMD Electronics Graduate Fellowship. Thank you to Arizona State University's Research Computing team for the use of high performance computing (HPC), storage, etc. resources that were used in this dissertation. In addition, I would like to thank Dr. Christopher Muhich, Dr. Stella Nickerson, and Dr. Michal Krompiec for their input and discussion on my research.

TABLE OF CONTENTS

Page

CHAPTER Page

CHAPTER Page

LIST OF TABLES

Table Page

LIST OF FIGURES

Figure Page

Figure Page

Figure Page

Figure Page

Figure Page

CHAPTER
1. INTRODUCTION

Functional materials are a specific class of materials that respond to a form of stimuli and encompass attractive properties for purposes within a variety of fields including semiconductors, ceramics, polymers, and energy storage.[1,2,11–13,3–10] Through experimental and computational methodologies, functional materials can be altered such that their physiochemical characteristics become highly desirable for their specific applications. The challenges associated with such modifications can make it difficult for researchers and scientists to successfully create working materials, however advancements from the past decades have furthered our knowledge and abilities to create cutting-edge functional materials.

Due to the complexity and tunability of functional materials, computational techniques are commonly employed to further understand the quantum, atomistic, and molecular characteristics of such materials. By combining experimental and computational approaches, functional materials are optimized and modified to fit their designated operations.[14–20] Innovation within these fields continues today as computational methods and programs are improved upon.[21–25]

In this dissertation prospectus, we explore the fundamental properties of functional materials including ionic liquids and their mixtures for applications in extreme environments and the reactivity of aminosilane precursors with an SiO_2 surface in the context of atomic layer deposition. While these topics are not inherently related, the encompassing theme is the use of computational chemistry to model the systems to gain a better understanding and optimize them for scale up engineering and design.

The first project investigates properties of electrolyte mixtures and method development of glass transition temperature predictions in neat ionic liquids. Our interest in ionic liquids and electrolyte mixtures stems from the need for customizable electrolyte mixtures in devices for energy storage and even planetary exploration.[26–33] The second project explores a variety of aminosilane precursor candidates for ALD on an SiO_2 (1 0 0) surface. This project lies in the interest of EMD Electronics, where ALD precursors are developed and screened for various ALD applications within the semiconductor industry.

The following describes each chapter of the dissertation prospectus: Chapter 1 details the importance of computational methods in materials development, briefly outlines multiscale modeling, and goes into the physical theory behind computational techniques utilized in this prospectus. Chapter 2 introduces the ionic liquids and electrolyte mixtures that are further explored in later chapters. Atomic layer deposition is also introduced and expanded on. Chapter 2 encompasses the motivations behind studying these selected functional materials. Chapter 3 outlines the methods used to carry out various simulations and calculations of ionic liquids and ALD reactions. Chapter 4 reports all the results from the projects and discusses their significance. Chapter 5 summarizes the work that has been done thus far and lastly, chapter 6 proposes work to further projects, or even branch off them.

1.1 Role of Computational Chemistry Techniques in Materials Development

The design of functional materials encompasses the multiscale methodologies involved with creating and improving chemical and physical processes that enhance industries such as semiconductors, pharmaceuticals, etc. It is without question that computational techniques have greatly enhanced the progress of research and development when it comes to materials design.[34,35,44–50,36–43] Moreover, these techniques continue to improve in capability, accuracy, and computing time. Specifically, computational chemistry in the context of materials design is crucial to the timeliness of the development and to our capability to gain direct insight into the properties and behavior of such materials to contribute to their advancement. For example, density functional theory (DFT) calculations can predict reaction energies and activation energies of reaction pathways

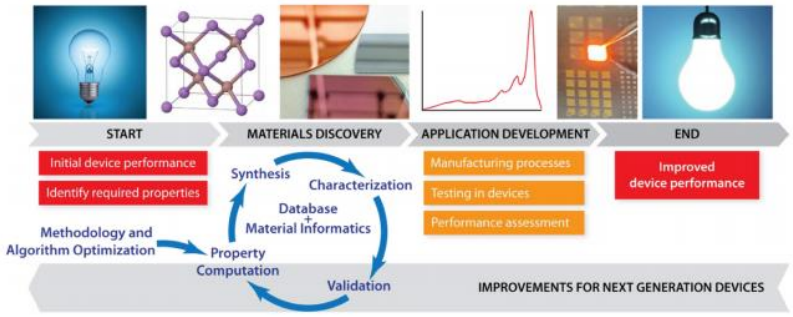

Figure 1.1.1 Materials Design Flow Chart Cycle

involved in reactions e.g during thin film deposition as seen in the semiconductor industry , or in batteries used for energy storage, and in uncountable industrial processes.[51,52] One of the all-encompassing themes of these calculations, further explored in this dissertation, is the capability of describing quantum, atomistic, and molecular level events and utilize them to understand how the larger scale behavior and material properties are changed.

When it comes to innovation in materials design, it is greatly dependent on the intertwining and harmony of experimental and computational work. To validate theoretical

calculations, pertinent experimental studies are required. Figure 1.2.1[53] shows a schematic view of how these two methods rely on each other for the improvement of materials design processes. The computational approaches are always based on simplified and idealized models. They usually focus on property calculations which comes from computational methodology and computer codes that have been optimized specifically for those property calculations. In order to improve the models or encompass the ability to calculate other necessary properties, there is a reliance on experimental work both in the model development and the validation of the computational results. Ultimately, an iterative cycle is created when computational and experimental techniques work in harmony which ideally results in better materials, improved manufacturing processes, optimized devices and improved overall performances.

Recent developments in the high-performance computing, machine learning, and artificial intelligence communities have aided to further computational chemistry capabilities. Calculations that have been traditionally computationally expensive are now less taxing through increased computation time and methods to circumvent traditional roadblock. For example, quantum chemistry codes are being optimized to run more efficiently and thus more quickly. Furthermore, machine learning-based codes are working to make calculations increasingly accurate and even more reliable. As these technologies are advancing further, it becomes our responsibility to find ways to stay up to date and continue to innovate.

1.2 Multiscale Modeling

Computational techniques can range from nanoscale quantum mechanics-based calculations to large scale process simulations. The process starts with identifying a desired property to be computed and from there, the computational technique can be chosen. For functional materials design, where the overall goal is to tune material properties or

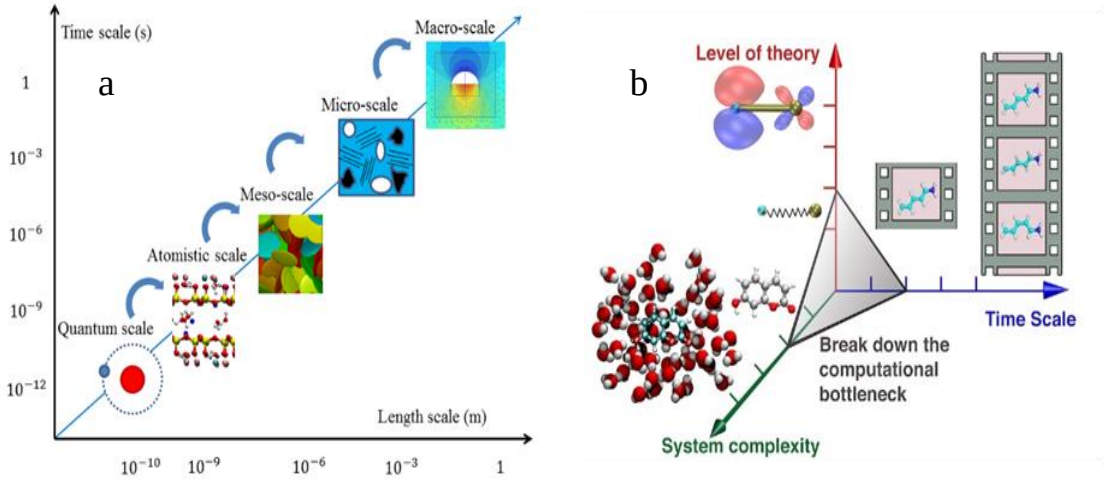

Figure 1.2.1 MultiScale Modeling (a) Quantum calculation considerations. (b) Multiscale Modeling Levels

processes, the computational capabilities lie all scales of modeling. Figure1.2.1 (a)[54] shows different levels of computation. Quantum scale calculations are limited to a few hundred atoms, while atomistic (force field) calculations often have tens of thousands of atoms. Micro-scale and macro-scale calculations are utilized to simulate large systems such as distillation columns, reactors, and processing systems. Figure 1.3.1 (b)[55] demonstrates how increasing the level of theory or system complexity of quantum scale computing will also affect the time scale of the calculations. As the system gets more complex, accuracy is increased, and time scale is increased, thus the time to complete the calculations will also increase. When approaching problems, computational resources such as complexity and time are often considered to design a method to solve the problem.

The computational methods utilized in this study are quantum and atomistic. Each method is different in terms of its capabilities to treat system sizes, yield calculable properties, and inherent accuracy. For example, molecular dynamics can be used to identify molecular interactions within ionic liquid mixture systems that may contribute to bulk properties observed in experimental results while DFT calculations would focus on a single ionic liquid ion pair. However, some parameters or results from each method can be propagated between different levels of modeling. Force field parameters used in molecular dynamics simulations are often derived from *ab-initio* or DFT calculations to simulate accurate intra and intermolecular interactions.

Determining appropriate computational modeling resources depends on availability and desired results. Having multiple approaches with different levels of computation allows for multiple pathways to solve a problem. In the context of functional materials, multiscale modeling provides "building blocks" for large scale computations that is crucial to materials design.

In this dissertation, there are three scales of modeling utilized for two types of functional materials. The smallest scale, quantum-based calculations, were performed on organosilane molecules to evaluate the reaction mechanisms and thermodynamics for atomic layer deposition within semiconductor manufacturing. Semi-empirical tight binding calculations were performed on the reaction surfaces containing ~1000 atoms, putting this scale more towards the atomistic side. Larger scale calculations containing tens of thousands of atoms were utilized for ionic liquids systems to derive structure-property relationships through identifying molecular mechanisms and validating through experiments. Semi-empirical tight binding calculations were also performed on smaller

ionic liquid systems to explore the expansion of computational method capabilities within the ionic liquid community.

1.3 Physical Theory Behind Computational Methods

Quantum mechanics can be defined, in general, as the starting point of microscale calculations that describe atomistic systems. The qualitative property paramount to quantum mechanics is the description of electrons and nuclei as particles with wave-like motion. In the world of computational chemistry, this relationship is better known as the Schrodinger's equation. This section of the dissertation will go into brief details of the expansion of the Schrodinger equation and how it progressed into well-known methods used today such as *ab-initio*, DFT, Semi-Empirical, and, indirectly, Molecular Mechanics methods. The following equations and concepts are explained in more details in the references.[56–65]

Schrodinger Equation

The time independent Schrodinger equation,

$$H\Psi = E\Psi \qquad \text{Eqn. 1.3.1}$$

states that for the Hamiltonian (an operator which is the sum of the kinetic and potential energies in the system) there is an eigenfunction, Ψ, (the wave function) that is equal to the eigenvalue, E, times the wave function. By knowing the Hamiltonian and having a method of solving for the eigenfunction and eigenvalue, we can then calculate and predict the system behavior.

For a system of electrons and nuclei, the Hamiltonian operator, H, breaks up the total energy into parts.

$$\hat{H} = -\sum_{A}^{nuc} \frac{\hbar^2}{2M_A} \nabla_A^2 - \sum_{i}^{elec} \frac{\hbar^2}{2m} \nabla_i^2 - \sum_{A}^{nuc} \sum_{i}^{elec} \frac{e^2 Z_A}{4\pi\epsilon_0 r_{Ai}} + \sum_{A>B}^{nuc} \frac{Z_A Z_B e^2}{4\pi\epsilon_0 R_{AB}} + \sum_{i>j}^{elec} \frac{e^2}{4\pi\epsilon_0 r_{ij}} \quad \text{Eqn. 1.3.2}$$

Eqn. 1.3.2 is the molecular Hamiltonian where the first term is the nucleus kinetic energy, the second term is the electronic kinetic energy, the third term is the electron-nucleus attraction, the fourth term is the nucleus-nucleus repulsion and the last term is the electron-electron repulsion.

While the Schrodinger equation can be explicitly solved for systems with one electron, it can be applied to systems with more electrons, however it will need to be approximated. Ultimately, solving the electronic Schrodinger equation gives a structure than can then be used to create a potential energy surface. From the potential energy surface, equilibrium geometries, vibrational frequencies, reaction mechanisms, transition states, and more can be calculated. Dipole moments and such can be calculated from the electronic wave function. In order to set up the Schrodinger equation, the Hamiltonian is rewritten from a molecular based equation to an electronic based equation, shown in Eqn. 1.3.3. While Eqn. 1.3.4 is the simplified version of the terms.

$$\hat{H} = -\sum_{A}^{nuc} \frac{1}{2M_A} \nabla_A^2 - \frac{1}{2} \sum_{i}^{elec} \nabla_i^2 - \sum_{A}^{nuc} \sum_{i}^{elec} \frac{Z_A}{r_{Ai}} + \sum_{A>B}^{nuc} \frac{Z_A Z_B}{R_{AB}} + \sum_{i>j}^{elec} \frac{1}{r_{ij}} \quad \text{Eqn. 1.3.3}$$

$$\hat{H} = \hat{T}_N(R) + \hat{T}_e(r) + V_{eN}(r, R) + V_{NN}(R) + V_{ee}(r) \quad \text{Eqn. 1.3.4}$$

To approximate the electronic Hamiltonian, the Born-Oppenheimer approximation is applied to the equation. It assumes that atomic nuclei are very heavy compared to electrons, thus electrons are moving in the field of fixed nuclei and other electrons. This assumption allows for the Schrodinger equation to be separately solved for the electrons. Eqn. 1.3.5 is the resulting Hamiltonian after the Born-Oppenheimer approximation is applied.

$$\hat{H} = \hat{T}_e(r) + V_{eN}(r;R) + V_{NN}(R) + V_{ee}(r) \qquad \text{Eqn. 1.3.5}$$

Now, we have the electronic Schrodinger equation, shown in Eqn. 1.3.6., and expanded in Eqn. 1.3.7. Eqn. 1.3.7 will need to be solved to generate the calculable properties mentioned above.

$$\hat{H}_{el}(r;R)\Psi(r;R) = \hat{E}_{el}(R)\Psi(r;R) \qquad \text{Eqn. 1.3.6}$$

$$\hat{E}_{el}\Psi(r;R) = [\hat{T}_e(r) + \hat{V}_{eN}(r;R) + \hat{V}_{NN}(R) + \hat{V}_{ee}(r)]\Psi(r;R) \qquad \text{Eqn. 1.3.7}$$

The Hartree-Fock method is typically used to solve the electronic Schrodinger equation. This starts by invoking the Hartree product, Eqn. 1.3.8. If we assume that we are solving a system of 2 electrons, then the simplest approach would be to multiply the wavefunctions to describe the motion. However, since that is not the case for most systems, we can assume the product of the wavefunctions will describe the electron motion for larger systems. This is known as the Hartree product.

$$\Psi_{HP}(x_1, x_2, \ldots . x_N) = \chi_1(x_1)\chi_2(x_2) \ldots . \chi_N(x_N) \qquad \text{Eqn. 1.3.8}$$

$$\Psi = \frac{1}{\sqrt{N!}} \begin{vmatrix} \chi_1(x_1) & \chi_2(x_1) & \ldots & \chi_N(x_1) \\ \ldots & \ldots & \ldots & \ldots \\ \chi_1(x_N) & \chi_2(x_N) & \ldots & \chi_N(x_N) \end{vmatrix} \qquad \text{Eqn. 1.3.9}$$

$$|\chi_i \chi_j \cdots \chi_k\rangle \qquad \text{Eqn. 1.3.10}$$

To approximate the Hartree-product, slater determinants are used so that the antisymmetry principle is satisfied and the molecular orbitals can be assumed as a linear combination of atomic orbitals.

Now that we have established a pathway to model the orbitals, the Hamiltonian is re-evaluated. One electron and two electron operators are introduced to further simplify the electronic Hamiltonian.

Eqn. 1.3.11 and Eqn. 1.3.12 are the one electron and two electron operators, respectively.

$$h(i) = -\frac{1}{2}\nabla_i^2 - \sum_A \frac{Z_A}{r_{iA}} \qquad \text{Eqn. 1.3.11}$$

$$v(i,j) = \frac{1}{r_{ij}} \qquad \text{Eqn. 1.3.12}$$

The operators are applied to the electronic Hamiltonian equation and the result is shown in Eqn. 1.3.13.

$$\widehat{H}_{el} = \sum_i h(i) + \sum_{i<j} v(i,j) + V_{NN} \qquad \text{Eqn. 1.3.13}$$

Now the electronic energy can be written as

$$E_{el} = \langle \Psi | \widehat{H}_{el} | \Psi \rangle \qquad \text{Eqn. 1.3.14}$$

Where the wave function is normalized. The electronic energy, or Hartree-Fock energy, can be written by substituting the simplified Hamiltonian into eqn. 1.3.15

$$E_{HF} = \sum_i \langle i|h|i\rangle + \frac{1}{2}\sum_{ij}[ii|jj] - [ij|ji] \qquad \text{Eqn. 1.3.15}$$

Next, the Hartree-Fock equations are solved for the orbitals, this is better known as the self-consistent field method, which iterates through the HF equations until there is little variation in the resulting orbitals. Eqn. 1.3.16 is the expanded Hartree-Fock equation.

$$h(x_1)\chi_i(x_1) + \sum_{j\neq i}[\int dx_2 \left|\chi_j(x_2)\right|^2 r_{12}^{-1}]\,\chi_i(x_1) - \sum_{j\neq i}[\int dx_2 \chi_j^*(x_2)\chi_i(x_2) r_{12}^{-1}]\,\chi_i(x_1) = \epsilon_i\chi_i(x_1) \qquad \text{Eqn. 1.3.16}$$

The above equation can be simplified in terms of operators that describe the coulombic interactions, Coulomb term Eqn. 1.3.17, and spin orbital exchange interactions, exchange term Eqn. 1.3.18.

$$J_i(x_1) = \int dx_2 \left|\chi_j(x_2)\right|^2 r_{12}^{-1} \qquad \text{Eqn. 1.3.17}$$

$$K_j(x_1)\chi_i(x_1) = [\int dx_2 \chi_j^*(x_2)\chi_i(x_2) r_{12}^{-1}]\,\chi_i(x_1) \qquad \text{Eqn. 1.3.18}$$

Inserting the operators into Eqn. 1.3.16 gives

$$\left[h(x_1) + \sum_{j\neq i} J_i(x_1) - \sum_{j\neq i} K_j(x_1)\right]\chi_i(x_1) = \epsilon_i\chi_i(x_1) \qquad \text{Eqn. 1.3.19}$$

Eqn. 1.3.19 is further simplified in equations 1.3.20 and 1.3.21

$$[Ji(x_1) - K_i(x_1)]\chi_i(x_1) = 0 \qquad \text{Eqn. 1.3.20}$$

$$f(x_1)\chi_i(x_1) = \epsilon_i\chi_i(x_1) \qquad \text{Eqn. 1.3.21}$$

To solve for orbitals, basis sets are introduced (discussed later). To incorporate the basis

$$\chi_i = \sum_{\mu=1}^{K} C_{\mu i}\widetilde{\chi_\mu} \qquad \text{Eqn. 1.3.22}$$

sets, the Hartree-Fock equation is transformed into a Roothaan equation, Eqn. 1.3.22.

Substituting Eqn. 1.3.22 into Eqn. 1.3.21 and expanding gives,

$$\sum_v C_{vi} \int dx_1\, \tilde{\chi}_\mu^*(x_1) f(x_1) \tilde{\chi}_v^*(x_1) = \epsilon_i \sum_v C_{vi} \int dx_1 \tilde{\chi}_\mu^*(x_1)\tilde{\chi}_v^*(x_1) \qquad \text{Eqn. 1.3.23}$$

This introduces the matrix equation, to simplify further the left and right integrals are notated as $S_{\mu v}$ and $F_{\mu v}$, giving

$$\sum_v F_{\mu v} C_{vi} = \epsilon_i \sum_v S_{\mu v} C_{vi} \qquad \text{Eqn. 1.3.24}$$

Finally, the fock matrix is created, FC=SCϵ.

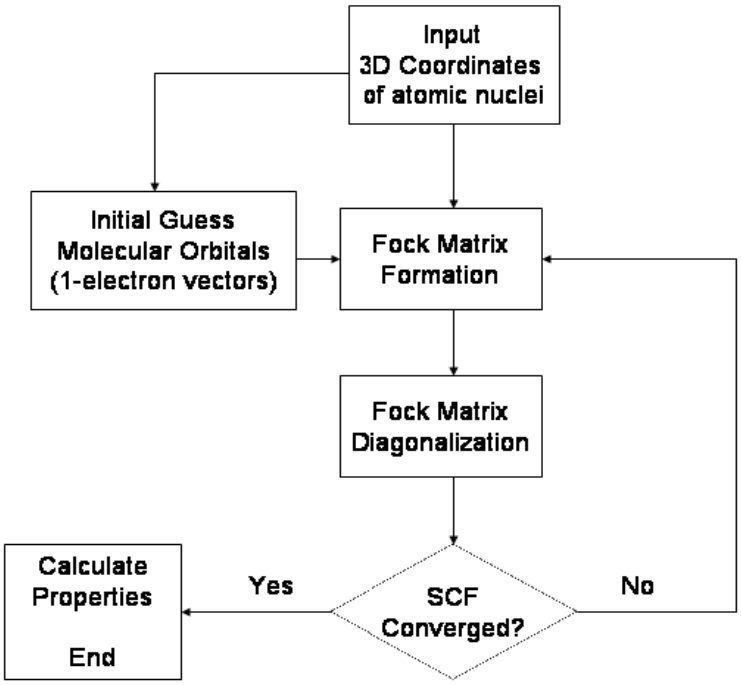

Figure 1.3.1: Flow chart of a Hartree-Fock calculation

Figure 1.3.1[66] demonstrates how a Hartree-Fock calculation is carried out. First the initial geometry is required for 3D coordinates. An initial guess of the molecular orbitals is made and input into the Fock Matrix. The Fock Matrix goes through diagnalization to solve for molecular orbitals. The self-consistency is evaluated for convergence and if it has not converged then the matrix is created again with another guess, but if it is converged then self-consistency has been achieved and properties can be calculated.

Basis Sets

$$BF = N \times e^{-\alpha r} \qquad \text{Eqn. 1.3.25}$$

The guess wavefunctions are often expanded over basis sets where functions are designed to represent the atomic orbitals. As an example, consider a methane molecule and a diiodosilane molecule. The diiodosilane molecule requires more "allowed" atomic orbitals than the methane because of their relative occupied electron orbitals. Implementing

basis sets customizes the calculation based on allowed atomic orbitals, polarization functions and diffuse functions. Slater type orbitals (STOs) are expressed as a linear combination gaussian orbitals to make them easier to integrate, where the form is eqn. 1.3.25.

And the STO is

$$\varphi_1(\alpha, n, l, m; r, \theta, \varphi) = N\, r^{n-1} e^{\alpha r} Y_{l,m}(\theta, \varphi) \qquad \text{Eqn. 1.3.26}$$

The STO is in spherical coordinates (r,θ,ϕ) where n, l and m are quantum numbers, and Y_{lm} is the angular momentum. STO basis sets are considered minimal basis sets, denoted as STO-nG. For example, a STO-3G* basis set includes 3 gaussian functions to make approximations for the slater type orbitals and one polarizable function. If more functions are included in the calculation to approximate orbitals, then the calculation will be more accurate and/or precise. Over the years other types of basis functions have been developed to improve the way orbitals are mathematically modeled. Table 1.3.1 lists common types of basis sets including minimal, Pople, correlation-consistent, and D,T,Q, zeta sets.

Table 1.3.1: Common bases sets utilized in *ab-initio* and DFT calculations

Minimal	Pople	Correlation Consistent	D,T,Q zeta
STO-nG (n=1,2…6) STO-3G*	3-21g, 3-21g*, 3-21+g, 6-31g, 6-31g*, 6-311g*	cc-pVDZ, cc-pVTZ, cc-pV5Z, aug-cc-pVDZ	SVP, DZV, TZV, TZVPP

Density Functional Theory

While the Hartree-Fock method and other traditional *ab-initio* methods created new fast and efficient ways to carry out quantum calculations, these methods are still approximations and make assumptions that can lead to inaccurate results in some cases. Some cons of the Hartree-Fock approach include high variability in results with relation to

basis functions and treatment of electron exchange correlation which assumes each electron interacts with an average charge density. All these aspects can be systematically improved upon and there are many highly accurate computational approaches to do just that but there is a heavy computational cost to be paid in scaling. Some highly accurate traditional ab initio methods scale as high as 2^7 with the number of basis functions which severely limits the system size which can be treated at those levels. To overcome these limitations, density functional methods were introduced to reduce the scaling without too much loss of accuracy.

A functional is a function of a function, here the density functional is shown as

$$p(r) = N \int \dots \int |\Psi(x_1, x_2, \dots, \dots, x_N|^2 \, ds_1 dx_2 \dots, \dots, dx_N \qquad \text{Eqn. 1.3.27}$$

Where p(r) is the electron density. The energy can be expressed as

$$E[p] = T_e[\rho] + U_{ee}[\rho] + V_{ext}[\rho] \qquad \text{Eqn. 1.3.28}$$

The energy is at a minimum if the density corresponds to the exact density of a ground state. To explicitly solve for the energy of the ground state, Kohn and Sham introduced a combined wavefunction and density equation.

$$E[\rho] = T_0[\rho] + \int [\hat{V}_{ext}(r) + \hat{U}_{el}(r)] \, \rho(r) dr + E_{xc}[\rho] \qquad \text{Eqn. 1.3.29}$$

The Kohn-Sham Hamiltonian is expressed as

$$\hat{H}_s = \sum_{i=1}^{N} -\frac{1}{2}\nabla^2 + v_s(r_i) \qquad \text{Eqn. 1.3.30}$$

Where $v_s(r)$ is the Kohn-Sham potential. The resulting Kohn-Sham one-electron equation is

$$\hat{h}_s \Psi_i = \left[-\frac{1}{2}\nabla^2 + v_s(r) \right] \Psi_i = \epsilon_i \Psi_i \qquad \text{Eqn. 1.3.31}$$

The final ground-state density is

$$n(r) = \sum_{i=1}^{N} |\Psi_i|^2 \qquad \text{Eqn. 1.3.32}$$

Solving equations 1.3.29-1.3.31 with a set of atomic coordinates and basis set will give a predicted energy. Once those steps are repeated until self-consistency is achieved, then other properties can be calculated.

The major advantage of this approach is that significantly larger systems can be treated (a few hundred atoms are routine due to the N^3 scaling) while still taking into account electron exchange and correlation. A number of density functionals have been developed, treating the exchange and correlation parts by using different functional forms. The disadvantage of using the density functional approximation is that the accuracy of the calculations can be highly dependent on the choice of the functional so benchmarking against high level traditional ab initio results for related systems and properties is recommended.

Semi-Empirical Methods

Semi-Empirical calculations simplify the Hartree-Fock method by utilizing some empirical parameters. These methods often eliminate core electrons from the calculation, use minimum basis sets, and reduce the number of integrals calculated. Parameter development is based on fitting to experimental measurements or high-level quantum calculations.

The Hamiltonian is written as

$$\widehat{H}_{val} = \sum_{i=1}^{n(val)} \left[-\frac{1}{2}\nabla_i^2 + V(i)\right] + \sum_{i=1}^{n(val)} \sum_{j>1} \frac{1}{r_{ij}} \qquad \text{Eqn. 1.3.33}$$

Where n(val) is the number of valence electrons and V(i) is the potential energy of a valence electron. The orbital equation, only considering valence electrons is

$$\varphi_i = \sum_{r=1}^{b} C_{ri} f_r \qquad \text{Eqn. 1.3.34}$$

And the electronic energy is

$$E = 2 \sum_{i=1}^{n(val)/2} H_{val,ii}^{core} + \sum_{i=1}^{n(val)/2} \sum_{j=1}^{n(val)/2} \left(2J_{ij} - K_{ij}\right) + V_{cc} \qquad \text{Eqn. 1.3.35}$$

From the last term, we can see the similarities with the Fock Matrix. While semi-empirical methods simplify the Hatree-Fock method, it can still be quite accurate and even employed in larger molecule systems, up to a thousand atoms.

Molecular Mechanics

Using Hartree-Fock, DFT, or semi-empitical methods for systems with tens of thousands of atoms is still not computationally feasible. Moreover, that level of calculation is not required for some results to be reasonably accurate or precise. For large molecular systems, typically methods such as Monte Carlo simulations or molecular dynamics simulations are carried out. This dissertation prospectus will focus on the theory of molecular dynamics (MD) simulations. MD simulations are based on the calculation of

energies from atomistic positions, forcefields, and velocities. Naturally, Newton's equations of motion are implemented to compute forces and velocities.

Forcefield parameters are created to iterate through Newton's equations of motion.

$$F_i = m_i a_i \qquad \text{Eqn. 1.3.36}$$

Forcefields consist of parameters that describe molecular intramolecular and intermolecular forces, often derived from *ab-initio* or DFT methods. In a particular implementation using an all-atom force field, Eqn. 1.3.37 is the total energy of the system consisting of energy contributions from molecular bonds between 2 atoms, angles between 3 atoms, torsion between 4 atoms, and interactions between non-bonded atoms. Intramolecular energies, E_{bond}, E_{angle}, $E_{torsion}$ are modeled as harmonic oscillators and all stem from Hooke's Law. Non-bonded interactions, or intermolecular interactions, are modeled using Lennard-Jones potentials and coulombic interactions. Equation 1.3.42 shows the Lennard-Jones potential energy equation.

$$E = E_{bond} + E_{angle} + E_{torsion} + E_{nonbond} \qquad \text{Eqn. 1.3.37}$$

$$E_{bond} = \sum_j \frac{1}{2} k\left(r_{ij} - r_0\right)^2 \qquad \text{Eqn. 1.3.38}$$

$$E_{angle} = \sum_\theta H_\theta (\theta - \theta_0)^2 \qquad \text{Eqn. 1.3.39}$$

$$E_{torsion} = V_1(1 + \cos(\emptyset)) + V_2(1 + \cos(2\emptyset)) + V_3(1 + \cos(3\emptyset)) \qquad \text{Eqn. 1.3.40}$$

$$E_{nonbond} = E_{vdW} + E_{Coulomb} + E_{hbond} \qquad \text{Eqn. 1.3.41}$$

To carry out a molecular dynamics simulation, first molecular coordinates, forcefield parameters, and initial velocities are required. Initial velocities are generated based on the Maxwell-Boltzmann distribution at the given temperature. Next, Newton's equation of motion is solved and iterated for a desired number of steps, then final energies, velocities, and trajectories are calculated.

$$V(r)^{LJ} = 4 \in \left[\left(\frac{\sigma}{r}\right)^{12} - \left(\frac{\sigma}{r}\right)^{6}\right] \qquad \text{Eqn. 1.3.42}$$

CHAPTER

2. BACKGROUND AND MOTIVATION

2.1 Background

2.1.1 Ionic Liquids and Electrolyte Mixtures

Recently, ionic liquids (ILs) have been employed in devices such as dye-sensitized solar cells, lithium-ion batteries, fuel cells, and sensor cells.[67–76] Their attractive properties including low volatility, low vapor pressure, high conductivity, and tunability through cation-anion selections make them prime candidates for such applications. To fully understand the complex interactions between the cation-anion pairs systematic research, including experimental and computational techniques, have been carried out.

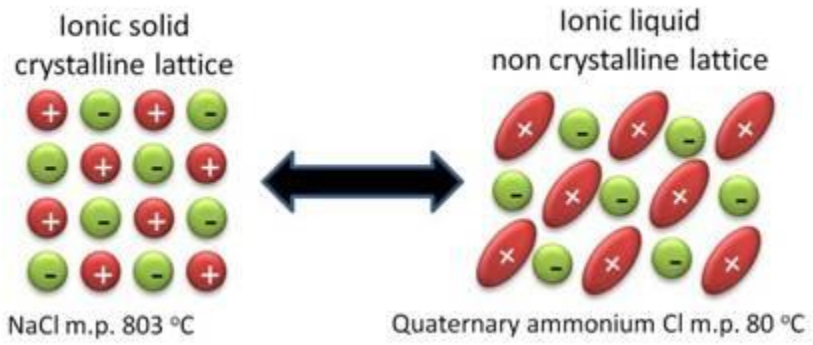

Figure 2.1.1.2: Demonstration of the difference between an ionic solid and ionic liquid with respect to anion-cation symmetry.

Ionic liquids are salts that consist of cation and anion pairs, have unique molecular coordination from their charge distributions, and as a result have melting points below 100°C. Figure 2.1.1.2 demonstrates the difference between ionic solids and ionic liquids[77]. On the left is a schematic of cation and anion pairs that form a solid lattice where NaCl is used as an example. The right is an ionic liquid with a non-crystalline lattice due to the difference in symmetry and charge between the ions. The size of the ions and functional groups incorporated into the molecular structure of the individual cations and anions inherently change the properties of ILs.

Classes of ILs have been established such that the types of ILs can be distinguished. Figure 2.1.1.3 contains common classes of ionic liquid cations and anions. These common cations have a variety of structures including rings and alkyl chains. For example, imidazolium-based ionic liquids contain an imidazolium ring structure with varying alkyl chain lengths in the cation, as shown in figure 2.1.1.3, which contributes to the change in inherent properties in imidazolium-based ionic liquids.

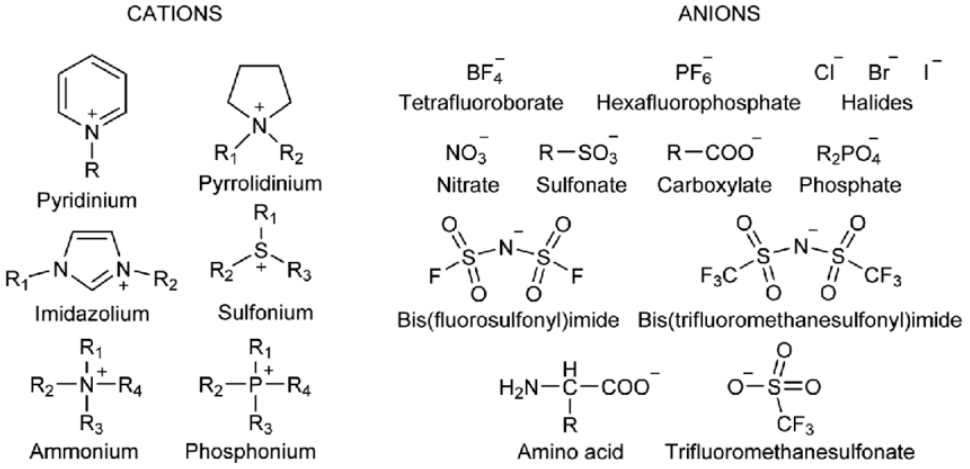

Figure 2.1.1.3: Classes of ionic liquids based on functional groups within cations and common anions.

Imidazolium-based ILs show promise in many applications due to the functionality of the imidazolium ring and cation-anion interactions. Experimental studies of imidazolium-based ionic liquids have characterized trends in physical properties such as transport and thermodynamic properties.[78,79,88–92,80–87] Results from these studies have demonstrated not only the complexity of these ionic liquids, but how variables such as alkyl chain lengths on the imidazolium cation and anion selection play huge roles in the properties. For example, in some imidazolium-based ionic liquids the density will increase with increasing alkyl chain lengths.[82,93–95] Moreover, the viscosity profiles also change when alkyl chain lengths are increased or decreased.

To fundamentally understand the molecular interactions of imidazolium-based ionic liquids, molecular dynamics simulations have been employed to explore the characteristics of such systems on an atomistic level. Molecular dynamics (MD) simulations utilize force fields with parameters often derived from density functional theory calculations applied to Newton's equations of motion to simulate systems of molecules containing tens of thousands of atoms.

While there are an assortment of force fields to choose from, increasingly accurate custom force fields have been published by a number of research groups including those conducted by Drs. Orlando Acevedo[96–99], Sundaram Balasubramanian[100], Jose Lopes[101,102], Agilio Padua[101], and Jorge Kohanoff[103] who have used first principles-based calculations to parameterize force fields specifically for ionic liquids. The customization of ionic liquid forcefields is necessary due to the unique cation-anion molecular interactions. One force field may be sufficient for a certain type of ionic liquid but not for another especially when considering the unique cation-anion pairs that can be created.

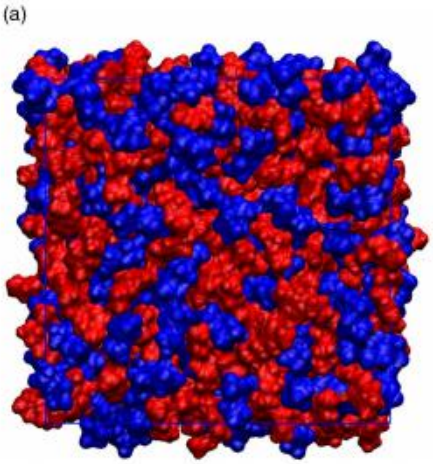

Figure 2.1.1.4: Example of a MD simulation box containing 1-butyl-3-methylimidazolium bis(trifluoromethanesulfonyl)imide

After the force field has been chosen, the simulation setup can continue through gathering necessary starting materials. To run an MD simulation, a coordinate file containing atom coordinates, topology file with force field parameters for inter and intramolecular forces and partial atomic charges, and a run file containing environmental parameters for the simulation are required. To contain the atoms and molecules, molecular structures are constrained to a box defined as an infinite system through periodic boundary conditions. This provides a small "snapshot" of the systems but allows for the results to be interpreted as a continuous system and makes structure-property relationships realistic. Figure 2.1.1.4[104] demonstrates a MD simulation box containing 1-butyl-3-methylimidazolium (red) and bis(trifluoromethanesulfonyl)imide (blue) and exemplifies how ionic liquid systems are studied through MD simulations. The box edges are meant to contain the molecules; however, the box dimensions can change based on the simulation ensemble chosen.

Environmental variables are set through ensembles which describe the conditions of the simulation and are used based on the desired outputs. Common ensembles are isothermal-isobaric (NPT), where the number of particles (N), pressure (P), and temperature (T) are held constant, and canonical (NVT) which is similar to the NPT ensemble except the volume is held constant instead of pressure. Typically, NPT ensembles are used to mimic experimental results and NVT ensembles are used to equilibrate the simulation boxes, but there are other ways to use the ensembles that are not explored in this prospectus. To monitor the temperature and pressure of the simulation boxes, specific thermostats and barostats are chosen. Furthermore, the simulations are also carried out at varying time lengths to capture the desired molecular interactions and motions. An

equilibration with an NVT ensemble may only require 1 ns, but an NPT simulation that will be used to explore the characteristics of the simulation may require more time.

The results of MD simulations can vary widely and are chosen based on the purpose of a study. Typically, density measurements are used to validate the simulations. Densities are directly correlated to intermolecular spacing and molecular charges that are used as simulation parameters. Once validation on the simulations has been done, the results can be used and analyzed. For example, MD simulations of ILs provide insight into transport properties through self-diffusion coefficients[80,94,105], and subsequently viscosity and conductivity. Molecular interactions between cations and anions are often characterized through radial distribution functions[80,106], or probability functions that describe the likelihood of bonding and coulombic interactions. Thermodynamic properties such as heat capacities and heats of vaporization can also be calculated through reported energies from the simulations.[78,107] Clearly, MD simulations are a powerful tool and have enhanced our understanding of ionic liquids through serving as a predictor tool of their properties and providing explanations of phenomena observed in experiments.

Recently, our group has used MD simulations as a pathway to further understand ionic liquid electrolyte mixtures. Ionic liquids are often mixed with solvents such as water or other organic solutions to create electrolyte mixtures. Electrolyte mixtures tend to lower viscosity and increase conductivity when compared to neat ILs. The concentration of each component in the electrolyte can heavily affect the properties of the mixture, hence MD simulation studies have been expanded from pure ionic liquid focuses to include electrolyte mixtures in order to accomplish a better understanding of such mixtures. Past group members have reported characteristics of ionic liquid mixtures and electrolyte mixtures

from MD simulations.[108,109] One study of particular interest explores the effects of water on 1-butyl-3-methylimidazolium iodide [BMIM][I].

[BMIM][I] is not a commonly studied ionic liquid, but it is a prime candidate for devices that utilize tri-iodide reactions for operations, and it is miscible in solvents such as water. Nickerson et. al. systematically studied [BMIM][I]/water mixtures using MD

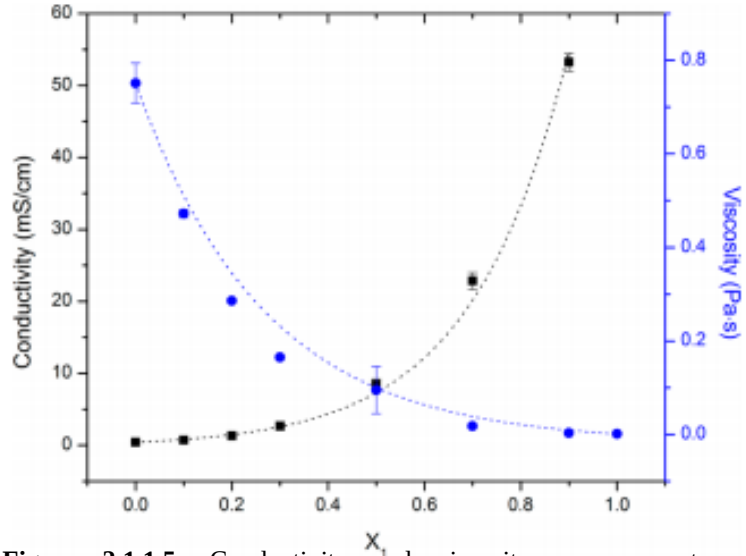

Figure 2.1.1.5: Conductivity and viscosity measurements of [BMIM][I]/water mixtures

simulations and showed how the concentration of water changes transport properties such as conductivity and viscosity, and explored the underlying molecular interactions between the ionic liquid and water.[108] Figure 2.1.1.5[108] is a plot of conductivity (black) and viscosity (blue) of [BMIM][I]/water mixtures as a function of the concentration of water. As the mole percent of water is increased, the viscosity decreases and the conductivity increases. Notably, the viscosity and conductivity change dramatically when water concentration is greater than 50%. The simulation results consisting of simulation box snapshots, radial distribution functions, and self-diffusion coefficients, revealed a change in ionic liquid ordering at high concentrations of water where eventually, a water network dominates the

mixture with pockets of ionic liquid dissolved within. These results have been a starting point for new developments of ionic liquid mixtures and continue to contribute to our current research to design more complex electrolyte mixtures.

2.1.2 Atomic Layer Deposition in Semiconductors

Atomic Layer deposition (ALD) is a method that utilizes surface reactions of gas phase reagents to build thin film surfaces or layers.[110–115] ALD is a branch of chemical vapor deposition (CVD) but is designed for conformality and control of layer thickness. Common applications of ALD, outlined in Figure 2.1.2.1[116], include generating thin films for nanostructures, nanotubes, nanowires, protective shells, coatings for polymer membranes, as well as thin films for transistors and memory in semiconductors.

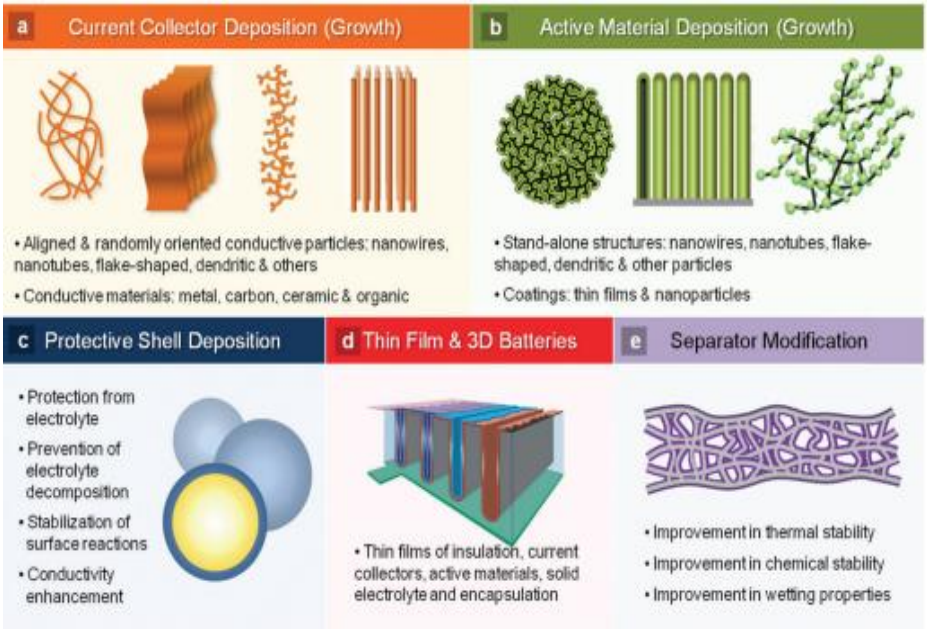

Figure 2.1.2.1: Application of atomic layer deposition (ALD)

Chemical vapor deposition is an umbrella term for processes that grow material on various surfaces through chemical reactions. CVD processes, such as APCVD, LPCVD, PECVD, PCVD, and ALD are chosen for a specific application.[117–121] For example, atmospheric pressure chemical vapor deposition (APCVD) is mostly used in large scale

applications such as glass coatings to create a uniform field, while plasma enhanced chemical vapor deposition (PECVD) is commonly used in the fabrication of electronic devices.[122,123] In the context of semiconductor fabrication, ALD is commonly employed to create thin and uniform films in a controlled manner. This is achieved through introducing precursors to reactive surfaces sequentially and repeating with different reactants, or the same, a predetermined number of cycles. By encouraging the slow growth of films, ALD films easily conform to surfaces, are smooth, and often are carried out at relatively low temperatures (200°C - 400°C).[112,116,124–126]

Figure 2.1.2.2[127] shows an example reaction mechanism of an ALD process. In the first sub-cycle, the gaseous precursor is exposed to the substrate. Once enough time is given for the reaction to reach almost full monolayer coverage, the remaining precursor is

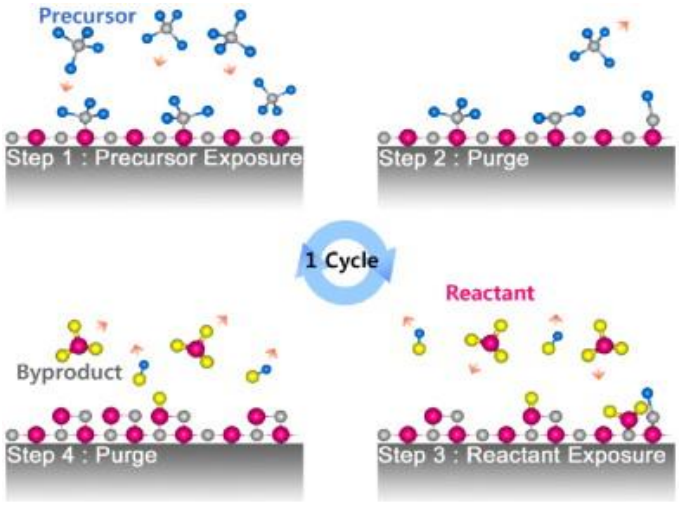

Figure 2.1.2.2: Reaction mechanism for an ALD process

removed from the system often by using a purge gas, such as N_2. In the next sub-cycle, another precursor or reactant is introduced and then purged. By the last step, the film has grown in thickness and the initial surface is re-established, ready for the next cycle. The sub cycles of ALD are self-limiting, meaning that once the precursors have reacted with

the active sites on the surface the half-reaction is complete. The self-limiting nature of ALD is the reason why uniform monolayers on a variety of surface topographies are achievable through this process.

ALD can be difficult to achieve when testing surface-precursor combinations and reactions. The ALD process only occurs within a defined temperature window where the growth per cycle becomes independent of temperature and therefore reaches a plateau. Figure 2.1.2.3[128] demonstrates how an ideal ALD temperature window is determined. The

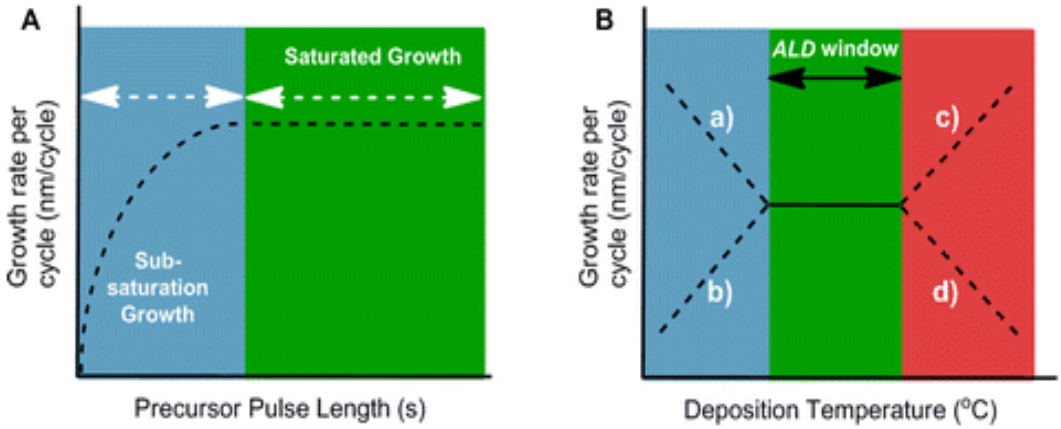

Figure 2.1.2.3: Plots determining the ALD window of a reaction. (A) demonstrates the precursor pulse length needed to achieve saturated growth. (B) shows the temperature window based on the growth per cycle and deposition temperature

plot on the left shoes how the growth per cycle (GPC) is affected by the precursor gas pulses. Once the growth reaches a plateau, the ALD temperature window is determined. At temperatures lower than the window, the GPC increases and precursor condensation can occur, while above the window the precursors could decompose or desorb from the surface.[106] The ALD temperature window is different for every reaction and is heavily dependent not only on the chosen surface, but selected precursor.

Precursors need to meet certain criteria in order to be effective, this includes high reactivity and thermal stability.[129–133] To endure ALD environments and ensure the

precursors will not decompose, they need to have a suitable thermal stability. Reactivity of the precursor is key, as this will be crucial in carrying out the reactions and forming a film. There are many pathways and methods for precursor screening, however, a common and effective method is the utilization of *ab-initio* and DFT calculations.

Computational chemistry techniques aid in precursor screening through providing reaction mechanisms, relative energies to calculate reaction and activation energies, and thermodynamic properties to determine thermal stability. Often these calculations are carried out using *ab-initio* or DFT based software on systems containing > 100 atoms.

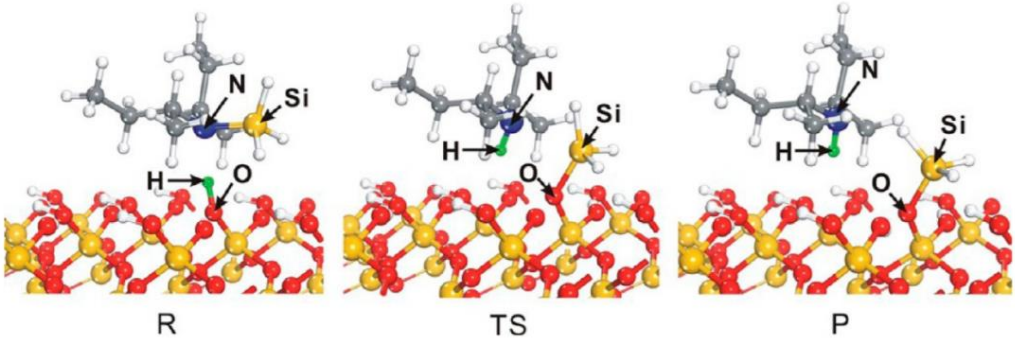

Figure 2.1.2.4: DFT results depicting the reactants, transition state complex, and products between an SiO_2 surface slab model and di(sec-butyl)silane

Common approaches to simulate the precursor-surface reactions include the use of small cluster or slab models that represent an extremely small portion of the reactive surface. Figure 2.1.2.4 is an example of how an SiO_2 surface slab model has been used to determine the transition state (middle), which lies between the reactants and products (left and right respectively), between the surface and di(sec-butylamino)silane. In this particular mechanism, the nitrogen (blue) hydrogen bonds to the surface hydrogen (green) and the silane bonds to the surface oxygen. The transition state tends to create an activation energy barrier and effects the efficiency of the reaction. Reactions with high activation energy barriers may require alternate methods to intervene and carryout the reaction. Small scale

calculations, such as those demonstrated in figure 2.1.2.4, can be used to calculate reaction energy barriers between precursors and ALD surfaces to determine precursor reactivity and the likelihood that the reaction will occur under ALD conditions. While transition states can be roadblocks in precursor screening and development, there are other energy barriers to consider in reaction pathways. For example, a crucial step in ALD is the adsorption between the transition state and product. If the energy required for desorption is high, then this creates another energy barrier to overcome for successful ALD.

Precursor selection depends on the resulting film characteristics, resources available to carry out the process, and ALD environment. In the context of SiO_2 film growth, a necessity in the semiconductor industry, aminosilane-based precursors have grown in popularity for such purposes.[134–137] Aminosilane precursors tend to contain a silane with varying amine groups and alkyl chain ligands. By changing the number of amines and alkyl chains, this group of precursors can be fine-tuned to fit applications and ALD environments.

2.2 Motivation

2.2.1 Utilization of Molecular Dynamics to Optimize Electrolyte Mixtures Employed in Applications for Extreme Environments

When it comes to designing electrolyte solutions for devices, there are multiple properties to consider including density, viscosity, conductivity, and a temperature window of operation. All of these characteristics can be attained by formulating and fine tuning an electrolyte mixture. There are countless ways to approach the design of such solutions, however, MD simulations are a common tool, especially when studying complex electrolyte solutions.

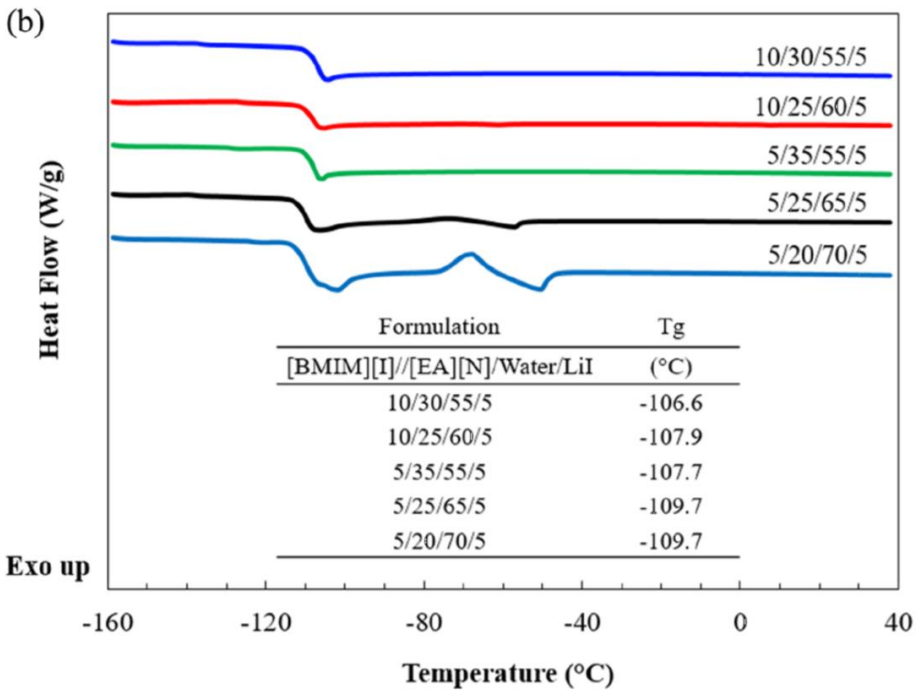

Formulation [BMIM][I]//[EA][N]/Water/LiI	Tg (°C)
10/30/55/5	-106.6
10/25/60/5	-107.9
5/35/55/5	-107.7
5/25/65/5	-109.7
5/20/70/5	-109.7

Figure 2.2.1.1: Differential scanning calorimetry (DSC) curves and reported glass transition temperatures (Tg) for ionic liquid electrolyte mixtures contatining [BMIM][I]/[EA][N]/Water/LiI

Recently, our group members have reported multiple formulations of a rare 4 component electrolyte solution that has potential to be used in energy storage devices, and more specifically, sensor devices that utilize a tri-iodide reaction for operation. The system, comprising of 1-butyl 3-methylimidazolium iodide, ethylammonium nitrate, water, and lithium iodide, displayed traits of good conductivity and an impressive temperature window of operation.

Figure 2.2.1.1 are differential scanning calorimetry (DSC) results of [BMIM][I]/[EA][NO_3]/Water/LiI mixtures. DSC results show changes in the thermal behavior of the IL mixtures including phase changes and glass transition temperatures, or Tg. Glass transition temperatures are the point where the material undergoes a transition from a glassy state to a rubbery state and is common in amorphous structures and ionic liquids.[138–141] The Tg is also an indicator of the low temperature bound of the temperature

window. Here, the glass transition temperatures of the IL mixtures show the development of eutectic mixtures capable of retaining liquid properties at extremely low temperature, down to -109.7 °C.

While we hypothesized the reasons for the low temperature behavior, including the introduction of new molecular interactions, more studies needed to be carried out to gain a complete understanding. In order to continue the work, we studied a ternary system of 1-butyl-3-methylimidazolium iodide, ethylammonium nitrate, and water using MD simulations. Furthermore, we hypothesize that the addition of water to the ionic liquid mixture will eventually cause water to dominate the systems where a water network is created. MD simulations of imidazolium-based ILs and water show a disruption in the ionic liquid ordering at high water concentrations often caused by water hydrogen bonding with itself and the anion of the ILs.[142–144] Even in an mixture with two ionic liquid cosolvents, we expected to see similar trends in the results.

The implementation of MD in this study allows us to understand molecular interactions between the ILs, ILs and water, and compare them to neat ILs as well as transport properties from a molecular level. This knowledge and understanding can further the development of other ionic liquid electrolyte solutions and improve upon those that have already been created. In this dissertation prospectus we present the MD simulation results of five electrolyte mixtures containing [BMIM][I]/water/[EA][NO_3] as a complimentary study to the experimental results already reported. In order to focus on the effects of water on the ionic liquid mixture, the concentration of water was slowly increased starting from a 50/50 IL mixture until 80 mol% water was reached. Included in the results are densities, simulation box snapshots, radial distribution functions, and self-diffusion

coefficients. Results indicate a significant change in properties and molecular interactions with high concentrations of water. Moreover, these results give insights into how these molecular interactions effect the bulk properties observed in experiments.

While on the topic of glass transition temperatures, we also explored the possibility of using MD simulations as a predictor for Tgs. The utilization of molecular dynamics to predict the glass transition temperature of imidazolium-based ionic liquids has been reported[145,146], however, the methodology has not been applied to [BMIM][I]. Moreover, the studies do not use an OPLS-AA forcefield. Forero-Martinez et.al reported the glass transition temperature of [BMIM][PF_6] from an MD simulation using an empirical force field and the DL_POLY program.[146] Figure 2.2.1.2 demonstrates their methodology in predicting the Tg where the average potential energy per ion pair is plotted vs temperature.

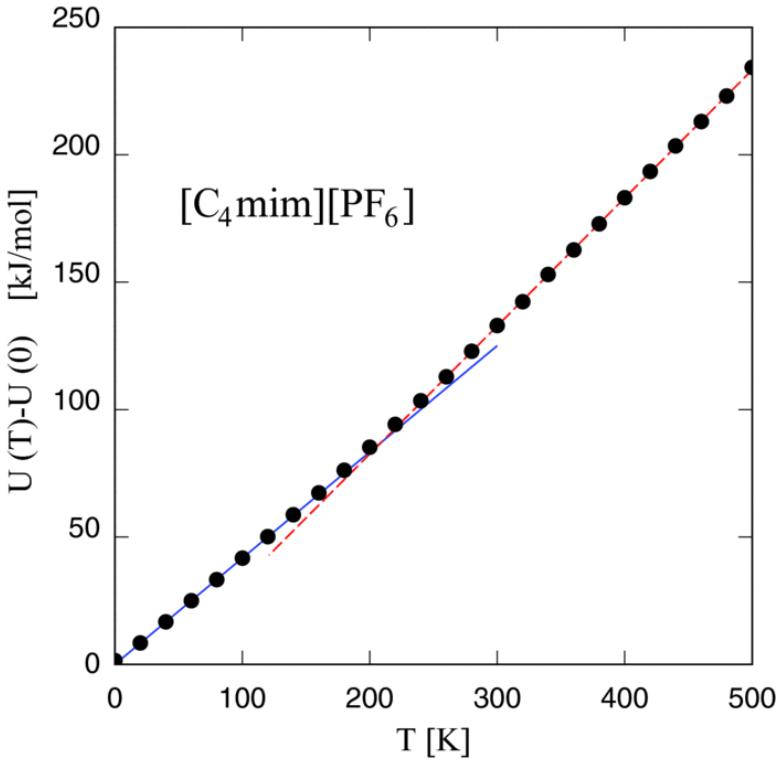

Figure 2.2.1.2: Glass transition temperature prediction of [BMIM][PF_6]. The average potential energy of ion pairs vs temperature plot shows two linear regions fitted with the blue and red lines. Where they intersect is the predicted Tg.

There is a difference in the slopes of the high temperature and low temperature regions, therefore, they estimate the Tg to be the point where the linear fittings intersect to be the Tg.

To further improve our efforts to predict glass transition temperatures of ionic liquids, we also report a refined method to use MD simulations to predict the Tgs of neat ionic liquid [BMIM][I]. In the reports mentioned above parameters such as simulation annealing rate and box lengths have not been comprehensively tested. We report a method to predict Tgs of imidazolium-based ionic liquid [BMIM][I] through molecular dynamics simulations by monitoring the slope of the ΔE_{pot}/ion pair vs temperature plot and identifying a discontinuity. Two annealing rates and simulation box lengths were tested to conclude if such parameters effect the glass transition temperature.

2.2.2 Combined DFT and Semi-Empirical Computational Techniques to Simulate ALD Precursor Reactivity and Stability

ALD is commonly utilized in the fabrication of semiconductors. Figure 2.2.2.1 shows the layers of a transistor that, when combined with other transistors, ultimately make up a larger integrated circuit. Typically, layers of materials are deposited onto a silicon wafer that has an etched pattern to make up the circuits and fine tune the behavior of the

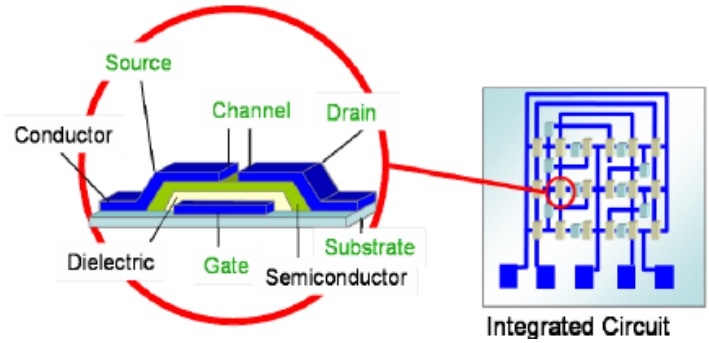

Figure 2.2.2.1 Schematic of transistor layers within an integrated circuit

circuit. In the figure, there is a dielectric layer (yellow) that is often deposited through ALD or another CVD process. At Versum Materials, we develop high-k and low-k dielectric precursors for such purposes.

A specific group of precursors developed at Versum Materials are aminosilane-based where amino group or groups are attached to the silane with varying alkyl chains. Such precursors show encouraging results for ALD applications for the growth of thin films such as SiO_2. SiO_2 films play a major role in the development of transistors and their conformations through deposition to create thin films can be difficult to achieve. Precursor screening for aminosilane candidates that have potential to create uniform SiO_2 films is commonly carried out with DFT calculations where the reaction mechanisms and ALD temperature windows are predicted. Figure 2.2.2.2 shows the predicted ALD temperature

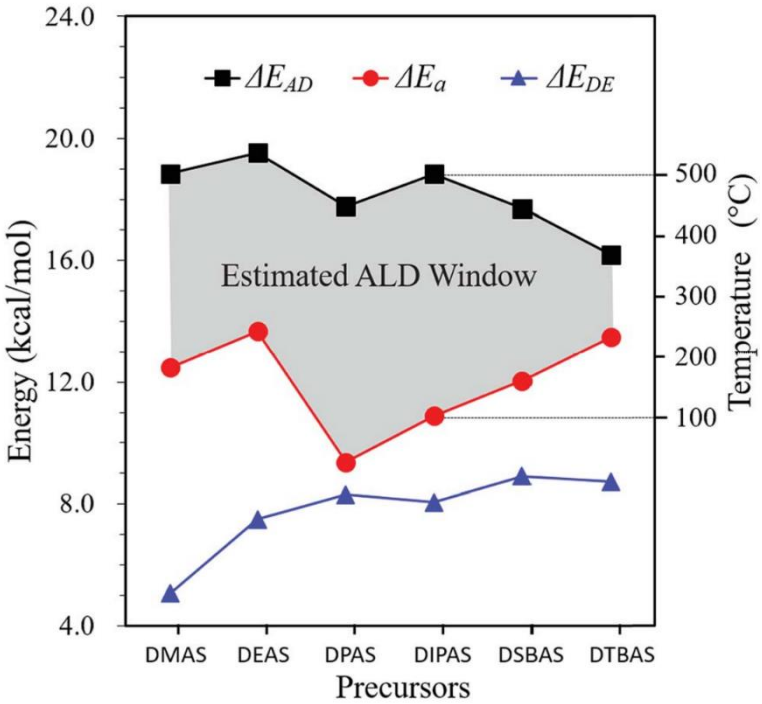

Figure 2.2.2.2: Estimated ALD temperature windows for mono-aminosilane precursors and a SiO_2 surface slab from DFT results

window of a group of mono-aminosilane precursors. Based on these results, all six of the precursors studied would be good ALD candidates.

To expand the comprehensive study of mono-aminosilane precursors by Huang et. al. we present a study of 10 aminosilane precursors to determine their viability for SiO_2 thin film growth through ALD. The precursors, consisting of mono and bis amino ligands, provide a comparison between the two types of aminosilane ligands. Similar to Huang et. al., DFT is used to complete the precursor screening, however, in this dissertation prospectus, we use a small cluster model consisting of a hydrogen terminated SiO_2 active site instead of a slab model. This cuts computation time and allows for more precursors to be included in the study while maintaining trends from slab models. A proposed reaction pathway as well as reaction coordinates are provided for a select group of precursors. The reaction energies and activation energies between the precursors and cluster model are also reported to explore trends between the amino group ligands.

Furthermore we also report the thermodynamic properties of the ten precursors, enthalpy of formation (ΔH_f) and gibbs free energy of formation (ΔG_f), which are used in scale up engineering and design. The intent of reporting the values is to compare two thermochemical recipes that are commonly employed in atomistic thermodynamic calculations. The first is a thermochemical recipe implemented in the Gaussian09 program named G3MP2 where four separate calculations are carried out to attain extreme accuracy. The next is a simpler calculation from the Spartan v'18 program named T1 where two calculations are carried out, however, initial comparisons report that the two recipes are comparable for some compounds.[147] The driving force for this comparison is the extreme difference in computation time and resources between the two methods. The G3MP2

method can take orders of magnitude longer than the T1 method to finish a calculation. The results from our calculations show good agreement between the two methods.

Currently, our capabilities include calculations for precursor reactions with small clusters and small area periodic surface slabs, however, expanding to a larger surface would allow for more property measurements such as growth per cycle and monitoring of active sites on the surfaces. In the literature, Atomic Layer Deposition has been simulated using reactive molecular dynamics, however, the forcefields associated with these chemistries are incredibly complex and require extensive parameterization for specific applications[148,149]. Thus, in this dissertation prospectus we propose utilizing methods such as semi-empirical tight binding approaches to simulate ALD reactive surfaces large enough to adsorb multiple reactant molecules and thus, simulate behavior at conditions approaching the full monolayer coverage.

CHAPTER

3. METHODS

3.1 Computational Methods

A Molecular Dynamics Insight on the Role of Water Molecules in Ionic Liquid Mixtures of 1-butyl-3-methylimidazolium Iodide and Ethylammonium Nitrate

The molecular dynamics simulations were carried out using the GROMACS 5.1.4 package.[150–152] For each formulation, the initial configurations were constructed by randomly inserting [BMIM][I], [EA][NO_3], and water into a 5x5x5 nm^3 box. [BMIM][I] and [EA][NO_3] were inserted pairwise. Table 3.1.1 shows the number of each ion pair and water molecule that constitutes the five simulation boxes.

Table 3.1.1 Formulations and respective box constituents of [EA][N]/Water/[BMIM][I] mixtures reported

Formulation (mol%) [EA][N]/Water]/[BMIM][I]	# of [EA][NO_3] Pairs	# Water Molecules	# of [BMIM][I] Pairs
10-80-10	80	640	80
20-60-20	160	480	160
30-40-30	240	320	240
40-20-40	320	160	320
50-0-50	300	0	300

The ionic liquids [BMIM][I] and [EA][NO_3] was described by an OPLS-AA force field. Parameters for the [BMIM] and $[EA]^+$ cations were implemented from works by Lopes[153] and Bhargava and Balasubramanian[100] while parameters for $[NO_3]^-$ was modeled using OPLS parameters from Doherty et.al[96] where they revisited forcefield parameters originally reported by Acevedo et al.[99]

The initial configuration boxes underwent a 1000 step energy minimization using the steepest descent method. An NVT equilibration was then performed for 0.5ns followed by a 20 ns NPT simulation. Each simulation used the leapfrog algorithm to integrate Newton's equations of motion with a time step of 0.002ps and hydrogen bonds were constrained with the LINCS algorithm[154,155]. Long range electrostatic interactions were treated using the particle-mesh Ewald (PME) while Lennard-Jones forces were treated with a cut off of 1.2 nm. The velocity-rescale thermostat[156] was used in the NVT equilibrations. For the NPT simulations, the berendsen thermostat[157] and parinello-rahman barostat[158] were used in the with a reference temperature and pressure of 295K and 1 bar. Simulation results including densities, radial distribution functions, and self-diffusion coefficients were computed with the GROMACS package between 5 and 10 ns. The Visual Molecular Dynamics package (VMD)[159] aided to visualize the simulation boxes and create simulation box snapshots from the last nanosecond of each simulation.

Glass Transition Temperature Predictions of Imidazolium-based Ionic Liquids

The forcefield utilized for the ionic liquids was first reported by Sambasivarao and Avcevedo in 2009[99], however, their group recently improved the forcefield, which showed improved predictions of thermodynamic properties. The latest forcefield by their group, published in 2017[96], was used for the glass transition temperature predictions.

The MD simulation details for the glass transition temperature predictions including energy minimizations, equilibration parameters, thermostats, and barostats, are the same as those above. The GROMACS package was used to carry out annealing simulations with varying cooling rates. The ionic liquid ion pairs were inserted randomly into boxes with length of 5nm and 6nm. To test variability in the simulation results,

multiple trials were carried out with the same starting configurations. Results from the trials concluded that three trials need to be done to predict the glass transition temperature in order to account for the stochastic nature of the simulations. Data for the self-diffusion coefficients and radial distribution functions was averaged over 20K segments in order to maintain accuracy in the MSD and RDF calculations.

Computational Studies of the Stability and Reactivity of Atomic Layer Deposition Precursors

The building and modifications of ALD precursors, clusters, and surfaces were done with the Materials Studio R2017 package visualizer.[160] Reaction mechanism complexes, transition state searches, and reaction energies were calculated with the DMol3[161–163] package using the BLYP[164–167] density functional and DNP basis set. Reaction energies were benchmarked using the MP2/6-31G*[168–171] *ab-initio* method in the Spartan V'18 package.[172] Thermodynamic properties including ΔH_f and ΔG_f were calculated using the Gaussian09[173] program G3MP2 thermochemical recipe and Spartan V'18 T1 thermochemical recipe. Semi-empirical tight binding calculations were carried out using the GFN2-XTB[174–179] package. The starting configurations were created in Materials Studio R2017.

3.2 Experimental Methods

The ionic liquids 1-butyl-3-methylimidazolium iodide ([BMIM][I]) and ethylammonium nitrate, ([EA][NO_3]) were purchased from Ionic Liquids Technologies Inc., and HPLC grade water was purchased from Fischer Scientific. Ionic liquid solutions were combined and mixed manually and by a Sonics VibraCell at 500W until the solution was visibly homogeneous.

Density measurements were done at room temperature using a 2mL specific gravity bottle that was calibrated using HPLC grade water.

CHAPTER

4. RESULTS AND DISCUSSION

4.1. A Molecular Dynamics Insight on the Role of Water Molecules in Ionic Liquid Mixtures of 1-butyl-3-methylimidazolium Iodide and Ethylammonium Nitrate

4.1.1 Validation of Forcefields for Ionic Liquids and Their Mixtures

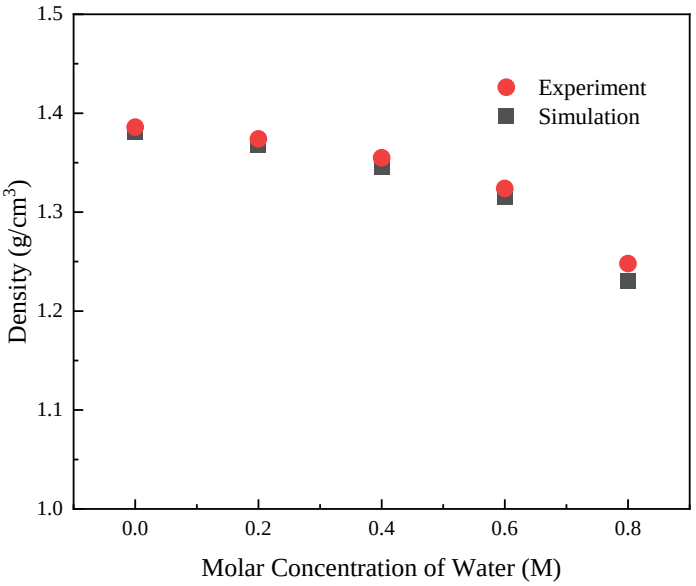

Figure 4.1.1.1: Plotted experimental and simulated densities for all formulations. Red dots indicate experimental values while the grey indicate simulation values.

The five formulations were selected to include varying molar percentage of water from 20 mol% up to 80 mol% with increments of 20 mol% to validate MD simulation accuracy over a wide concentration range. The concentrations of the ionic liquids were split equally between [BMIM][I] and [EA][NO_3], for example, for a formulation of 20 mol% water, there was 40 mol% [EA][NO_3] and 40 mol% [BMIM][I]. The number of molecules per simulation box were chosen to adequately fill the box. Density is often used to validate simulation results because forcefields represent intramolecular and intermolecular distances, as well as system volumes, that reflect experimental

densities.[101,180–183] Comparison between the experimental and simulated density values are plotted in Figure 1. The difference between the experimental and simulation values all fall under a three percent difference, which is a generally accepted threshold for density differences. As expected, the incorporation of water to the [BMIM][I]/[EA][NO_3] mixture decreases the density as water is much less dense than the ionic liquids. The good agreement validates the OPLS-AA forcefield and allows for an in depth look at the results from the simulations.

4.1.2 Qualitative Analysis of Simulation Boxes via Snapshots

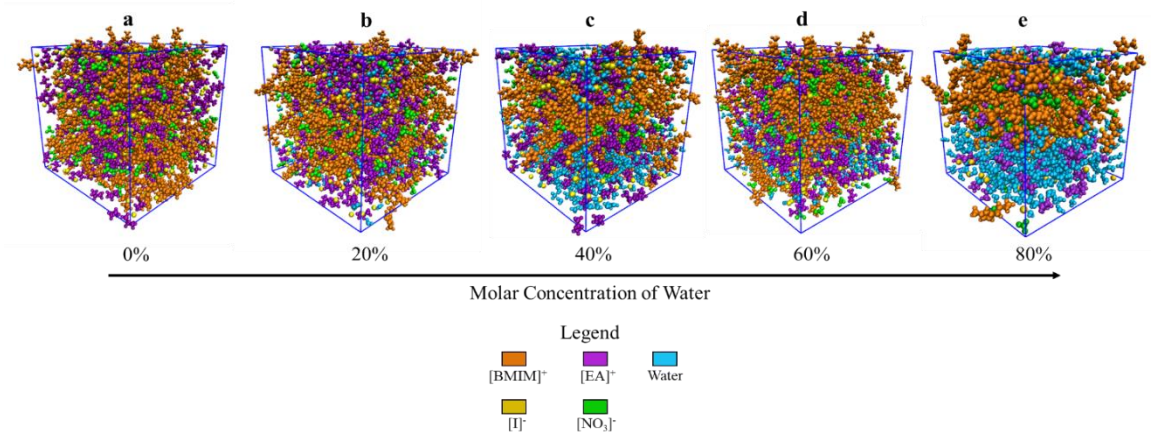

Figure 4.1.2.1: Visualizations of the simulation boxes at 20 ns for all formulations. Blue lines indicate the box edges, where periodic boundary conditions apply.

To visualize the molecular ordering of respective mixtures, snapshots of each simulation box at 20ns were created and displayed side by side in Figure 2 to monitor the qualitative changes between mixtures. Snapshots aid in showing how the mixtures change from their initial to final equilibrated configurations; however, for the purpose of this study, we use them to identify changes in the equilibrated molecular structures between formulations. Through interpreting the visualizations, we can make initial guesses at possible molecular interactions and gain understanding of structural changes.

The blue boxes within the snapshots are the simulation box edges and each ion or molecule has been colored according to the legend. Within box "a", which shows a 50/50 mixture of ionic liquids [BMIM][I] and [EA][NO_3], the ionic liquids are mixed homogeneously where no definite large pockets of ionic liquids are separated. The orange $[BMIM]^+$ cation and iodide anion are well dispersed with the ethylammonium cations and nitrate anions. With increasing molar percent of water, the ionic liquid structures no longer resemble homogeneous systems. A noticeable transition occurred when water concentration increased from 40-60 mol%, where pockets of water and ionic liquid are forming. At 80 mol% water, the orange $[BMIM]^+$ ions cluster with the green nitrates while the iodide anions cluster with water, and the purple ethylammonium cations are dispersed between both clusters. Eventually what seems to be a water network, or large aggregates, starts to form and is most prominent in simulation box "e" with 10 mol%[BMIM][I], 10 mol% [EA][NO_3], and 80 mol% water. Water aggregates and networks are known to occur at higher water concentrations in electrolytes and cause phase separations,[184–186] which also seems to be the case in the studied systems. At high water concentrations there is clearly a segregation between two groups, one comprising of water and iodide and the other $[BMIM]^+$ and $[NO_3]^-$. Ethylammonium seems to be interacting with both groups, but to get a clear picture of the molecular interactions, further investigation is done through radial distribution functions.

4.1.3 Exploration of Molecular Interactions Through Radial Distribution Functions

Radial distribution functions, which represent the probability, g(r), of a molecule or atom residing a distance (r) from another molecule or atom, were computed to characterize the molecular interactions within the mixtures. Radial distribution functions

between iodide-ethylammonium and iodide-water are plotted in Figure 4.1.3.1. Figure 4.1.3.1a represents a radial distribution function between iodide and the NH_3 group on the ethylammonium. In the 50-0-50 formulation (gold), there is a high probability that two ethylammonium molecules are ordering themselves around iodide. In mixtures with water, the two distinctive peaks and their relative positions indicate two $[EA]^+$ molecules surrounding iodide. As the molar percent of water decreases, the two peaks also start to decrease, suggesting that this particular interaction is highly dependent on the concentration of water in the mixture because the ionic liquid concentrations are equal.

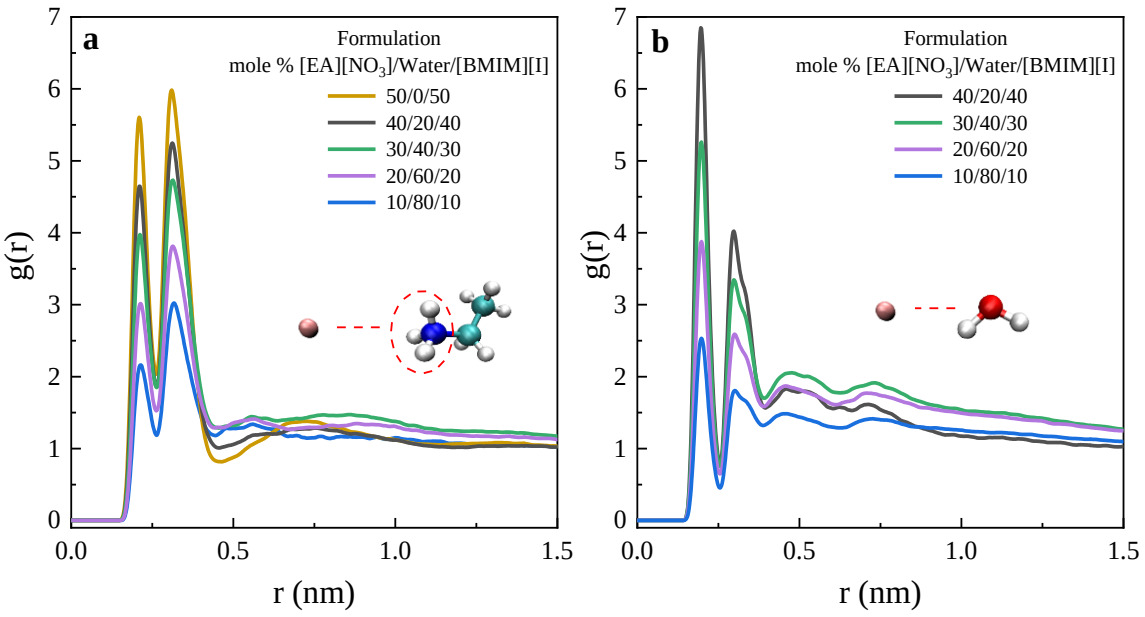

Figure 4.1.3.1: Radial distribution functions between iodide and $[NH_3]^+$ (a) and iodide and water (b)

Figure 4.1.3.1b are radial distribution functions between iodide and water. The probability functions have a similar trend to that of iodide and ethylammonium with two distinct peaks at similar distances, suggesting water is also ordering itself around iodide as two water molecules around one iodide via hydrogen bonding. Hydrogen bonding between water and iodide has been reported previously.[108,187] Chandra and Karmakar reported a first principles study of iodide and water where water is found to diffuse within the solvation

shell of iodide.[187] Furthermore, their results indicated water molecules hydrogen bonding with iodide within the first solvation shell and others remaining in the shell but not hydrogen bonding. Figure 3b is in agreement with the findings of Chandra and Karmakar[187] where water ordering has a similar trend.

Both interactions displayed in Figure 4.1.3.1 are dependent on the concentration and possibly the self-diffusion of water, indicated by the increasing probabilities with decreasing water concentration. The iodide-water RDFs decrease in magnitude with increasing water concentration is most likely due to water molecules interacting with each other at higher concentrations and less with iodide. The same trend found between iodide-$[EA]^+$ RDFs could be a result of the water aggregates forming that were identified in the simulation box snapshots. The change in the homogeneity of the system and transport properties decreases the probability of the iodide-$[EA]^+$ bonding, but the structure of the mechanism remains the same which is confirmed by the continued peak trends in the RDF. Furthermore, the iodide sites are likely competitive for both water and the $[EA]^+$ cations and would explain the clustering observed in the simulation box snapshots.

To explore the molecular interaction changes between the neat ionic liquids and in the various mixtures, RDFs were calculated between [BMIM]-[I] and [EA]-[NO_3]. Figures 4.1.3.2a and c are probability functions representing the cation-anion interactions in the neat ionic liquids (red lines) and in a 50/50 mixture of [BMIM][I] and [EA][NO_3] (gold lines). The [BMIM][I] cation-anion probability functions in panel “a” have a distinct shape and one defined peak but decrease in probability when forming mixtures with 50 mol% [EA][NO_3]. On the other hand, the ethylammonium nitrate cation-anion interaction shows a higher probability when in neat IL compared to in mixture, with a more distinctive and

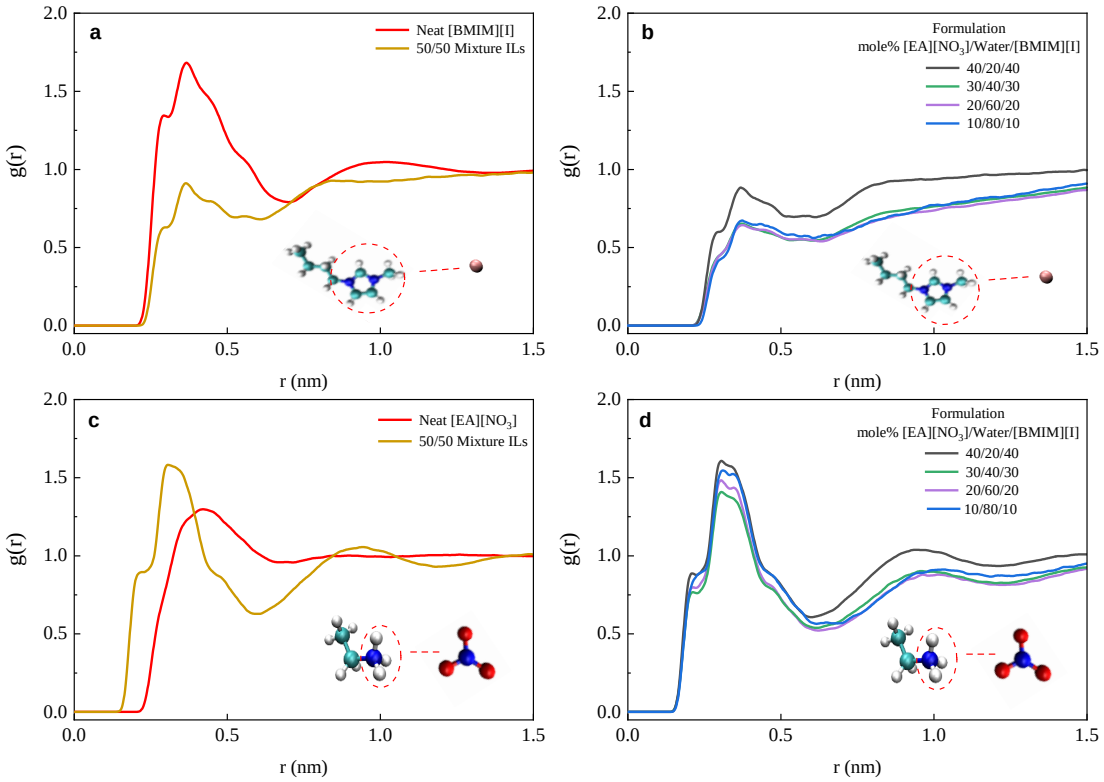

Figure 4.1.3.2: Radial distribution functions between the ions of the ionic liquids. (a) compares RDFs between neat [BMIM][I] and a 50/50 mixture of the ILs of the imidazolium ring and iodide. (b) compares RDFs between the imidazolium ring and iodide in formulations containing water. (c) compares RDFs of neat [EA][NO_3] and a 50/50 mixture of ILs of the [NH_3] cation and [NO_3]$^-$ anion (d) compared RDFs between the [NH_3] cation and [NO_3]$^-$ anion in formulations containing water

taller peak at a closer distance. The function for the 50/50 mixture also forms another peak, suggesting another nitrate anion is ~ 0.9 nm away from the center of the ethylammonium cation. The trends observed in panels “a” and “c” can be attributed to different molecular interactions occurring with the isolated ions. The decrease in probability of [BMIM]-[I] interaction from neat [BMIM][I] to 50/50 mixture is somewhat likely due to the interaction between ethylammonium and iodide as discussed earlier. This could segregate iodide ions from interacting with [BMIM] $^+$. However, the increase in probability for the [EA]-[NO_3] interaction demonstrated a shift where the ions are closer together possibly due to the change in density of the mixtures and an inherent change in the fundamental interactions between the ions where the [EA]+ cation is now interacting with iodide. In neat [EA][NO_3]

the ethylammonium cations have three oxygen sites on the nitrate to interact with, however in this mixure that may not be the case. The shift of interaction sites could also contribute to the change in the probability function. In panels “b” and “d”, water is introduced to the 50/50 IL mixture and the RDFs maintain the same overall shape and distance. For both neat IL cation-anion interactions, the RDFs decrease in probability with the increase of water concentration. Considering that the previous RDFs showed hydrogen bonding between iodide-water and iodide-$[EA]^+$, the trends in Figure 4b are to be expected since iodide is interacting with other molecules besides $[BMIM]^+$. The trends in Figure 4d show slight variation and decrease with respect to water concentration, however the interaction remains consistent within each mixture formulation suggesting that water concentration has little effect on the interaction, but the concentration of neat IL may have more influence.

The last interactions studied are between the [BMIM]+ cation and $[NO_3]^-$ anion. The snapshots in Figure 4.1.2.1 show possible interaction between the ions, hence RDFs between the imidazolium ring and nitrate anion were calculated and plotted in Figure 4.1.3.3. Each of the formulations, including the 50/50 ionic liquid mixture, show an interaction between the $[BMIM]^+$ ring and the nitrate anion at ~ 0.4 nm. The probability grows with increasing concentration of water in the formulations; however, there is a significant increase in the formulation containing 80 mol% water which suggests a change in the overall system at high water concentrations. The interaction also supports the RDFs from Figure 4.1.3.3c and 4.1.3.3d where the [EA]-[NO3] probability function shifts in formulations with [BMIM][I] and water. The [BMIM]-[NO3] interaction inhibits [EA]+

from hydrogen bonding with the three possible oxygens on the nitrate, therefore changing the interaction when compared to neat [EA][NO_3].

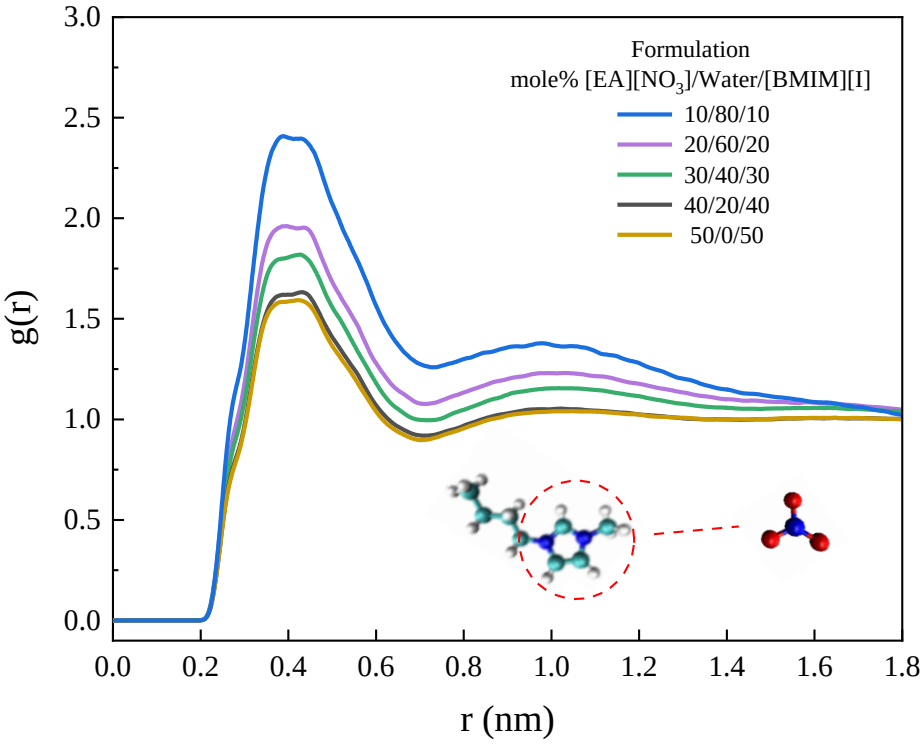

Figure 4.1.3.3: Radial distribution functions between the $[BMIM]^+$ imidazolium ring and nitrate anion.

The presence of this interaction suggests an anion exchange between the ionic liquid occurs in mixtures with and without water. Anion exchanges can be difficult to prove experimentally[188], therefore having the support of MD simulation results can further validate the occurrence. In this case, the anion exchange is likely a result of the attraction between iodide-water and iodide-ethylammonium, where iodide and ethylammonium are introduced to other competing interactions and $[BMIM]^+$ and $[NO_3]^-$ are left to form weak interactions. It may also contribute to the homogeneity of the 50/50 IL formulation.

4.1.4 Effects of Water Concentration and Molecular Interactions on Transport

Self-diffusion coefficients (SDCs) were calculated for each ion in all formulations and presented in Figure 4.1.4.1. To further explore the diffusion trends at higher water concentrations, SDCs of previous formulations and additional compositions with 70 and 90 mol% were included. In the 50/50 IL mixture with no water, the self-diffusion coefficients of constituent ions are all close together, except for iodide. This fits the homogeneity observed in the simulation snapshots where the ILs seem to be well mixed and the anion exchange characterized in Figure 4.1.3.3. With the introduction of water at 20 mol%, the iodide SDC is increased as it is most likely to form hydrogen bonding with

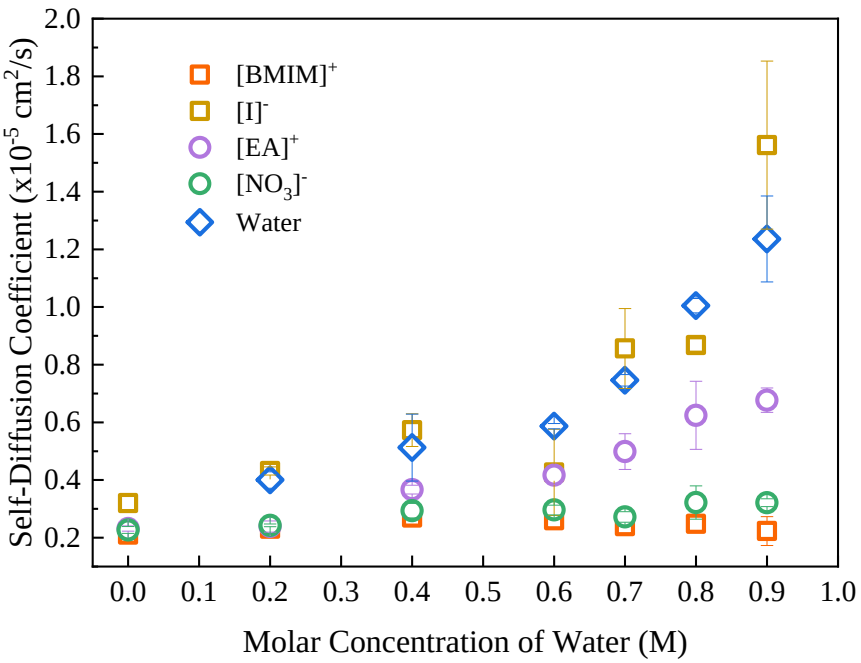

Figure 4.1.4.1: Self-Diffusion Coefficients for $[BMIM]^+$ (red), $[I]^-$ (gold), $[EA]^+$(purple), $[NO_3]^-$ (green), and water (blue) for each formulation studied from 0 to 80 mole percent water.

water, which was further supported through the radial distribution functions. At 40 mol% water the iodide and water SDCs continue to increase while the $[BMIM]^+$ and $[NO_3]^-$ SDCs do not vary much. In this formulation the [EA]+ cation SDC starts to break away from the lower SDCs and increase towards the middle of the set. At higher water concentrations the SDC increases but remains in between the two sets of ions. RDFs suggested that the $[EA]^+$

cation interacts with nitrate and iodide and is now reflected in the self-diffusion coefficients.

In almost all sets of SDCs the iodide anion and water molecules are diffusing together. This is supported through the radial distribution functions where the trends showed hydrogen bonding. Furthermore, it also supports the development of a water/iodide/ethylammonium network observed in the simulation snapshots suggesting that the ions are diffusing within their clusters formed with the increase of water concentration.

4.1.5 Structure-Property Establishment through Differential Scanning Calorimetry

Differential scanning calorimetry experiments were carried out to characterize the phase behavior of the mixtures in a temperature window of -140°C to 40°C in order to connect the simulations with experimental work. Specifically, the emphasis lies in explanation of first-order phase transitions observed in the mixtures which was previously hypothesized to attributed to formation of water aggregates or networks. Figure 4.1.5.1 shows the DSC results and corresponding simulation boxes highlighting only the water molecules within the mixtures. Formulations containing 0, 40, 60, and 70 mol% water were chosen to adequately display a range of phase behavior. By comparing the simulation snapshots and DSC curves directly, we can assess how the structure of the water aggregates may affect occurrence of crystallization and melting behavior.

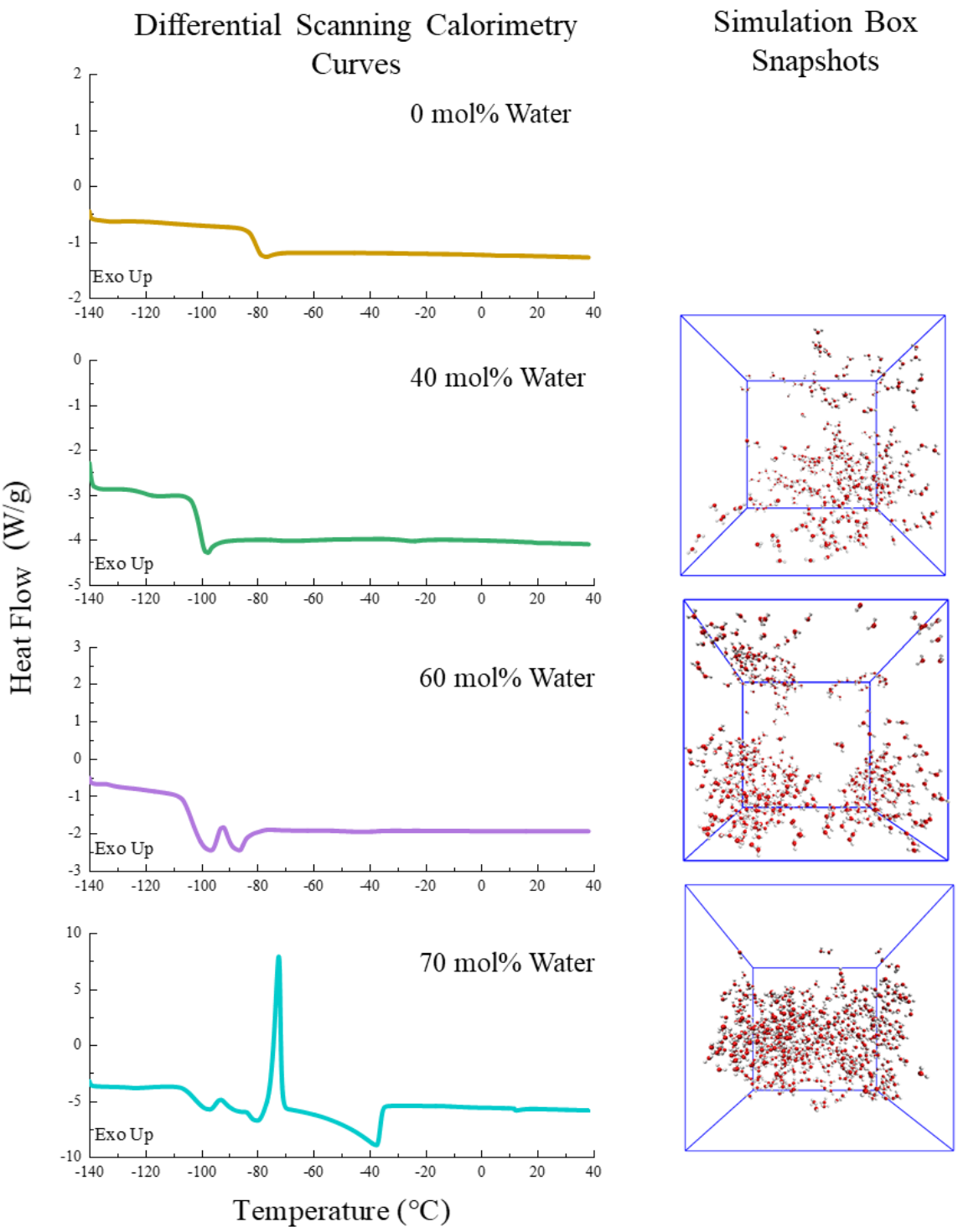

Figure 4.1.5.1: Differential Scanning Calorimetry (DSC) curves (left) of formulations containing 0, 40, 60, and 70 mol% water with the corresponding simulation boxes (right) displaying only water molecules.

The left panel of Figure 4.1.5.1 are the DSC curves of 4 formulations with increasing concentrations of water. The 50/50 mixture of ionic liquids (gold curve) displays a typical thermal behavior of IL mixtures, where a clear glass transition was identified at around 80 °C without other events at higher temperatures. Several ILs are known as glass-forming liquids and only exhibit glass transition due to bulky and asymmetric ions that inhibit crystallization.[138,140,189] Even at 40 mol% water (green curve), only the glass transition has been observed but at a much lower temperature ~ -100 ˚C. Such an effect has been discussed in our previous work, attributed to solvation effect of water around iodide that effectively decrease the cohesive energy of the mixture. The corresponding simulation box displays well dispersed water molecules due to intermolecular interactions, supporting absence of first-order phase transitions from the thermogram. At 60 mol% water (purple curve), recrystallization and melting peaks started to emerge at temperatures higher than Tg despite weak. In the corresponding simulation box, small water aggregates have formed, resulting in heterogeneity of the mixture with phase transitions of several regimes identified at different temperatures.. Finally, at 70 mol% water, in addition to the glass transition, several heat flows were captured with a distinct recrystallization peak at -75 ˚C, followed by the melting peak at -38 ˚C. Compared to the 60 mol% simulation box, significant evolution in molecule configurations was observed even with just an additional 10 mol% of water, as evident by the prominent water cluster. At this formulation, there were not enough iodide for water to interact with, and hence an abundance of water molecules started to form aggregates or networks that resulted in prominent phase transition over the broad temperature range. Furthermore, there seemed to be a progression of the water network formation, which was reflected in the DSC curves where more phase

transitions occurred with higher corresponding heat flow only when passing a certain composition threshold. This implies the high complexity of intermolecular interactions in the ternary mixtures and the significance of achieving a balanced molecular dynamic of all constituent species for electrolyte optimizations.

The direct comparison of the DSC curves and simulation boxes demonstrates the structure-property relationship of IL-based mixtures. Specifically, in ternary systems of [EA][NO_3]/water/[BMIM][I], the first-order phase transition behaviors were governed by configuration of water, which determine the operating temperature window of respective mixtures. While we have established a connection and validated the hypothesis of correlation between water and 1st order phase transitions from our previous experimental study[190], the MD simulations can be even more impactful for future electrolyte development. From MD simulations, we can easily identify the composition transition point where water aggregates start to be prominent enough to affect thermal properties of the mixtures. Such an insight can direct electrolyte optimization and even be extended to other physicochemical properties, for instance, SDCs for transport behaviors. Moreover, the computational results support the experimental observations over a broad temperature range effectively despite simulations at room-temperature with simple SPC/E for water model. Further studies with more complex models can be built upon these findings with consideration of relevant environmental parameters such as temperature and pressure to draw stronger correlations and strengthen these types of MD simulations as predictive tools.

4.2 Glass Transition Temperature Predictions of Imidazolium-based Ionic Liquids

4.2.1 Identification of Glass Transition Region

MD simulations have been employed to predict glass transition temperatures in the past, however, the effects of parameters such as simulation box size and annealing rate have not been systematically studied and have not been extended to include [BMIM][I]. The initial prediction method utilized in this study is the monitoring of potential energy per ion pair vs temperature. Theoretically, the slope of the potential energy plot vs temperature should be linear. In the case of a phase change, the linearity breaks indicating a change in energy and possible phase change. This method was chosen to allow for in depth analysis and to maintain precision in predictions. An OPLS-AA forcefield was chosen as parameters for imidazolium-based ionic liquids have been improved and are specific to this class of ionic liquids.

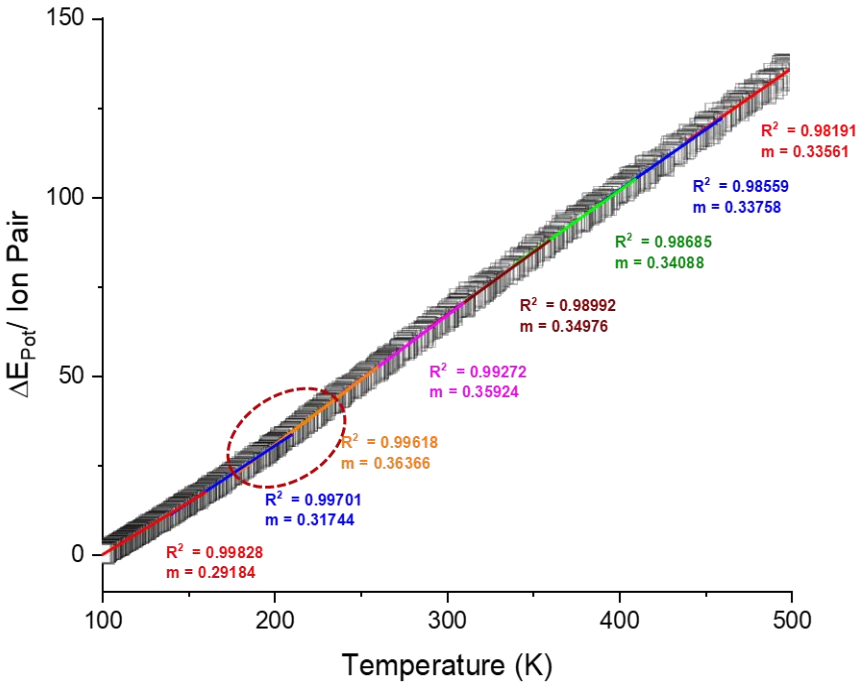

Figure 4.2.1.1: ΔE_{Pot}/Ion Pair (kJ/mol) vs Temperature (K) plot from an annealing simulation of neat [BMIM][I] with linear fits of 50K segments.

A defining question we wanted to answer in this investigation was "what determines a break in linearity when monitoring the potential energy slope?". In order to answer this question, potential energy vs time data from a simulated annealing of neat [BMIM][I] from 500K to 100K at an annealing rate of 20K/ns was plotted. Slopes and R^2 values were taken from parts of the graph to determine if there are significant changes between segments of the plot. Figure 4.2.1.1 depicts the annealing data with the R^2 values and slopes from linear fittings are shown for 50K segments. R^2 values for all segments show that each segment is linear, and the fitting is acceptable. From 500K to ~250K the slope changes are very gradual and small, however, there is a noticeable change between the orange segment and dark blue segment, highlighted with the red circle. At this point, the slope changes from 0.363 to 0.317, a more drastic change than the other segments. This

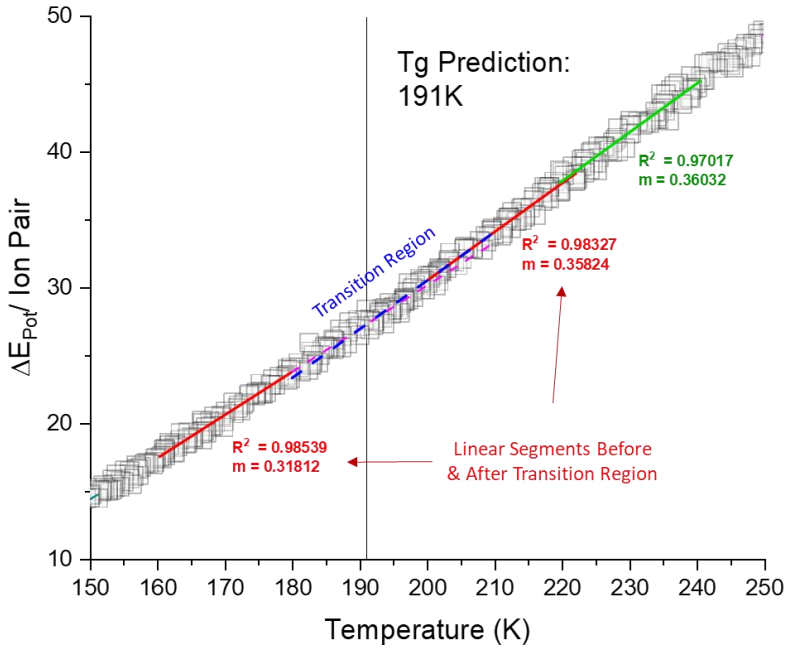

Figure 4.2.2.1: ΔE_{Pot}/Ion Pair (kJ/mol) vs Temperature (K) plot from an annealing simulation of neat [BMIM][I] focused on 150K to 250K temperature range. Red linear fits are segments before and after the transition region, demonstrating a significant change in slope. Blue and pink dashed lines are the extrapolated fits from the red lines. Pink is from the low temperature fit while blue is from the higher temperature fit.

is most likely where the glass transition is occurring, but to more accurately predict the Tg, smaller linear segments need to be applied.

4.2.2 Method for a Robust Glass Transition Temperature Prediction in [BMIM][I]

Figure 4.2.2.1 is a "zoomed in" version of the previous figure where a 100K portion, 150K to 250K, of the plot has been chosen to fit smaller linear sections. The green line is a 20K segments that is before the glass transition. The two red lines are 20K segments before and after the glass transition, and the blue and pink lines represent the "transition region". The "transition region" is here defined as a 20K temperature window where the glass transition temperature lies. The prediction is done by extrapolating linear fits of the red segments and identifying where they intersect. Here, they intersect at 191K, therefore the Tg prediction of neat [BMIM][I] is 191K, or -82.15 °C. The Tg of [BMIM][I] provided through experimental techniques is -67.4 °C, which shows that the model predicts the Tg at a lower temperature than the experimental value. The over prediction is most likely die to the difference in cooling between the experimental technique and simulation. Simulated annealing is a controlled cooling, while experimentally it is difficult to achieve the same. Overall, the model does predict an accurate transition region of 180K-200K.

4.2.3 Effects of Simulation Box Size and Cooling Rate on Glass Transition Temperature Predictions

Table 4.2.3.1: Predicted glass transition temperatures for neat [BMIM][I] with varying box lengths and annealing rates compared to experimental Tg.

	Exp. Tg	Box Length		Annealing Rate		
		6nm	5nm	10K/ns	20K/ns	30K/ns
Tg Prediction (°C)	-67.4	-87.65	-82.15	-87.15	-82.15	-106.15

Simulations with varying box sizes and annealing rates were also carried out to evaluate the effects of simulation parameters. Again, using neat [BMIM][I], annealing simulations were carried out with a constant annealing rate of 20K/ns and in boxes with box lengths of 5nm and 6nm. Unfortunately, box lengths of 4nm and 7nm were not suitable for the simulations. Annealing simulations with rates of 30K/ns, 20K/ns and 10K/ns were done with constant box sizes of lengths of 5nm. The predicted Tgs from the simulations are reported in table 4.2.3.1. The Tgs were predicted with the same methodology demonstrated in figure 4.2.2.1 There is ~5K difference in the predictions when box lengths and annealing rates are changed between the two lowest annealing rates, indicating that the parameters may not contribute largely to the prediction of glass transition temperatures. The difference may also be due to slight differences in the designation of the glass transition regions. There is a large change in the prediction at the 30K/ns annealing rate. At this rate, the system may not be well equilibrated at the annealing points and therefore the prediction is not as accurate. While the simulations over-predict the glass transition temperatures, the results indicated that they do in fact predict accurate glass transition regions at lower annealing rates. For [BMIM][I] the predicted glass transition region is between 180K-200K. Moreover, validation of these methods gives way to investigate trends of transport properties and molecular interactions throughout the simulations.

4.2.4 Investigation of Temperature Effects on Transport Properties and Molecular Interactions of Neat Ionic Liquid [BMIM][I]

Figure 4.2.4.1 are plots of self-diffusion coefficients (left) of [BMIM] [I] ions and radial distribution functions of the ions as a function of temperature. The self-diffusion coefficients (SDCs) show a stead decreasing trend from 500K to 100K. At a point, the

SDCs stop decreasing and reach a plateau most likely after the glass transition temperature as been reached. Tg predictions using SDCs have been done, however, our SDCs are averaged over a set time in the simulation, which can give variability in the Tg prediction.

The radial distribution functions between the cation and antion slowly increase with decreasing temperature. Considering the trend of the SDCs, this interaction is probably affected by the diffusion of the ions, hence an increase in probability when the SDCs are very low. The molecules diffusion is limited, making their interactions more probable. Notable, the second peak shifts slightly closer to the center of mass of the other ion. In this case the peak shift is most likely due to the change in density of the system at lower temperatures, however it seems to not change the interactions until very low temperatures.

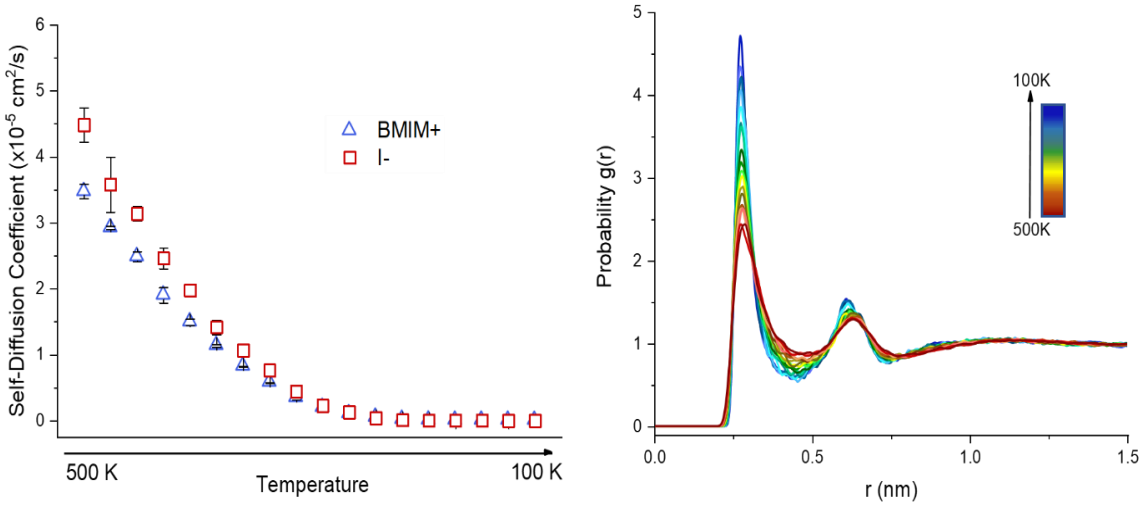

Figure 4.2.4.1: Plotted self-diffusion coefficients (left) and radial distribution functions (right) for $[BMIM]^+$ and $[I]^-$ averaged over 20K segments from 500K to 100K.

4.3 Computational Studies of the Stability and Reactivity of Atomic Layer Deposition Precursors

4.3.1 Reaction Mechanism via Cluster Model

To understand if possible ALD precursors are good candidates for deposition and to optimize existing precursors, reaction and activation energies were calculated through DFT. For quick and accurate results, precursors are modeled to react with a hydroxyl terminated SiO_2 cluster. The SiO2 cluster represents a reaction on an isolated active site of a Si(1 0 0) surface without needing to model the reaction with high surface coverage. This practice allows for the investigation of reaction mechanisms without influence from surrounding atoms.[191–193] Figure 4.3.1.1 is an example of the SiO_2 cluster and $SiH_3(NMe_2)$

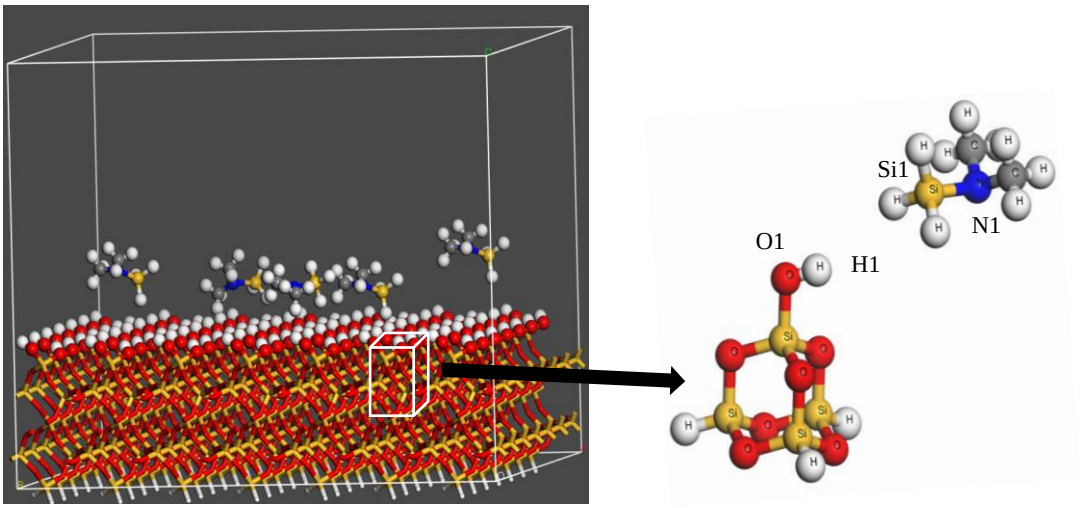

Figure 4.3.1.1: Demonstration of how cluster models represent small sections of reactive surfaces (white box) and the cluster model used in this work with labeled atoms.

precursor used in the calculations. The white box shows how a small part of the Si(1 0 0) surface is transformed into the cluster model. Here, the cluster containing $Si_4O_7H_4$ is considered small, yet still large enough to use for the purpose of this study and is comparable to other investigations that implement small surface clusters.[191,194,195]

The cluster model is utilized to calculate a reaction mechanism for the reaction between the cluster and the selected aminosilane precursors. Figure 4.3.1.2 is an example of the reaction mechanism between a $H_3Si(NH_2)$ precursor and SiO_2 hydroxyl terminated cluster where the isolated reactants, products, transition state, and pre and post van der

waals complexes are shown. Initially, the isolated precursor has a N1-Si1 bond length of 1.742Å, however in the pre reaction van der waals complex, complex II, the bond distance increases slightly to 1.778Å and the precursor is positioned for N1 to hydrogen bond with H1, while Si1 is in position almost on top of O1 at a distance of 3.839Å. At the transition state, N1 has bonded to H1 and is simultaneously bonded to Si1. The bond distance between Si1 and N1 increases to 1.911Å and the distance between Si1 and O1 decreases significantly to 2.367Å. Once the post reaction van der waals complex is reached on the pathway, the Si1-N1 bond has broken and Si1-O2 has formed, with a bond distance of 1.691Å. In the isolated products that bond distance decreases slightly to 1.677Å.

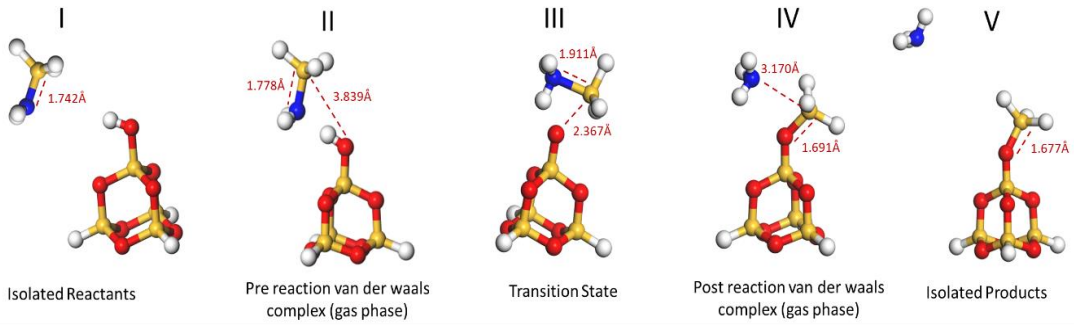

Figure 4.3.1.2: Reaction mechanism between $H_3Si(NH_2)$ and SiO_2 cluster. Complexes included are the isolated reactants (I), pre reaction van der waals complex (II), transition state (III), post reaction van der waals complex (IV), and the isolated products (IV)

4.3.2 Reactivity of Mono and Bis Precursors

To directly compare the reactivity of the mono and bis precursors, a reaction coordinate graph was generated in figure 4.3.2.1. Each energy state of the SiO_2 cluster and selected precursor is denoted by a roman numeral that matches the states in figure 4.3.1.2. A major area of interest when screening ALD precursors is the activation energy barrier required for the reaction to carry out successfully. In figure 4.2.1.2 the activation energy (E_A) is shown as the difference in energy between the pre-reaction van der waals complex

and transition state (complexes II & III). The blue line denotes the reaction coordinates of the H_3SiNH_2 precursor and the SiO_2 cluster where the E_A is 27.1 kcal/mol. This is a significant reaction barrier to overcome, especially without a catalyst and under normal ALD conditions. Adding an alkyl chain to the amine group of the precursor has been proven to lower the reaction barrier on an Si (1 0 0) surface to an extent.[137,196,197] The same phenomenon is observed in our results when comparing the activation energy barriers between mono-aminosilane and bis-aminosilane ligands. Starting with substituting the hydrogens on the amine to methyl groups (DMAS), the activation energy barrier is lowered by ~7 kcal/mol, shown in orange. Substituting two of the hydrogens on the Si for amines, shown as $H_2Si(NH_2)_2$ in a green line, significantly lowers the barrier to ~14 kcal/mol and

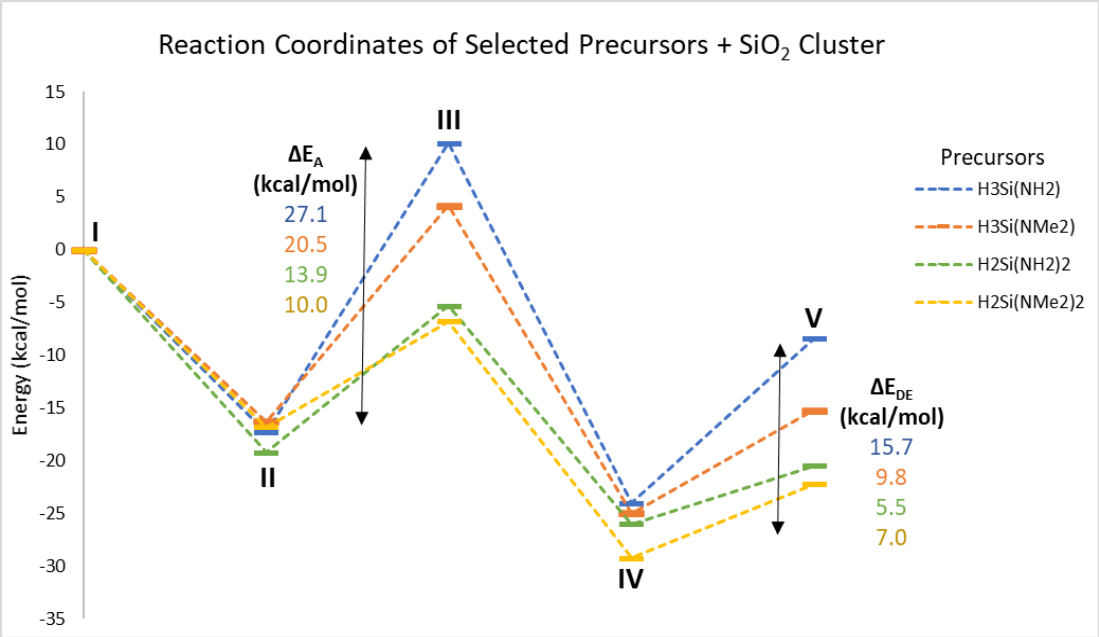

Figure 4.3.2.1: Reaction coordinates, activation energies (E_a) and desorption energies (E_{DE}) of reactions between the SiO2 cluster and selected aminosilane precursors

is further lowered by the use of $H_2Si(NMe_2)_2$ (BDMAS), shown in the yellow line.

Another area of focus is the desorption between complexes IV and V where the post-reaction van der waals complex separates into an isolated product. This is a crucial step in ALD as the byproduct will have to be removed from the system.

Similar to the trend of the activation energies, the substitution of hydrogens on the silane of the precursor to more amines or methyl groups lowers the desorption reaction barrier. However, this is only to an extent as the lowest post-reaction energy barrier is that with the $H_2Si(NH_2)_2$ precursor with a value of 5.5 kcal/mol and is raised slightly to 7.0 kcal/mol when $H_2Si(NMe_2)_2$ is used.

The viability of related aminosilane precursors with varying ligands was further investigated through reaction energies and activation energies with respect to reactant energies. These calculations reflect three states of the reaction: the isolated reactants, transition state, and isolated products. The reported activation energies, shown in table 4.3.2.1 reflect the 3 chosen states and do not include adsorption and desorption energies in order to quickly and easily screen the effects of amine ligands on the silane precursor reactions with the SiO_2 cluster.

The $H_3Si(NX_2)_2$ group of precursors, highlighted in the green section of the table where X=H,Me,Et,iPr, show a decrease in reaction energy and reaction barriers with the SiO_2 cluster. With the substitution of a hydrogen on the silane to an amine group, the

Table 4.3.2.1: Reaction and activation energies, with respect to isolated reactants, of reactions between the SiO2 cluster and aminosilane precursor families.

Precursor	$H_3Si(NH_2)$	$H_3Si(NMe_2)$	$H_3Si(NEt_2)$	$H_3Si(NiPr_2)$
E_{RXN} (kcal/mol)	-8.4	-9.4	-14.4	-15.2
E_A (kcal/mol)	10.1	4.2	-2.9	-5.4
Precursor		$H_2Si(NMe_2)_2$	$H_2Si(NEt_2)_2$	$H_2Si(NiPr_2)_2$
E_{RXN} (kcal/mol)		-22.2	-29.8	-35.2
E_A (kcal/mol)		-6.8	-4.3	-3.7
Precursor	$H_2Si(NH_2)_2$	$H_2Si(NHMe)_2$	$H_2Si(NHEt)_2$	
E_{RXN} (kcal/mol)	-20.5	-24.5	-24.0	
E_A (kcal/mol)	-5.3	-5.1	-5.5	

$SiH_2(NX_2)_2$ group highlighted in blue where X=Me,Et,iPr, the reaction energy continues to decrease steadily, although the reaction energy barriers seem to have reached a plateau suggesting that the addition of an amine and increasing the alkyl chain on the amines may decrease reaction energies but not have a large effect on the reaction energy barrier. Now substituting a hydrogen in for an alkyl chain on the amino groups, the $H_2Si(NH_2)_2$ group in orange, has a small effect on reaction and activation barrier energies compared to the

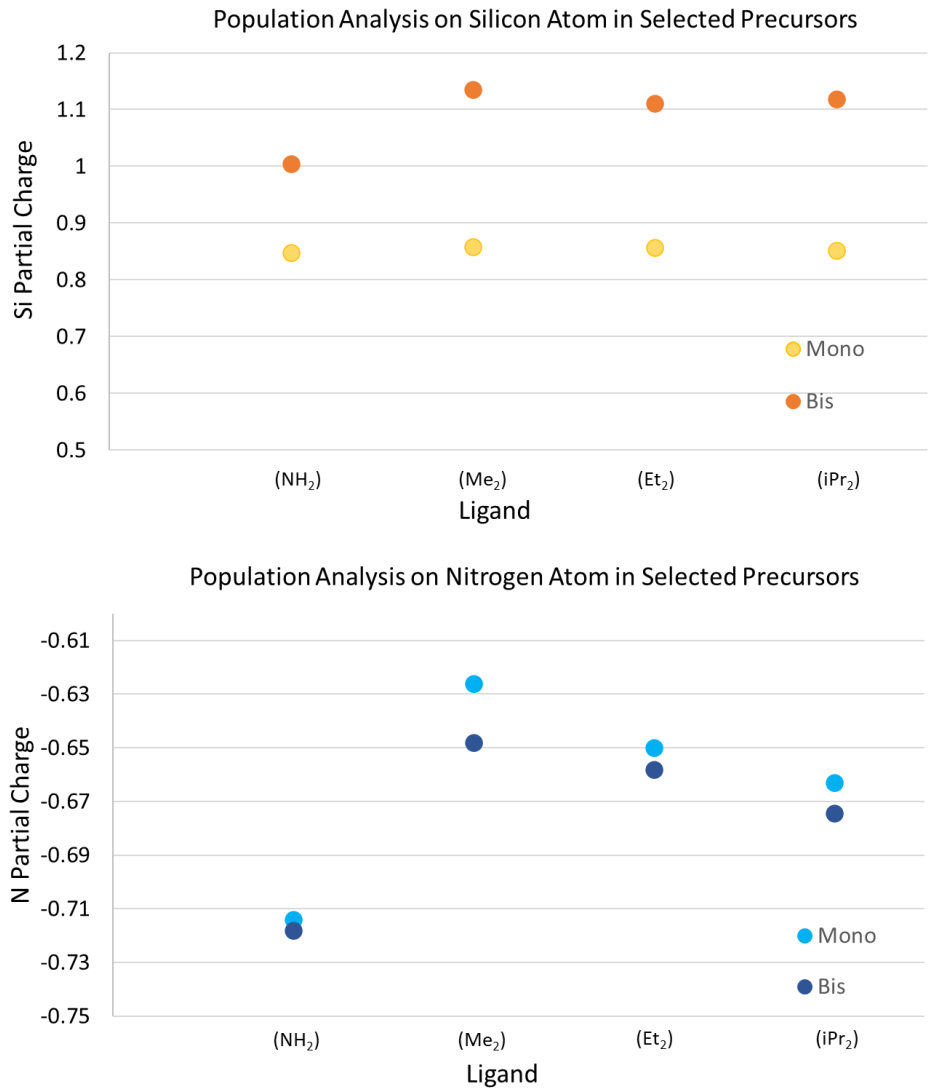

Figure 4.3.2.2: Population analysis on mono and bis aminosilane isolated precursors. Top panel is partial charges of the silicon atom while the bottom panel are partial charges of the nitrogen atom. All charges shown are Mulliken charges.

blue and green groups. The reaction energies drop ~4 kcal/mol and the activation energies remain constant around 5 kcal/mol.

To investigate the drop in activation energy with respect to the mono and bis substituted precursors, a population analysis was performed on the isolated precursors and the results are plotted in figure 4.3.2.2. All partial charges are Mulliken charges, however Hirshfield charges were also calculated and displayed the same trends. The top panel shows the partial charges on the silicon atoms for selected precursors. The mono aminosilane precursors (yellow markers) show a consistent trend with the increased alkyl chain length of the ligand. When a second ligand is added to create the bis aminosilane precursors, the silicon partial charge (orange markers) increases and become more positive when compared to the monoaminosilanes. The increase makes the silicons more electrophilic and thus stabilizing the transition state and lowering the activation energy barrier further. The partial charges of the nitrogen atoms (bottom panel) do not show the same trend. In fact, there is little variation between the partial charges of the nitrogen atom of the mono and bis aminosilanes. Thus, the stabilization of the transition state is most likely due to the electrophilic nature of silicon in the bis substituted aminosilanes.

It is important to note that although the bis-aminosilane precursors significantly lower the reaction energy barrier, the product of the reaction will have a mono-aminosilane bonded to the reactive surface instead of a silane. This requires a second amine elimination that can be difficult to carry out or may need intervention of other methods.[196]

4.3.3 DFT calculations determining Precursor Thermal Stability for Scale Up Engineering

Precursor thermal stability is considered during the ALD process to ensure that the precursor will not decompose in the ALD environment leading to parasitic CVD.

Moreover, the parameters derived from the thermal stability calculations are used for scale-up simulations conducted in the Aspen program.

Thermal properties were investigated through the computation of the heat of formation (ΔH_f) and Gibbs free energy of formation (ΔG_f). Reported are the ΔH_f and ΔG_f values of the selected precursors calculated from 2 computational program's thermochemical recipes: G3MP2 (Gaussian09) and T1 (Spartan'18). The Gaussian09 G3MP2 thermochemical recipe utilizes multiple calculations to get extremely accurate energies that are required for the thermodynamic property calculations but it may not feasible for larger molecules due to its extreme need for computational resources (disk space, memory and CPU time). The calculation steps of the G3MP2 thermochemical recipe are as follows: 1. HF/6-31G(d) geometry optimization, 2. HF/6-31G(d) frequency calculation, 3. MP2/6-31G(d) geometry optimization, 4. QCISD(T)/6-31G(d) energy calculation, and 5. MP2/6-311+G(3df,2p) energy calculation. After calculating the total

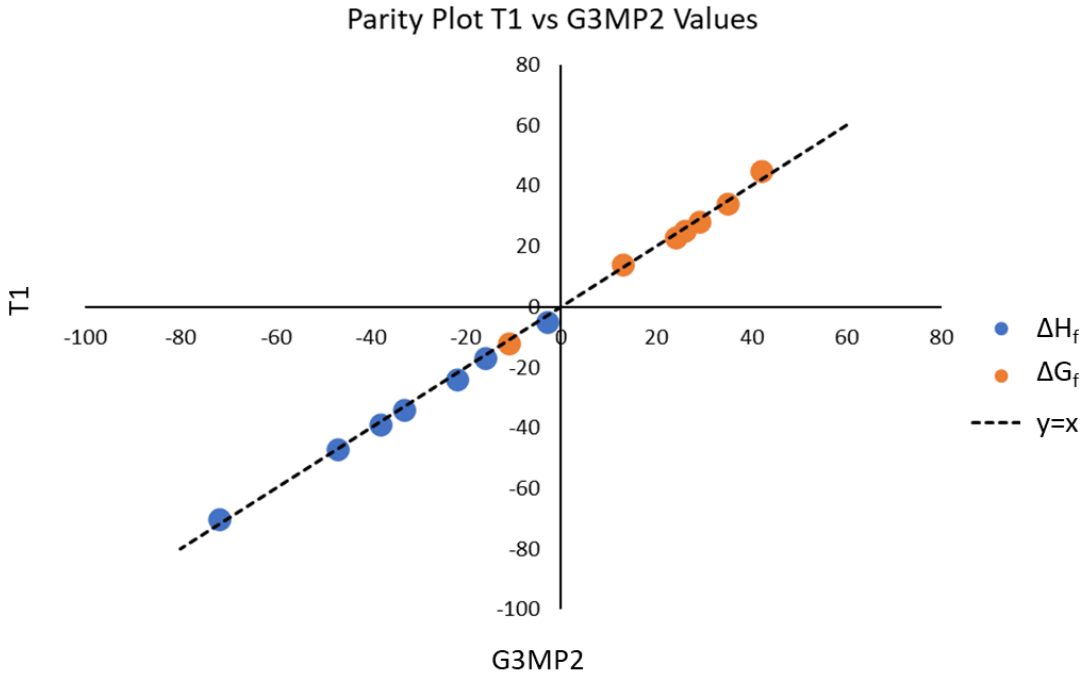

Figure 4.3.3.1: Parity plot of ΔH_f (kcal/mol) and ΔG_f (kcal/mol) values comparing G3MP2 and T1 thermochemical recipes

energy, energies for the gas phase atoms in the molecule are also evaluated and the atomization enthalpies and Gibbs free energies are calculated. Finally, the enthalpy of formation and Gibbs free energy of formation is evaluated by completing the Hess cycle by including the experimentally available atomization enthalpies and entropies of the constituent elements. The T1 recipe follows a similar process to calculate the enthalpy of formation; however, it is significantly less computationally intensive and has proven to be comparable in terms of accuracy with G3MP2 ΔH_f values.[147] The T1 thermochemical recipe is a shorter calculation series consisting of 1. HF/6-31G* geometry optimization, 2. RI-MP2/6-311+G(2d,p)[6-311G*] energy, and 3. Empirical correction. The T1 recipe has been empirically parametrized so it is important to benchmark it for specific classes of compounds, such as aminosilanes as our compounds of interest. In order to also obtain the Gibbs free energies of formation at this level, thermal contributions were calculated using density functional theory (specifically, BLYP/DNP as implemented in Dmol^3 in Materials Studio).

Figure 4.3.3.1 is a parity plot of the ΔH_f and ΔG_f values in kcal/mol from both the G3MP2 and T1 thermochemical recipes. The values are in good agreement with the linear y=x line, proving that the T1 method is reliable to predict the thermodynamic properties for this set of aminosilane precursors. When screening ALD precursor candidates, the thermodynamic values are used in scale up calculations to determine viability in the ALD environment. From a quantum chemistry perspective, we can make general comments on the values. Positive ΔG_f values indicate a non-spontaneous reaction to form the molecules from its constituent elements. There is one ΔG_f point that is negative, indicating that the precursor may prove to be difficult in handling for testing experimentally, as it will not be

stable for transportation. Furthermore, the ΔH_f values demonstrate exothermic behavior with the exception of one point that is close to zero and, again, indicates that particular precursor may be difficult to work with. Therefore, the stability studies aid to ensure proper safety measures are taken during experiments.

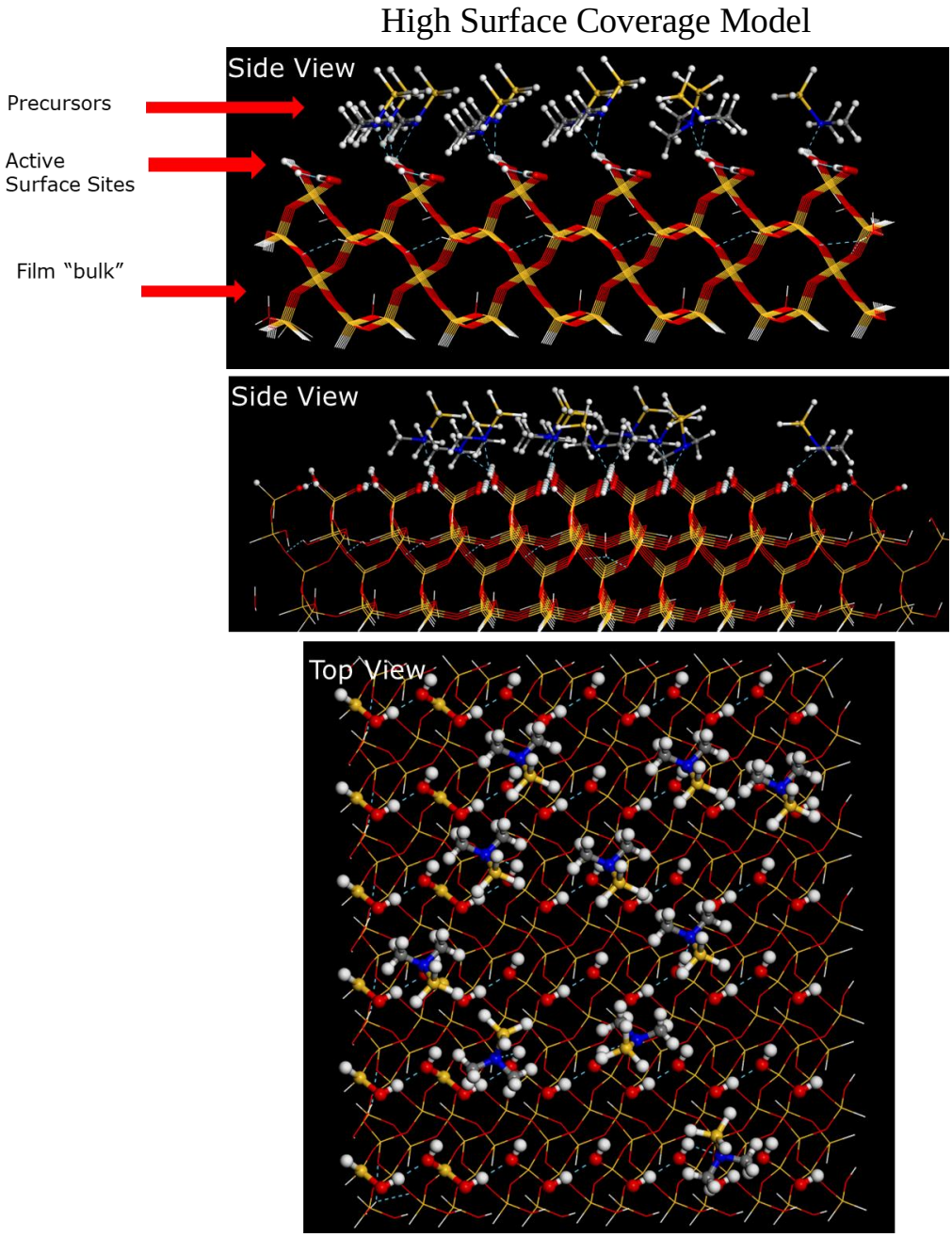

Figure 4.3.4.1: Initial structure of SiO_2 surface model with mono aminosilane precursors positioned similarly to the pre-reaction Van Der Waals complexes. Displayed are two side views and one top view.

4.3.4 Investigation of ALD surface reactivity with selected precursors through semi-empirical calculations

While cluster models and slab models give incredible insight to the reactivity of ALD precursors and are crucial to the optimization and development of such precursors, there is an opportunity to expand the surface coverage of the models through semi-empirical tight binding calculations. Semi-empirical tight binding methods approximate the Hartree-Fock integrals implemented in *ab-initio* and DFT calculations and as a result the calculation time is significantly decreased, and more atoms can be added to a system without sacrificing accuracy in the ideal implementation.

Here, we present an initial test to utilize the XTB-GNF2 tight binding program as a means for ALD surface expansion calculations. The model, shown in figure 4.3.4.1, is a 1000 atom SiO_2 hydroxyl terminated surface with 10 $H_3Si(NMe_2)$ (DMAS) precursors dispersed above the surface. The top panel of figure 4.3.4.1 shows how the precursors are positioned such that they are most likely to react. In order to give the highest chance of capturing a reactive trajectory, the precursors were placed in a van der Waals pre-reaction complex type position. Below the precursors are the O-H active sites that will be the focus for the reactive trajectories. Below the active sites is a continuation of the film to represent the “bulk” phase. The size of this model exceeds that of larger slabs typically employed in ALD surface calculations, moreover the inclusion of multiple precursors and active sites gives insight into the number of reactive trajectories in a simulation and possibly growth per cycle of the film while undergoing the ALD cycles. The results from this model capture the 1st cycle in the ALD process, which is the formation of Si-H species on the surface of the film after amine elimination.

As the next step in the testing process, a geometry optimization was carried out on the initial structure to see if the optimization will converge and what the program will dictate is a minima on the potential energy surface (PES). To maintain the conformality of the film, all oxygens were constrained, and the temperature was set to 300K. Figure 4.3.4.2

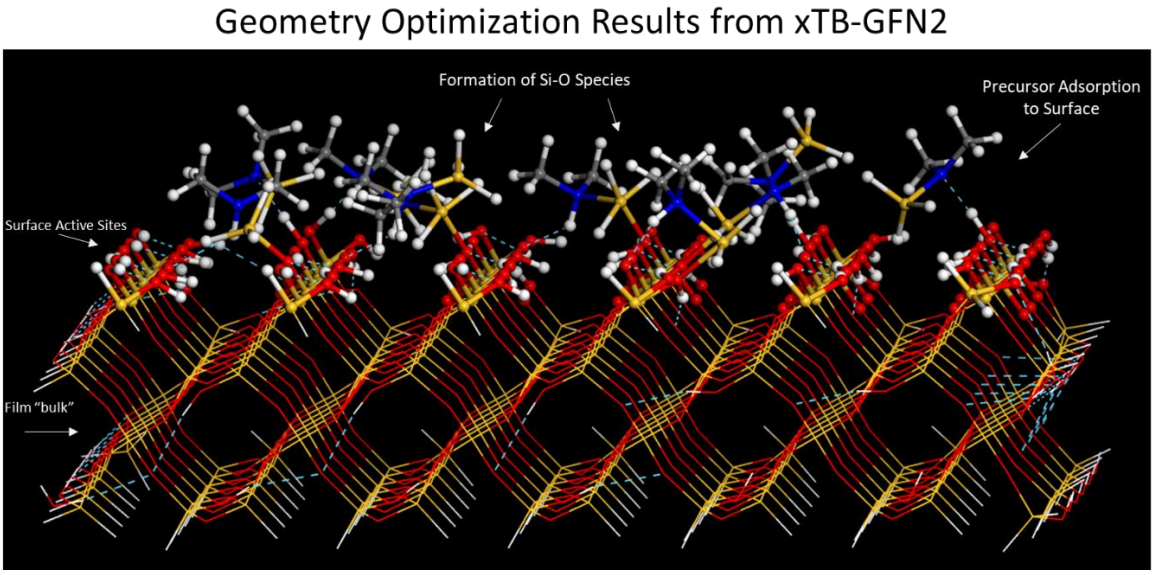

Figure 4.3.4.2: Structure of model after geometry optimization in xTB-GFN2 at an electronic temperature of 300K. Within structure are multiple precursor-surface complexes identified to be adsorbed to the surface or bonded to the surface.

displays the final optimized structure with highlighted active surface sites and precursors. There are multiple complexes identified within the structure including healthy precursor-surface adsorption and unexpected Si-O bonding creating a penta-coordinated silicon. To further investigate the different structures, the complexes were isolated and displayed in figure 4.3.4.3.

In figure 4.3.4.3 there are three highlighted structures from the geometry optimization results. Panel "a" shows a likely adsorption between the precursor and surface where the nitrogen of the precursor is hydrogen bonded to a hydrogen on an active site. This is further supported through the Si-N bond length of ~1.8 Å and N-H bond length of ~1.6 Å. The structure in panel "a" is probable as a minimum on the PES. However, the

structures in panels “b” and “c” are less likely to occur on the PES due to the coordination structure around silicon. In panel “b” the amine has been protonated with a hydrogen from the surface and the silicon from the same precursor has bonded with the oxygen. The Si-O bond length is ~1.8 Å demonstrating a clear bond between the two atoms. The Si-N bond length is ~1.9 Å which is strained compared to the Si-N bond length of ~1.7 Å of the isolated precursor. The structure in panel “c” shows a similar trend to that in panel “b” with the exception that the oxygen active site is still protonated and the Si-O bond length is increased. To validate the existence of the structures in panels “b” and “c” a minima on the PES, DFT calculations were performed using the BLYP functional and DNP basis set. The structures were taken directly from the xTB-GFN2 optimized structures and scaled down to only include the precursor and small cluster for the active site. The DFT geometry optimizations displayed dissociation of the amine from the silicon and therefore the structures from the xTB-GFN2 program are likely not real minima. This could mean that

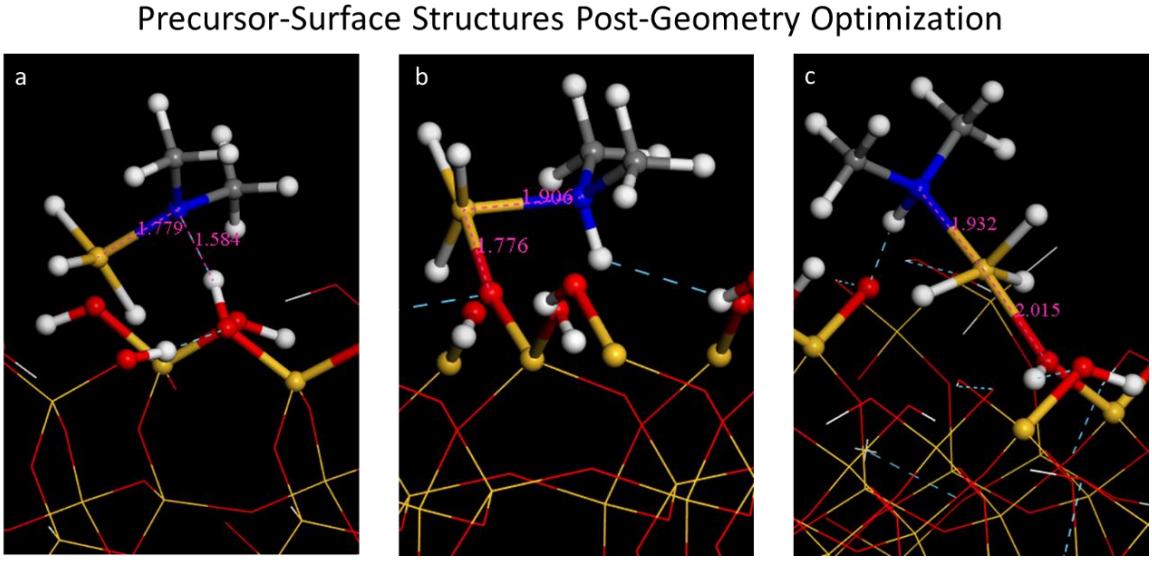

Figure 4.3.4.3: Isolated structures with related bond lengths (pink) from geometry optimization result. Panel “a” displays an adsorbed DMAS precursor to the SiO_2 surface, panel “b” shows a penta-coordinated silicon bonded to the surface oxygen with a protonated amine group, and panel “c” shows another penta-coordinated silicon bonded to an O-H surface site with a protonated amine group.

the version of the program is not correctly parameterized for the system that we are testing. Nonetheless, further testing of the program was done through DFT-MD simulations.

DFT-MD simulations will ultimately determine the properties of interest such as the precursor-surface interactions at high surface coverage. The final optimized geometry from figure 4.3.4.3 was used as the initial structure for the MD-DFT simulation. It was carried out at 600K for 5 ps. Typically, 10 ps or higher is more adequate time for DFT-MD simulation, however, the program took a considerable amount of time to run the DFT-MD. The final structure from the DFT-MD run is displayed in figure 4.3.4.4 where the various species are labeled. Overall, there were four reactive trajectories that resulted in the creation of the Si-H fragments at the SiO_2 surface which is the desired product of the first half reaction in the ALD process of interest. In other words, 40% of the precursors reacted favorably. The other 60% either stayed physisorbed at the film surface or repelled from it

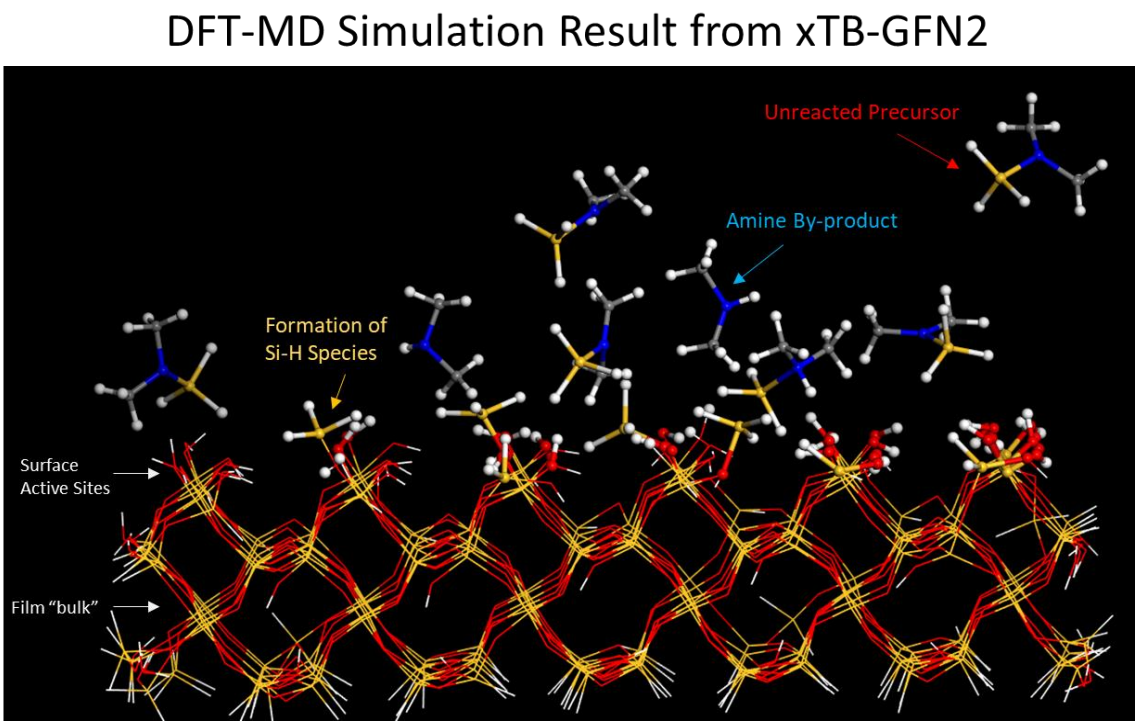

Figure 4.3.4.4: Result from 5 ps MD-DFT simulation in xTB-GFN2 using the optimized structure from Figure 4.3.1.3. Final structure indicates formation of Si-H species, amine by-produce and unreacted precursors.

and remained unreacted. Also, the amine by-products tended to move away from the surface after reaction. These results from the DFT-MD simulation are encouraging for implementation of the program and give realistic situations where some precursors react with the precursors and others do not.

The simplicity and performance of xTB-GFN2 initially attracted us to the implementation for further investigation of precursor-surface interactions via a high surface coverage model. The initial testing of the model including geometry optimizations and DFT-MD simulations reveal high potential for the use of xTB-GFN2 in an industry setting, however more testing needs to be done. The geometry optimizations displayed artifacts that may not realistically exist as a minima on the PES. The DFT-MD simulations displayed encouraging results but are computationally expensive. With more testing of the xTB versions and some improvement in the parametrization by the developers, it may be enough for industrial implementation. More testing will be required to fully adopt the method as a screening tool for ALD precursors.

CHAPTER

5. SUMMARY

In this dissertation, we have reported the results from investigations of functional materials through computational methods focused on atomistic and quantum calculations. The studies represent the capabilities and potential of emerging computational programs and methods to continue to contribute to the field of functional material development with respect to ionic liquid electrolytes and atomic layer deposition precursors.

In Chapter 4.1 we explored the properties of a [BMIM][I]/water/[EA]NO_3] system with increasing water concentration through molecular dynamics simulations. The experimental and simulation densities are in good agreement and validate the chosen OPLS-AA forcefield, which allows for an in-depth investigation of the systems. Simulation box snapshots show a homogeneous mixture in a 50/50 IL mixture, however, as the concentration of water is increased the snapshots show the development of heterogeneous mixtures where water starts to dominate. Radial distribution functions between iodide and water, and iodide and ethylammonium demonstrate hydrogen bonding in both interactions. Furthermore, the radial distribution functions between the IL constituents in their neat state and in mixture show consistent trends, except for high concentrations of water where the molecular interactions start to shift. The radial distribution functions between the $[BMIM]^+$ cation and $[NO_3]^-$ anion display evidence of an anion exchange between the ionic liquids that is evident in the 50/50 IL mixture and increases in probability as the concentration of water is increased within the formulations. Self-diffusion coefficients display a shift in the transport of the ions that are consistent with the simulation box snapshots and radial distribution functions, therefore further proving a change in molecular interaction in

formulations containing > 60 mole percent water. Differential scanning calorimetry (DSC) experiments supplemented these results by showing the thermal behaviors of the mixtures above the glass transition where thermal crystallization and melting phase changes can occur. Selected simulation boxes highlighting the water molecules in the mixtures were compared to the DSC results and displayed a development of a water network that matched the DSC trends of increased thermal behaviors with increasing concentrations of water.

While the electrolytes are commonly studied at room temperature, in Chapter 4.2 we presented a MD annealing simulation method to predict the glass transition temperature of neat [BMIM][I]. The annealing simulations were carried out over a temperature range of 500K to 100K in order to properly capture the glass transition. The average potential energy of the ion pairs was plotted vs temperature to identify a discontinuous point. Segments of the plot were linearly fitted to reveal a glass transition region where the slope of the fittings suddenly changes in trend. Extrapolations of the linear fits before and after the glass transition region helped to predict a glass transition temperature of -87.5^{o} C. Simulation parameters box length and annealing rate were also tested and revealed no significant changes between the parameters in the glass transition prediction results. We determined that the simulations were accurate in predicting a glass transition window and therefore calculated self-diffusion coefficients and radial distribution functions between the [BMIM][I] ions as a function of temperature. Self-diffusion coefficients show a decreasing trend as the temperature decreases and the radial distribution functions reveal a dependency on the temperature. The results of this investigation are encouraging and will be a starting point for glass transition temperature predictions in [BMIM][I]/water mixtures, further discussed in Chapter 6.1.

Finally, density function theory (DFT) methods were used to screen aminosilane ALD precursors in Chapter 4.3. The 10 precursors consisting of mono and bis amino ligands, display potential to be used in the creation of SiO_2 thin films. Using a small cluster model, we presented a reaction pathway and coordinates for selected precursor-cluster reactions. The results demonstrate a favorability for the bis-aminosilanes, however, more studies need to be carried out to confirm their viability. Reaction energies and activation energies between the cluster and precursors reveal a trend in decreasing energies with the addition of alkyl chains to the mono-aminosilanes and little change between the bis-aminosilanes. To explore the thermal stability for scale up engineering, enthalpy of formation and Gibbs free energy of formation were calculated using two thermochemical recipes, T1 and G3MP2. The results between the methods are in good agreement and suggest the T1 method can be used for the aminosilane precursors to save computation time and resources. Lastly, to expand the size of the simulations, a SiO_2 surface and mono-methylamino silane precursors system were used to test a semi-empirical tight binding XTB-GFN2 program. The geometry, containing 1,000 atoms, was optimized using the XTB-GFN2 program and revealed different structures than the cluster models. The structures were scaled down and subjected to DFT calculations to test the validity of the complexes, but unfortunately they most likely do not exist as a minima on the PES. The MD-DFT simulation was encouraging as it showed reactive trajectories for the creation of Si-H species on the surface, however, it was computationally expensive. Overall, the XTB-GFN2 program has much potential for similar systems but may not be ready for use in industry.

CHAPTER

6. PROPOSED WORK

6.1 Expansion of Ionic Liquid Glass Transition Temperature Predictions to Ionic Liquid Mixtures

Following the encouraging results of the glass transition predictions of neat imidazolium-based ionic liquids, the predictions can now be expanded to IL mixtures. IL mixtures have been extensively studied through molecular dynamics, however, to our knowledge their glass transition temperatures have not been predicted through MD approaches. Having the toolset to predict Tg of ionic liquid mixtures would allow our group to test IL mixtures without using expensive ILs extensively in Tg measurements.

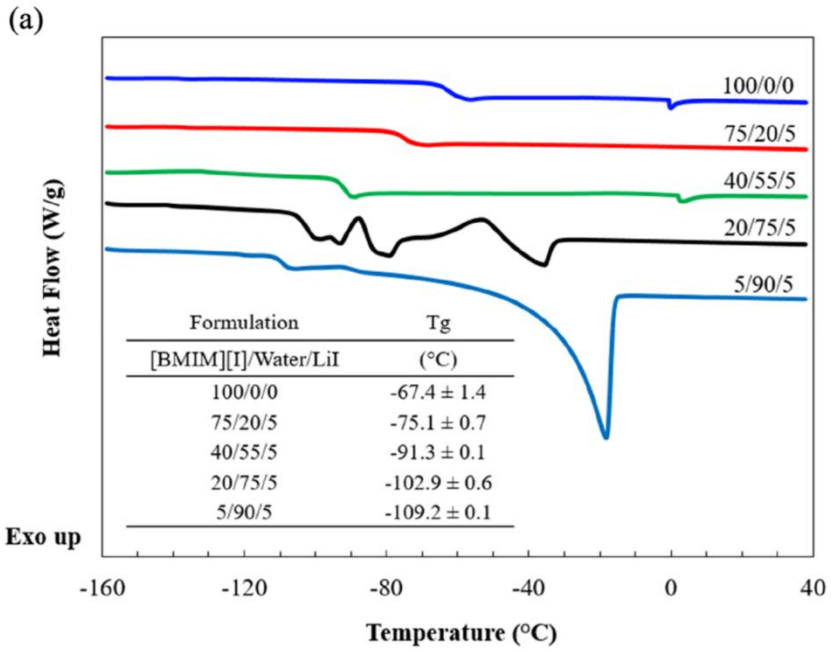

Formulation [BMIM][I]/Water/LiI	Tg (°C)
100/0/0	-67.4 ± 1.4
75/20/5	-75.1 ± 0.7
40/55/5	-91.3 ± 0.1
20/75/5	-102.9 ± 0.6
5/90/5	-109.2 ± 0.1

Figure 6.1.1: Experimentally determined Tgs of [BMIM][I]/Water/LiI mixtures and through DSC curves

To fully investigate the effects of solvents on the glass transition temperature of IL/solvent mixtures, systematic studies are carried out.[189,190,198] Figure 6.1.1 reports the

glass transition temperatures and DSC curves of [BMIM][I]/Water/LiI mixtures with increasing water concentration.[190] The purpose of the electrolyte mixtures is to be used in devices that require wide temperature windows of operation. The royal blue, red, and green DSC curves show smooth thermal behavior below 0°C and would be prime candidates for such devices. However, with increasing water concentration, the curves display changes in thermal behavior as shown in the black and dark blue curves. Again there is a shift in behavior at higher water concentrations, likely due to a development of water aggregates, however, MD simulations can be carried out to better understand the phenomena.

To further the MD glass transition temperature predictions, we will expand the systems from neat ILs to binary IL mixtures of [BMIM][I]/water. At high water concentrations, it has been experimentally determined that the mixtures tend to show crystallization before the glass transition temperature. In order to fully capture the phase behavior and determine the capabilities of the MD Tg prediction method, systematic studies of the binary IL/water mixtures will be carried out through simulation of multiple formulations. Water will be added to the neat ILs in increments of 20 mole percent. If upon further analysis, the results show inconsistencies, then the increments can be decreased to 10 mole percent.

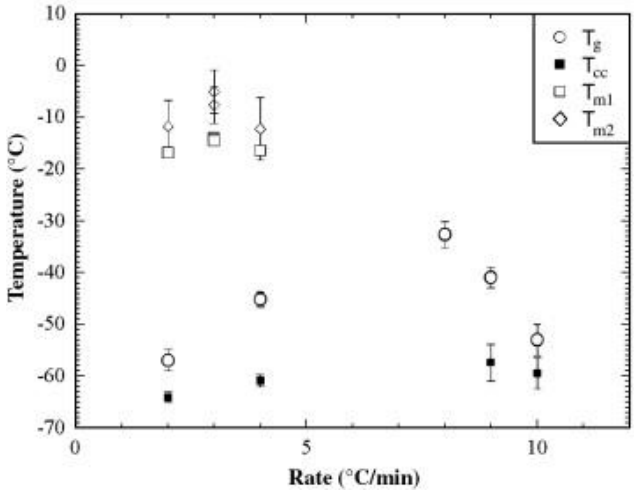

Figure 6.1.2: Tg predictions of IL/water mixture with various cooling rates

If the results of the IL/water mixtures show good Tg predictions, then the studies will be expanded to include organic solvents such as gamma-butylrolactone or butyronitrile, which have shown encouraging experimental results in lowering the glass transition temperature of [BMIM][I] based electrolyte mixtures in our lab.

The simulation parameters tested in this study, annealing rate and box length, have shown that they may be negligible when it comes to neat IL predictions, however, experimental results show that cooling rate can have an effect on the Tg Prediction of IL mixtures. Figure 6.1.1[199] shows the experimentally determined glass transition temperatures of a [DEME][BF4]/water mixture with varying cooling rates. The cooling rates have a significant influence on the Tg, and as a result, the annealing rate dependence may need to be revisited in the annealing simulations of the IL/water mixtures.

Once the annealing simulation parameters have been revisited for mixtures, the simulations will be carried out for multiple [BMIM][I]/water formulations and possibly include binary mixtures with organic solvents. While we are investigating the thermal behavior of the mixtures, it would be helpful to also predict the viscosities over the same

temperature ranges, ie. 500K to 100K. To predict the viscosities, the Einstein-Stoked relation will be used to calculate the viscosities based on the self-diffusion coefficients. The Einstein-Stokes relation states the following:

$$D = \frac{k_B T}{6\pi\eta R}$$

Where k_B is the Boltzmann constant, T is the temperature, η is the viscosity, and R is the radius of the molecule. The annealing simulations provide almost everything needed to carry out the calculation except the molecular radius. To acquire the radius, DFT calculations will be done.

6.2 Expansion of semi-empirical methods to imidazolium-based ionic liquids and their mixtures

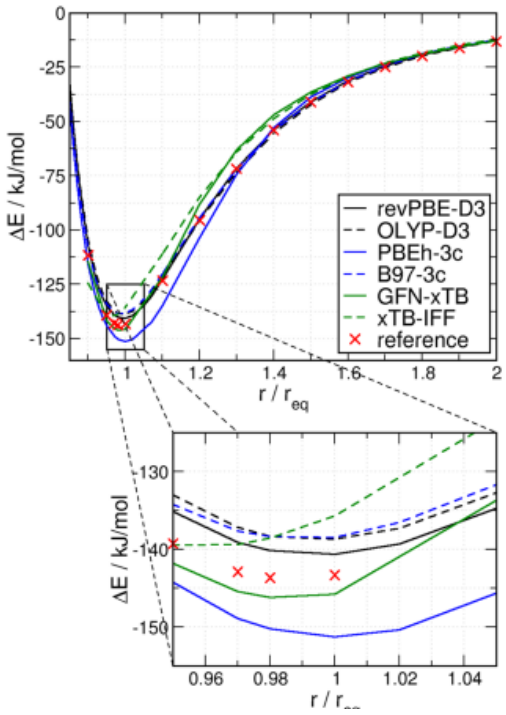

Figure 6.2.1: Interaction energies of a ethylammonium nitrate cluster studied through multiple computational approaches

To connect the ionic liquids focused projects with the atomic layer deposition project, we propose utilizing the same tight binding code, GFN2-XTB to simulate the imidazolium ionic liquids and mixtures. This offers another scale of simulations to examine between *ab-initio*, DFT, and MD results. There have been few reports on the use of XTB-GFN on ionic liquids, however, one study from Perlt et. al. gives encouraging results that the code works well for ILs. Figure 6.2.1[200] shows the interaction energy of an ethylammonium cluster model through various computational method approaches. GFN-xTB is represented by the solid green line and proves comparable to the reference in red xs.

Implementation of the XTB-GFN2 code will start with geometry optimizations of individual molecules and ion pairs. From there, short simulations of 30ps can be carried out where the results will be compared against reported *ab-initio* and DFT results. Once the method is validated, more ionic liquid pairs can be added to the systems and other solvent molecular such as water or organic solvents. The addition of solvents offers an in-depth investigation of the mixtures where the results can be compared to the MD simulations and give further insight.

REFERENCES

1. Zhang S, Zhang J, Zhang Y, Deng Y. Nanoconfined Ionic Liquids. *Chem Rev*. 2017;117(10):6755-6833. doi:10.1021/acs.chemrev.6b00509

2. Decreton M, Shikama T, Hodgson E. Performance of functional materials and components in a fusion reactor: The issue of radiation effects in ceramics and glass materials for diagnostics. In: *Journal of Nuclear Materials*. Vol 329-333. North-Holland; 2004:125-132. doi:10.1016/j.jnucmat.2004.04.012

3. Böttcher H, Soltmann U, Mertig M, Pompe W. Biocers: Ceramics with incorporated microorganisms for biocatalytic, biosorptive and functional materials development. *J Mater Chem*. 2004;14(14):2176-2188. doi:10.1039/b401724b

4. Zirkl M, Sawatdee A, Helbig U, et al. An all-printed ferroelectric active matrix sensor network based on only five functional materials forming a touchless control interface. *Adv Mater*. 2011;23(18):2069-2074. doi:10.1002/adma.201100054

5. Akiyama M, Morofuji Y, Kamohara T, et al. Preparation of oriented aluminum nitride thin films on polyimide films and piezoelectric response with high thermal stability and flexibility. *Adv Funct Mater*. 2007;17(3):458-462. doi:10.1002/adfm.200600098

6. Ramadan KS, Sameoto D, Evoy S. A review of piezoelectric polymers as functional materials for electromechanical transducers. *Smart Mater Struct*. 2014;23(3):033001. doi:10.1088/0964-1726/23/3/033001

7. Greiner A, Wendorff JH. Functional self-assembled nanofibers by electrospinning. *Adv Polym Sci*. 2008;219(1):107-171. doi:10.1007/12_2008_146

8. Agarwal S, Greiner A, Wendorff JH. Functional materials by electrospinning of polymers. *Prog Polym Sci*. 2013;38(6):963-991. doi:10.1016/j.progpolymsci.2013.02.001

9. Gatabi J, Lyon K, Rahman S, et al. Functional materials integrated on III-V semiconductors. *Microelectron Eng*. 2015;147:117-121. doi:10.1016/j.mee.2015.04.050

10. Ekiz MS, Cinar G, Khalily MA, Guler MO. Self-assembled peptide nanostructures for functional materials. *Nanotechnology*. 2016;27(40). doi:10.1088/0957-4484/27/40/402002

11. Eakins GL, Pandey R, Wojciechowski JP, et al. Functional Organic Semiconductors Assembled via Natural Aggregating Peptides. *Adv Funct Mater*. 2015;25(35):5640-5649. doi:10.1002/adfm.201502255

12. Mizoshita N, Tani T, Inagaki S. Highly conductive organosilica hybrid films prepared from a liquid-crystal perylene bisimide precursor. *Adv Funct Mater*. 2011;21(17):3291-3296. doi:10.1002/adfm.201100444

13. Jie W, Hao J. Graphene-based hybrid structures combined with functional materials of ferroelectrics and semiconductors. *Nanoscale*. 2014;6(12):6346-6362.

doi:10.1039/c3nr06918d

14. Adamo C. Tuning of structural and magnetic properties of nitronyl nitroxides by the environment. A combined experimental and computational study. *J Phys Chem A*. 1999;103(18):3481-3488. doi:10.1021/jp983825s

15. Agrawal S, Pastore M, Marotta G, Reddy MA, Chandrasekharam M, De Angelis F. Optical properties and aggregation of phenothiazine-based dye-sensitizers for solar cells applications: A combined experimental and computational investigation. *J Phys Chem C*. 2013;117(19):9613-9622. doi:10.1021/jp4026305

16. Vijayakumar M, Schwenzer B, Shutthanandan V, Hu JZ, Liu J, Aksay IA. Elucidating graphene-ionic liquid interfacial region: A combined experimental and computational study. *Nano Energy*. 2014;3:152-158. doi:10.1016/j.nanoen.2012.09.014

17. Mehio N, Lashely MA, Nugent JW, et al. Acidity of the amidoxime functional group in aqueous solution: A combined experimental and computational study. *J Phys Chem B*. 2015;119(8):3567-3576. doi:10.1021/jp512778x

18. Tong AHY, Drees B, Nardelli G, et al. A combined experimental and computational strategy to define protein interaction networks for peptide recognition modules. *Science (80-)*. 2002;295(5553):321-324. doi:10.1126/science.1064987

19. Gronau G, Krishnaji ST, Kinahan ME, et al. A review of combined experimental and computational procedures for assessing biopolymer structure-process-property relationships. *Biomaterials*. 2012;33(33):8240-8255. doi:10.1016/j.biomaterials.2012.06.054

20. Feng X, Chien P-H, Zhu Z, et al. Studies of Functional Defects for Fast Na-Ion Conduction in $Na_{3-y}PS_{4-x}Cl_x$ with a Combined Experimental and Computational Approach. *Adv Funct Mater*. 2019;29(9):1807951. doi:10.1002/adfm.201807951

21. Schleder GR, Padilha ACM, Acosta CM, Costa M, Fazzio A. From DFT to machine learning: recent approaches to materials science–a review. *J Phys Mater*. 2019;2(3):032001. doi:10.1088/2515-7639/ab084b

22. Yoon G, Kim D-H, Park I, et al. Using First-Principles Calculations for the Advancement of Materials for Rechargeable Batteries. *Adv Funct Mater*. 2017;27(40):1702887. doi:10.1002/adfm.201702887

23. Walsh A, Chen S, Wei SH, Gong XG. Kesterite thin-film solar cells: Advances in materials modelling of Cu 2 ZnSnS 4. *Adv Energy Mater*. 2012;2(4):400-409. doi:10.1002/aenm.201100630

24. Grew KN, Chiu WKS. A review of modeling and simulation techniques across the length scales for the solid oxide fuel cell. *J Power Sources*. 2012;199:1-13. doi:10.1016/j.jpowsour.2011.10.010

25. Wu L, Liu L, Wang Y, et al. A machine learning-based method to design modular

metamaterials. *Extrem Mech Lett*. 2020;36:100657. doi:10.1016/j.eml.2020.100657

26. Thangavel R, Kannan AG, Ponraj R, Thangavel V, Kim DW, Lee YS. High-energy green supercapacitor driven by ionic liquid electrolytes as an ultra-high stable next-generation energy storage device. *J Power Sources*. 2018;383:102-109. doi:10.1016/j.jpowsour.2018.02.037

27. Balducci A. Electrolytes for high voltage electrochemical double layer capacitors: A perspective article. *J Power Sources*. 2016;326:534-540. doi:10.1016/j.jpowsour.2016.05.029

28. Singh V V., Nigam AK, Batra A, Boopathi M, Singh B, Vijayaraghavan R. Applications of Ionic Liquids in Electrochemical Sensors and Biosensors. *Int J Electrochem*. 2012;2012:1-19. doi:10.1155/2012/165683

29. Arbizzani C, Biso M, Cericola D, Lazzari M, Soavi F, Mastragostino M. Safe, high-energy supercapacitors based on solvent-free ionic liquid electrolytes. *J Power Sources*. 2008;185(2):1575-1579. doi:10.1016/j.jpowsour.2008.09.016

30. Deng T, Chen D, Chen J, Sun Z, Li G, Wang J. Microelectromechanical Systems-Based Electrochemical Seismic Sensors with Insulating Spacers Integrated Electrodes for Planetary Exploration. *IEEE Sens J*. 2016;16(3):650-653. doi:10.1109/JSEN.2015.2491783

31. Li G, Wang J, Chen D, Xing Y, Chen J. The effect of electrolyte concentration on the characteristics of MEMS based electrochemical seismic sensors. In: *2015 IEEE SENSORS - Proceedings*. Institute of Electrical and Electronics Engineers Inc.; 2015. doi:10.1109/ICSENS.2015.7370402

32. Yu H, Garnero E, Fouch M. *Molecular Electronic Transducers Based Micro-Seismometers for Planetary Exploration*.

33. Huang H, Carande B, Tang R, et al. A micro seismometer based on molecular electronic transducer technology for planetary exploration. *Appl Phys Lett*. 2013;102(19):193512. doi:10.1063/1.4806983

34. Pilania G, R. Whittle K, Jiang C, et al. Using Machine Learning To Identify Factors That Govern Amorphization of Irradiated Pyrochlores. *Chem Mater*. 2017;29(6):2574-2583. doi:10.1021/acs.chemmater.6b04666

35. Zhang Y, J. Miller G, P. T. Fokwa B. Computational Design of Rare-Earth-Free Magnets with the Ti3Co5B2-Type Structure. *Chem Mater*. 2017;29(6):2535-2541. doi:10.1021/acs.chemmater.6b04114

36. A. Miller S, Gorai P, R. Ortiz B, et al. Capturing Anharmonicity in a Lattice Thermal Conductivity Model for High-Throughput Predictions. *Chem Mater*. 2017;29(6):2494-2501. doi:10.1021/acs.chemmater.6b04179

37. Chattopadhyaya M, Hermann J, Poltavsky I, Tkatchenko A. Tuning Intermolecular Interactions with Nanostructured Environments. *Chem Mater*. 2016;29(6):2452-2458. doi:10.1021/acs.chemmater.6b04190

38. He J, Franchini C, M. Rondinelli J. Ferroelectric Oxides with Strong Visible-Light Absorption from Charge Ordering. *Chem Mater*. 2016;29(6):2445-2451. doi:10.1021/acs.chemmater.6b03486

39. Li L, Long R, Prezhdo O V. Charge Separation and Recombination in Two-Dimensional MoS2/WS2: Time-Domain ab Initio Modeling. *Chem Mater*. 2017;29(6):2466-2473. doi:10.1021/acs.chemmater.6b03727

40. Eliad L, Salitra G, Soffer A, Aurbach D. Ion sieving effects in the electrical double layer of porous carbon electrodes: Estimating effective ion size in electrolytic solutions. *J Phys Chem B*. 2001;105(29):6880-6887. doi:10.1021/jp010086y

41. Li W, Peng Q, Ma H, et al. Theoretical Investigations on the Roles of Intramolecular Structure Distortion versus Irregular Intermolecular Packing in Optical Spectra of 6T Nanoparticles. *Chem Mater*. 2017;29(6):2513-2520. doi:10.1021/acs.chemmater.6b04210

42. Griffin SM, Reidulff M, Selbach SM, Spaldin NA. Defect Chemistry as a Crystal Structure Design Parameter: Intrinsic Point Defects and Ga Substitution in InMnO3. *Chem Mater*. 2017;29(6):2425-2434. doi:10.1021/acs.chemmater.6b04207

43. Zhang Y, Miller GJ, Fokwa BPT. Computational Design of Rare-Earth-Free Magnets with the Ti3Co5B2-Type Structure. *Chem Mater*. 2017;29(6):2535-2541. doi:10.1021/acs.chemmater.6b04114

44. Leung K. First-Principles Modeling of Mn(II) Migration above and Dissolution from LixMn2O4 (001) Surfaces. *Chem Mater*. 2017;29(6):2550-2562. doi:10.1021/acs.chemmater.6b04429

45. Pilania G, Whittle KR, Jiang C, et al. Using Machine Learning to Identify Factors That Govern Amorphization of Irradiated Pyrochlores. *Chem Mater*. 2017;29(6):2574-2583. doi:10.1021/acs.chemmater.6b04666

46. Troppenz M, Rigamonti S, Draxl C. Predicting Ground-State Configurations and Electronic Properties of the Thermoelectric Clathrates Ba8AlxSi46-x and Sr8AlxSi46-x. *Chem Mater*. 2017;29(6):2414-2424. doi:10.1021/acs.chemmater.6b05027

47. Miklitz M, Turcani L, Greenaway RL, Jelfs KE. Computational discovery of molecular C60 encapsulants with an evolutionary algorithm. *Commun Chem*. 2020;3(1). doi:10.1038/s42004-020-0255-8

48. Friederich P, Fediai A, Kaiser S, Konrad M, Jung N, Wenzel W. Toward Design of Novel Materials for Organic Electronics. *Adv Mater*. 2019;31(26). doi:10.1002/adma.201808256

49. Brédas JL, Persson K, Seshadri R. Computational Design of Functional Materials. *Chem Mater*. 2017;29(6):2399-2401. doi:10.1021/acs.chemmater.7b00990

50. Zäh D, Miehe C. Computational homogenization in dissipative electro-mechanics of functional materials. *Comput Methods Appl Mech Eng*. 2013;267:487-510.

doi:10.1016/j.cma.2013.09.012

51. Mishra AK, Roldan A, De Leeuw NH. A density functional theory study of the adsorption behaviour of CO2 on Cu2O surfaces. *J Chem Phys*. 2016;145(4). doi:10.1063/1.4958804

52. Tracey DF, Delley B, McKenzie DR, Warschkow O. Molecular adsorption on silicon (001): A systematic evaluation of size effects in slab and cluster models. *AIP Adv*. 2013;3(4):042117. doi:10.1063/1.4802837

53. Alberi K, Nardelli MB, Zakutayev A, et al. The 2019 materials by design roadmap. *J Phys D Appl Phys*. 2018;52(1):13001. doi:10.1088/1361-6463/aad926

54. Multiscale Modeling of Clays | Andrew J. Whittle's Research Group. Accessed October 7, 2020. https://ajw-group.mit.edu/multiscale-modeling-clays

55. Research | Fang Liu's Homepage. Accessed October 7, 2020. https://fangliu.mit.edu/research

56. Ramachandran KI, Deepa G, Namboori K. *Computational Chemistry and Molecular Modeling*. Springer; 2008.

57. Schneider R, Sharma AR, Rai A. Introduction to Molecular Dynamics. *Springer*. 2008;(739):3-40.

58. Blinder S., House JE. *Mathematical Physics in Theoretical Chemistry*. Elsevier; 2019.

59. McQuarrie D. *Quantum Chemistry*. University Science Books; 1983.

60. Singh J. *Quantum Mechanics*. Wiley; 1996. doi:10.1002/9783527618194

61. Sherrill DC. The Born-Oppenheimer Approximation. Georgia Institute of Technology. Published 2005. Accessed October 15, 2020. http://vergil.chemistry.gatech.edu/notes/bo/bo.html

62. Shavitt I. *Methods of Electronic Structure Theory*. Springer US; 1977. doi:10.1007/978-1-4757-0887-5

63. Sherrillt D, Schaefer HF, Sherrill CD, Schaefer HF. *A The Configuration Interaction Method: Advances in Highly Correlated Approaches*. Vol 34. doi:10.1016/S0065-3276(08)60535-3

64. Sherrill CD. *General Introduction to Electronic Structure Theory*. Accessed October 15, 2020. www.nobelprize.org

65. The Sherrill Group: Notes. Accessed October 15, 2020. http://vergil.chemistry.gatech.edu/notes/

66. Crystal Structure Prediction and its Application in Earth and Materials Sciences: Quantum simulation and density functional theory. Accessed October 15, 2020. http://www.physics.unlv.edu/~qzhu/qzhu-thesis/sect0020.html

67. Zhang X, Zhao Y, Hu S, et al. Electrochemical Reduction of Carbon Dioxide to

Formic Acid in Ionic Liquid [Emim][N(CN)2]/Water System. *Electrochim Acta*. 2017;247:281-287. doi:10.1016/j.electacta.2017.06.112

68. Papageorgiou N, Athanassov Y, Armand M, et al. The Performance and Stability of Ambient Temperature Molten Salts for Solar Cell Applications. *J Electrochem Soc*. 1996;143(10):3099-3108. doi:10.1149/1.1837171

69. Kawano R, Matsui H, Matsuyama C, et al. High performance dye-sensitized solar cells using ionic liquids as their electrolytes. *J Photochem Photobiol A Chem*. 2004;164(1-3):87-92. doi:10.1016/j.jphotochem.2003.12.019

70. Dossi N, Toniolo R, Pizzariello A, et al. An electrochemical gas sensor based on paper supported room temperature ionic liquids. *Lab Chip*. 2012;12(1):153-158. doi:10.1039/c1lc20663j

71. Wei D, Ivaska A. Applications of ionic liquids in electrochemical sensors. *Anal Chim Acta*. 2008;607(2):126-135. doi:10.1016/j.aca.2007.12.011

72. Fernicola A, Scrosati B, Ohno H. Potentialities of ionic liquids as new electrolyte media in advanced electrochemical devices. *Ionics (Kiel)*. 2006;12(2):95-102. doi:10.1007/s11581-006-0023-5

73. HAGIWARA R, LEE JS. Ionic Liquids for Electrochemical Devices. *Electrochemistry*. 2007;75(1):23-34. doi:10.5796/electrochemistry.75.23

74. Watanabe M, Thomas ML, Zhang S, Ueno K, Yasuda T, Dokko K. Application of Ionic Liquids to Energy Storage and Conversion Materials and Devices. *Chem Rev*. 2017;117(10):7190-7239. doi:10.1021/acs.chemrev.6b00504

75. Macfarlane DR, Forsyth M, Howlett PC, et al. Ionic liquids in electrochemical devices and processes: Managing interfacial electrochemistry. *Acc Chem Res*. 2007;40(11):1165-1173. doi:10.1021/ar7000952

76. Lu W, Fadeev AG, Qi B, et al. Use of ionic liquids for π-conjugated polymer electrochemical devices. *Science (80-)*. 2002;297(5583):983-987. doi:10.1126/science.1072651

77. Amino Acid Based Chiral Ionic Liquids as Potential GC Stationary Phases - 2011 - Wiley Analytical Science. Accessed September 27, 2020. https://analyticalscience.wiley.com/do/10.1002/gitlab.4946/full/

78. Köddermann T, Paschek D, Ludwig R. Ionic liquids: Dissecting the enthalpies of vaporization. *ChemPhysChem*. 2008;9(4):549-555. doi:10.1002/cphc.200700814

79. Mejri R, Dias JC, Besbes Hentati S, et al. Imidazolium-based ionic liquid type dependence of the bending response of polymer actuators. *Eur Polym J*. 2016;85:445-451. doi:10.1016/j.eurpolymj.2016.10.052

80. Androulaki E, Vergadou N, Economou IG. Analysis of the heterogeneous dynamics of imidazolium-based [Tf2N-] ionic liquids using molecular simulation. *Mol Phys*. 2014;112(20):2694-2706. doi:10.1080/00268976.2014.906670

81. Bonĥte P, Dias AP, Papageorgiou N, Kalyanasundaram K, Grätzel M. Hydrophobic, Highly Conductive Ambient-Temperature Molten Salts. *Inorg Chem*. 1996;35(5):1168-1178. doi:10.1021/ic951325x

82. Guan W, Chang N, Yang L, Bu X, Wei J, Liu Q. Determination and Prediction for the Polarity of Ionic Liquids. *J Chem Eng Data*. 2017;62(9):2610-2616. doi:10.1021/acs.jced.7b00082

83. Binetti E, Panniello A, Triggiani L, et al. Spectroscopic study on imidazolium-based ionic liquids: Effect of alkyl chain length and anion. *J Phys Chem B*. 2012;116(11):3512-3518. doi:10.1021/jp300517h

84. Moosavi M, Daneshvar A. Investigation of the rheological properties of two imidazolium-based ionic liquids. *J Mol Liq*. 2014;190:59-67. doi:10.1016/j.molliq.2013.10.024

85. Mukherjee I, Manna K, Dinda G, Ghosh S, Moulik SP. Shear- and temperature-dependent viscosity behavior of two phosphonium-based ionic liquids and surfactant triton X-100 and their biocidal activities. *J Chem Eng Data*. 2012;57(5):1376-1386. doi:10.1021/je200938k

86. Burrell GL, Dunlop NF, Separovic F. Non-Newtonian viscous shear thinning in ionic liquids. *Soft Matter*. 2010;6(9):2080-2086. doi:10.1039/b916049n

87. Jin H, O'Hare B, Dong J, et al. Physical properties of ionic liquids consisting of the 1-butyl-3- methylimidazolium cation with various anions and the bis(trifluoromethylsulfonyl)imide anion with various cations. *J Phys Chem B*. 2008;112(1):81-92. doi:10.1021/jp076462h

88. Harris KR, Kanakubo M, Woolf LA. Temperature and pressure dependence of the viscosity of the ionic liquids 1-hexyl-3-methylimidazolium hexafluorophosphate and 1-butyl-3-methylimidazolium BiS(trifluoromethylsulfonyl)imide. *J Chem Eng Data*. 2007;52(3):1080-1085. doi:10.1021/je700032n

89. Harris KR, Kanakubo M, Woolf LA. Temperature and pressure dependence of the viscosity of the ionic liquids 1-methyl-3-octylimidazolium hexafluorophosphate and 1-methyl-3-octylimidazolium tetrafluoroborate. *J Chem Eng Data*. 2006;51(3):1161-1167. doi:10.1021/je060082s

90. Galán Sánchez LM, Espel JR, Onink F, Meindersma GW, De Haan AB. Density, viscosity, and surface tension of synthesis grade imidazolium,pyridinium, and pyrrolidinium based room temperature ionic liquids. *J Chem Eng Data*. 2009;54(10):2803-2812. doi:10.1021/je800710p

91. Tsunashima K, Kawabata A, Matsumiya M, et al. Low viscous and highly conductive phosphonium ionic liquids based on bis(fluorosulfonyl)amide anion as potential electrolytes. *Electrochem commun*. 2011;13(2):178-181. doi:10.1016/j.elecom.2010.12.007

92. Pereiro AB, Legido JL, Rodríguez A. Physical properties of ionic liquids based on 1-alkyl-3-methylimidazolium cation and hexafluorophosphate as anion and

temperature dependence. *J Chem Thermodyn*. 2007;39(8):1168-1175. doi:10.1016/j.jct.2006.12.005

93. P. Fredlake C, M. Crosthwaite J, G. Hert D, N. V. K. Aki S, F. Brennecke J. Thermophysical Properties of Imidazolium-Based Ionic Liquids. *J Chem & Eng Data*. 2004;49(4):954-964. doi:10.1021/je034261a

94. Moganty SS, Chinthamanipeta PS, Vendra VK, Krishnan S, Baltus RE. Structure-property relationships in transport and thermodynamic properties of imidazolium bistriflamide ionic liquids for CO2 capture. *Chem Eng J*. 2014;250:377-389. doi:10.1016/j.cej.2014.04.010

95. Xue L, Gurung E, Tamas G, et al. Effect of Alkyl Chain Branching on Physicochemical Properties of Imidazolium-Based Ionic Liquids. Published online 2016. doi:10.1021/acs.jced.5b00658

96. Doherty B, Zhong X, Gathiaka S, Li B, Acevedo O. Revisiting OPLS Force Field Parameters for Ionic Liquid Simulations. *J Chem Theory Comput*. 2017;13(12):6131-6135. doi:10.1021/acs.jctc.7b00520

97. Doherty B, Zhong X, Acevedo O. Virtual Site OPLS Force Field for Imidazolium-Based Ionic Liquids. *J Phys Chem B*. 2018;122(11):2962-2974. doi:10.1021/acs.jpcb.7b11996

98. Doherty B, Acevedo O. OPLS Force Field for Choline Chloride-Based Deep Eutectic Solvents. *J Phys Chem B*. 2018;122(43):9982-9993. doi:10.1021/acs.jpcb.8b06647

99. V. Sambasivarao S, Acevedo O. Development of OPLS-AA Force Field Parameters for 68 Unique Ionic Liquids. *J Chem Theory Comput*. 2009;5(4):1038-1050. doi:10.1021/ct900009a

100. Bhargava BL, Balasubramanian SS. Refined potential model for atomistic simulations of ionic liquid. *J Chem Phys*. 2007;127:114510. doi:10.1063/1.2772268

101. Lopes JNC, Pádua AAH. Molecular Force Field for Ionic Liquids Composed of Triflate or Bistriflylimide Anions. Published online 2004. doi:10.1021/jp0476545

102. Canongia Lopes JN, Deschamps J, Pádua AAH. Modeling Ionic Liquids Using a Systematic All-Atom Force Field. *J Phys Chem B*. 2004;108(6):2038-2047. doi:10.1021/jp0362133

103. Youngs TGA, Del Pópolo MG, Kohanoff J. Development of complex classical force fields through force matching to ab initio data: Application to a room-temperature ionic liquid. *J Phys Chem B*. 2006;110(11):5697-5707. doi:10.1021/jp056931k

104. Feng G, Chen M, Bi S, et al. Free and Bound States of Ions in Ionic Liquids, Conductivity, and Underscreening Paradox. *Phys Rev X*. 2019;9(2). doi:10.1103/PhysRevX.9.021024

105. Kowsari MH, Alavi S, Ashrafizaadeh M, Najafi B. Molecular dynamics simulation of imidazolium-based ionic liquids. I. Dynamics and diffusion coefficient. *J Chem Phys*. 2008;129(22):224508. doi:10.1063/1.3035978

106. Fakhraee M, Zandkarimi B, Salari H, Gholami MR. Hydroxyl-functionalized 1-(2-hydroxyethyl)-3-methyl imidazolium ionic liquids: Thermodynamic and structural properties using molecular dynamics simulations and ab initio calculations. *J Phys Chem B*. 2014;118(49):14410-14428. doi:10.1021/jp5083714

107. Troncoso J, Cerdeiriña CA, Sanmamed YA, Romaní L, Rebelo LPN. Thermodynamic properties of imidazolium-based ionic liquids: Densities, heat capacities, and enthalpies of fusion of [bmim][PF6] and [bmim][NTf2]. *J Chem Eng Data*. 2006;51(5):1856-1859. doi:10.1021/je060222y

108. Nickerson SD, Nofen EM, Chen H, et al. A Combined Experimental and Molecular Dynamics Study of Iodide-Based Ionic Liquid and Water Mixtures. *J Phys Chem B*. 2015;119(28):8764-8772. doi:10.1021/acs.jpcb.5b04020

109. S. Frost D, Machas M, Perea B, L. Dai L. Nonconvective Mixing of Miscible Ionic Liquids. *Langmuir*. 2013;29(32):10159-10165. doi:10.1021/la402158n

110. Johnson RW, Hultqvist A, Bent SF. A brief review of atomic layer deposition: From fundamentals to applications. *Mater Today*. 2014;17(5):236-246. doi:10.1016/j.mattod.2014.04.026

111. Oviroh PO, Akbarzadeh R, Pan D, Coetzee RAM, Jen TC. New development of atomic layer deposition: processes, methods and applications. *Sci Technol Adv Mater*. 2019;20(1):465-496. doi:10.1080/14686996.2019.1599694

112. Pakkala A, Putkonen M. Chapter 8 - Atomic Layer Deposition. In: Martin PMBT-H of DT for F and C (Third E, ed. William Andrew Publishing; 2010:364-391. doi:https://doi.org/10.1016/B978-0-8155-2031-3.00008-9

113. Muneshwar T, Miao M, Borujeny ER, Cadien K. Atomic Layer Deposition: Fundamentals, Practice, and Challenges. In: *Handbook of Thin Film Deposition: Fourth Edition*. Elsevier; 2018:359-377. doi:10.1016/B978-0-12-812311-9.00011-6

114. Kim H. Atomic layer deposition of metal and nitride thin films: Current research efforts and applications for semiconductor device processing. *J Vac Sci Technol B Microelectron Nanom Struct*. 2003;21(6):2231. doi:10.1116/1.1622676

115. Lichty P, Liang X, Muhich C, Evanko B, Bingham C, Weimer AW. Atomic layer deposited thin film metal oxides for fuel production in a solar cavity reactor. *Int J Hydrogen Energy*. 2012;37(22):16888-16894. doi:10.1016/j.ijhydene.2012.08.004

116. Wang X, Yushin GN. Chemical vapor deposition and atomic layer deposition for advanced lithium ion batteries and supercapacitors. *Energy Environ Sci*. 2015;8:1889-1904.

117. Lucovsky G, Tsu D V. Plasma enhanced chemical vapor deposition: Differences between direct and remote plasma excitation. *J Vac Sci Technol A Vacuum,*

Surfaces, Film. 1987;5(4):2231-2238. doi:10.1116/1.574963

118. Wild C, Wagner J, Koidl P. Process monitoring of a -C:H plasma deposition . *J Vac Sci Technol A Vacuum, Surfaces, Film*. 1987;5(4):2227-2230. doi:10.1116/1.574962

119. Hatanpää T, Ritala M, Leskelä M. Precursors as enablers of ALD technology: Contributions from university of helsinki. *Coord Chem Rev*. 2013;257(23-24):3297-3322. doi:10.1016/j.ccr.2013.07.002

120. Schiller S, Beister G, Heisig U, Foerster H. High-rate vapor deposition and large systems for coating processes. *J Vac Sci Technol A Vacuum, Surfaces, Film*. 1987;5(4):2239-2245. doi:10.1116/1.574964

121. Remes Z, Vanecek M, Yates HM, Evans P, Sheel DW. Optical properties of SnO2:F films deposited by atmospheric pressure CVD. *Thin Solid Films*. 2009;517:6287-6289. doi:10.1016/j.tsf.2009.02.109

122. Sathasivam S, Kafizas A, Ponja S, et al. Combinatorial Atmospheric Pressure CVD of a Composite TiO2/SnO2 Thin Film. *Chem Vap Depos*. 2014;20(1-2-3):69-79. doi:10.1002/cvde.201307081

123. Abedi M, Abdollah-zadeh A, Bestetti M, Vicenzo A, Serafini A, Movassagh-Alanagh F. The effects of phase transformation on the structure and mechanical properties of TiSiCN nanocomposite coatings deposited by PECVD method. *Appl Surf Sci*. 2018;444:377-386. doi:https://doi.org/10.1016/j.apsusc.2018.02.263

124. Ovanesyan RA, Filatova EA, Elliott SD, Hausmann DM, Smith DC, Agarwal S. Atomic layer deposition of silicon-based dielectrics for semiconductor manufacturing: Current status and future outlook. *J Vac Sci Technol A*. 2019;37(6):60904. doi:10.1116/1.5113631

125. Glocker David A. RS V. *No Title*. John Wiley & Sons; 2016. https://app.knovel.com/hotlink/toc/id:kpMCDT0002/medical-coatings-deposition/medical-coatings-deposition

126. Meyer-Friedrichsen T, Elschner A, Keohan F, Lövenich W, Ponomarenko S. Conductors and semiconductors for advanced organic electronics. *Proc SPIE - Int Soc Opt Eng*. Published online August 1, 2009:1. doi:10.1117/12.826270

127. Kim H, Lee H-B-R, Maeng W-J. Applications of atomic layer deposition to nanofabrication and emerging nanodevices. *Thin Solid Films*. 2009;517(8):2563-2580. doi:https://doi.org/10.1016/j.tsf.2008.09.007

128. Johnson AL, Parish JD. Recent developments in molecular precursors for atomic layer deposition. *ACS Symp Ser*. 2018;1311:1-53. doi:10.1039/9781788010672-00001

129. Sherman A. Atomic layer deposition for nanotechnology: an enabling process for nanotechnology fabrication. Published online 2008.

130. Kääriäinen T, Cameron D, Kääriäinen M, Sherman A. *Atomic Layer Deposition:*

Principles, Characteristics, and Nanotechnology Applications.; 2013. Accessed October 1, 2020. https://books.google.com/books?hl=en&lr=&id=gTrGuGJ8cgwC&oi=fnd&pg=PA2008&ots=XFKCOgpoqi&sig=bW6gBnlANO1k6zohmTtw1Zu0v7o

131. Pinna N, Knez M, WILEY-VCH Verlag GmbH gc Co KGaA W. *Atomic Layer Deposition of Nanostructured Materials*.; 2012. Accessed October 1, 2020. https://books.google.com/books?hl=en&lr=&id=r7G4BwAAQBAJ&oi=fnd&pg=PR5&ots=w7XztH6Q7Y&sig=J5A0TYLjNoE6Xe_F9h8AxEdQD1Y

132. Fang G, Xu L, Cao Y, Li A. Theoretical design and computational screening of precursors for atomic layer deposition. *Coord Chem Rev*. 2016;322:94-103. doi:10.1016/j.ccr.2016.05.011

133. Hausmann D, Becker J, Wang S, Gordon RG. Rapid vapor deposition of highly conformal silica nanolaminates. *Science (80-)*. 2002;298(5592):402-406. doi:10.1126/science.1073552

134. Hirose F, Kinoshita Y, Shibuya S, et al. Atomic layer deposition of SiO2 from Tris(dimethylamino)silane and ozone by using temperature-controlled water vapor treatment. *Thin Solid Films*. 2010;519(1):270-275. doi:10.1016/j.tsf.2010.07.107

135. Fang GY, Xu LN, Cao YQ, Wang LG, Wu D, Li AD. Self-catalysis by aminosilanes and strong surface oxidation by O2 plasma in plasma-enhanced atomic layer deposition of high-quality SiO2. *Chem Commun*. 2015;51(7):1341-1344. doi:10.1039/c4cc08004a

136. Yang JH, Baek S Bin, Kim YC. Initial surface reaction of di-isopropylaminosilane on a fully hydroxyl-terminated Si (001) surface. *J Nanosci Nanotechnol*. 2014;14(10):7954-7960. doi:10.1166/jnn.2014.9474

137. Han B, Zhang Q, Wu J, et al. On the Mechanisms of SiO2 Thin-Film Growth by the Full Atomic Layer Deposition Process Using Bis(t-butylamino)silane on the Hydroxylated SiO2(001) Surface. *J Phys Chem C*. 2011;116(1):947-952. doi:10.1021/jp2094802

138. Jarosz G, Mierzwa M, Zioło J, Paluch M, Shirota H, Ngai KL. Glass transition dynamics of room-temperature ionic liquid 1-methyl-3-trimethylsilylmethylimidazolium tetrafluoroborate. *J Phys Chem B*. 2011;115(44):12709-12716. doi:10.1021/jp207291k

139. Gibbs JH, DiMarzio EA. Nature of the glass transition and the glassy state. *J Chem Phys*. 1958;28(3):373-383. doi:10.1063/1.1744141

140. Wojnarowska Z, Kołodziejczyk K, Paluch KJ, et al. Decoupling of conductivity relaxation from structural relaxation in protic ionic liquids and general properties. *Phys Chem Chem Phys*. 2013;15(23):9205-9211. doi:10.1039/c3cp50627d

141. Moura Ramos JJ, Afonso CAM, Branco LC. Glass transition relaxation and fragility in two room temperature ionic liquids. *J Therm Anal Calorim*. 2003;71(2):659-666. doi:10.1023/A:1022884716750

142. Carrete JJ, Méndezméndez-Morales T, Scar Cabeza Ó, Lynden-Bell RM, Gallego LJ, Varela LM. Investigation of the Local Structure of Mixtures of an Ionic Liquid with Polar Molecular Species through Molecular Dynamics: Cluster Formation and Angular Distributions. Published online 2012. doi:10.1021/jp301309s

143. Ghoshdastidar D, Senapati S, Festschrift BB. Nanostructural Reorganization Manifests in Sui-Generis Density Trend of Imidazolium Acetate/Water Binary Mixtures. *J Phys Chem B*. 2015;119:0. doi:10.1021/acs.jpcb.5b00433

144. Sieffert N, Wipff G. The [BMI][Tf 2 N] Ionic Liquid/Water Binary System: A Molecular Dynamics Study of Phase Separation and of the Liquid-Liquid Interface. Published online 2006. doi:10.1021/jp061849q

145. Habasaki J, Ngai KL. Rigidity and soft percolation in the glass transition of an atomistic model of ionic liquid, 1-ethyl-3-methyl imidazolium nitrate, from molecular dynamics simulations - Existence of infinite overlapping networks in a fragile ionic liquid. *J Chem Phys*. 2015;142(16):164501. doi:10.1063/1.4918586

146. Forero-Martinez NC, Cortes-Huerto R, Ballone P. The glass transition and the distribution of voids in room-temperature ionic liquids: A molecular dynamics study. *J Chem Phys*. 2012;136(20):124502. doi:10.1063/1.4723855

147. Ohlinger WS, Klunzinger PE, Deppmeier BJ, Hehre WJ. Efficient Calculation of Heats of Formation †. doi:10.1021/jp810144q

148. Ostadhossein A, Kim S-Y, Cubuk ED, Qi Y, van Duin ACT. Atomic Insight into the Lithium Storage and Diffusion Mechanism of SiO2/Al2O3 Electrodes of Lithium Ion Batteries: ReaxFF Reactive Force Field Modeling. *J Phys Chem A*. 2016;120(13):2114-2127. doi:10.1021/acs.jpca.5b11908

149. Hu X, Schuster J, Schulz SE. Multiparameter and Parallel Optimization of ReaxFF Reactive Force Field for Modeling the Atomic Layer Deposition of Copper. *J Phys Chem C*. 2017;121(50):28077-28089. doi:10.1021/acs.jpcc.7b09948

150. James M, Murtola T, Schulz R, Smith JC, Hess B, Lindahl E. GROMACS : High performance molecular simulations through multi-level parallelism from laptops to supercomputers. *Softw X*. 2015;1-2:19-25. doi:10.1016/j.softx.2015.06.001

151. Spoel D Van Der, Lindahl E, Hess B, Groenhof G. GROMACS: Fast, Flexible, and Free. *J Comput Chem*. 2005;26(16):1701–1718. doi:10.1002/jcc.20291

152. Berendsen H, Spoel D Van Der, Drunen R Van. GROMACS : A message-passing parallel molecular dynamics implementation. *Comput Phys Commun*. 1995;91:43-56.

153. Lopes NC, Deschamps J, Pa AH, Pascal B, Landes A V. Modeling Ionic Liquids Using a Systematic All-Atom Force Field. *J Phys Chem B*. 2004;108:2038-2047. doi:10.1021/jp0362133

154. Hess, B.; Henk, B.; Berendsen H. FJ. P-LINCS : A Parallel Linear Constraint Solver for Molecular Simulation. *J Comput Chem*. 1997;18:1463-1472. doi:10.1021/ct700200b

155. Hess B, Bekker H, Berendsen HJC, Fraaije JGEM. LINCS : A Linear Constraint Solver for Molecular Simulations. *J Chem Theory Comput*. 1997;4:116-122.

156. Bussi G, Donadio D, Parrinello M. Canonical sampling through velocity rescaling. *J Chem Phys*. 2007;126:014101. doi:10.1063/1.2408420

157. Berendsen HJC, Postma JPM, van Gunsteren WF, DiNola, A., Haak JR. Molecular dynamics with coupling to an external bath. *J Chem Phys*. 1984;81:3684. doi:10.1063/1.448118

158. Parrinello M, Rahman A. Polymorphic transitions in single crystals : A new molecular dynamics method. *J Appl Phys*. 1981;52:7182. doi:10.1063/1.328693

159. Humphrey W, Dalke A, Schulten K. VMD : Visual Molecular Dynamics. 1996;7855(October 1995):33-38.

160. Systems D. BIOVIA, Materials Studio, R2017, San Diego. Published online 2017. https://3ds.com/products-services/biovia/products#_ga=2.150667057.647335877.1602788749-a1fe2030-0f18-11eb-9e30-4f2b8d558f14

161. Delley B. From molecules to solids with the DMol3 approach. *J Chem Phys*. 2000;113(18):7756-7764. doi:10.1063/1.1316015

162. Delley B, Ellis DE. Efficient and accurate expansion methods for molecules in local density models. *J Chem Phys*. 1982;76(4):1949-1960. doi:10.1063/1.443168

163. Delley B. An all-electron numerical method for solving the local density functional for polyatomic molecules. *J Chem Phys*. 1990;92(1):508-517. doi:10.1063/1.458452

164. Becke AD. Density-functional thermochemistry. III. The role of exact exchange. *J Chem Phys*. 1993;98(7):5648-5652. doi:10.1063/1.464913

165. Becke AD, Dickson RM. Numerical solution of Poisson's equation in polyatomic molecules. *J Chem Phys*. 1988;89(5):2993-2997. doi:10.1063/1.455005

166. Edgecombe KE, Becke AD. Cr2 in density-functional theory: approximate spin projection. *Chem Phys Lett*. 1995;244(5-6):427-432. doi:10.1016/0009-2614(95)00945-Z

167. Becke AD. Density-functional exchange-energy approximation with correct asymptotic behavior. *Phys Rev A*. 1988;38(6):3098-3100. doi:10.1103/PhysRevA.38.3098

168. McDouall JJW, Peasley K, Robb MA. A simple MC SCF perturbation theory: Orthogonal valence bond Møller-Plesset 2 (OVB MP2). *Chem Phys Lett*. 1988;148(2-3):183-189. doi:10.1016/0009-2614(88)80296-3

169. Almlöf J. Elimination of energy denominators in Møller-Plesset perturbation theory by a Laplace transform approach. *Chem Phys Lett*. 1991;181(4):319-320. doi:10.1016/0009-2614(91)80078-C

170. Saebø S, Pulay P. Fourth-order Møller-Plessett perturbation theory in the local correlation treatment. I. Method. *J Chem Phys*. 1986;86(2):914-922. doi:10.1063/1.452293

171. Surján PR. The MP2 energy as a functional of the Hartree-Fock density matrix. *Chem Phys Lett*. 2005;406(4-6):318-320. doi:10.1016/j.cplett.2005.03.024

172. Inc. W. Spartan '18. https://www.wavefun.com/

173. Frisch, M. J.; Trucks, G. W.; Schlegel, H. B.; Scuseria, G. E.; Robb, M. A.; Cheeseman, J. R.; Scalmani, G.; Barone, V.; Mennucci, B.; Petersson, G. A.; Nakatsuji, H.; Caricato, M.; Li, X.; Hratchian, H. P.; Izmaylov, A. F.; Bloino, J.; Zheng, G.; Sonnenb DJ. Gaussian09. https://gaussian.com/glossary/g09/

174. Grimme S, Bannwarth C, Dohm S, et al. Fully Automated Quantum-Chemistry-Based Computation of Spin–Spin-Coupled Nuclear Magnetic Resonance Spectra. *Angew Chemie - Int Ed*. 2017;56(46):14763-14769. doi:10.1002/anie.201708266

175. Grimme S, Bannwarth C. Ultra-fast computation of electronic spectra for large systems by tight-binding based simplified Tamm-Dancoff approximation (sTDA-xTB). *J Chem Phys*. 2016;145(5). doi:10.1063/1.4959605

176. Bannwarth C, Ehlert S, Grimme S. GFN2-xTB - An Accurate and Broadly Parametrized Self-Consistent Tight-Binding Quantum Chemical Method with Multipole Electrostatics and Density-Dependent Dispersion Contributions. *J Chem Theory Comput*. 2019;15(3):1652-1671. doi:10.1021/acs.jctc.8b01176

177. Grimme S, Brandenburg JG, Bannwarth C, Hansen A. Consistent structures and interactions by density functional theory with small atomic orbital basis sets. *J Chem Phys*. 2015;143(5). doi:10.1063/1.4927476

178. Grimme S, Hansen A, Brandenburg JG, Bannwarth C. Dispersion-Corrected Mean-Field Electronic Structure Methods. *Chem Rev*. 2016;116(9):5105-5154. doi:10.1021/acs.chemrev.5b00533

179. Grimme S, Bannwarth C, Caldeweyher E, Pisarek J, Hansen A. A general intermolecular force field based on tight-binding quantum chemical calculations. *J Chem Phys*. 2017;147(16). doi:10.1063/1.4991798

180. Cole DJ, Vilseck JZ, Tirado-Rives J, Payne MC, Jorgensen WL. Biomolecular Force Field Parameterization via Atoms-in-Molecule Electron Density Partitioning. *J Chem Theory Comput*. 2016;12(5):2312-2323. doi:10.1021/acs.jctc.6b00027

181. Köddermann T, Paschek D, Ludwig R. Molecular dynamic simulations of ionic liquids: A reliable description of structure, thermodynamics and dynamics. *ChemPhysChem*. 2007;8(17):2464-2470. doi:10.1002/cphc.200700552

182. Liu X, Zhang S, Zhou G, Wu G, Yuan X, Yao X. New Force Field for Molecular Simulation of Guanidinium-Based Ionic Liquids. Published online 2006. doi:10.1021/jp060834p

183. Liu X, Zhou G, Zhang S, Yao X. Molecular dynamics simulation of dual amino-functionalized imidazolium-based ionic liquids. *Fluid Phase Equilib*. 2009;284(1):44-49. doi:10.1016/j.fluid.2009.06.004

184. Koishi T. Molecular Dynamics Study of the Effect of Water on Hydrophilic and Hydrophobic Ionic Liquids. *J Phys Chem B*. 2018;122:12342-12350. doi:10.1021/acs.jpcb.8b07774

185. Singh T, Kumar A. Cation-anion-water interactions in aqueous mixtures of imidazolium based ionic liquids. *Vib Spectrosc*. 2011;55(1):119-125. doi:10.1016/j.vibspec.2010.09.009

186. Moreno M, Castiglione F, Mele A, Pasqui C, Raos G. Interaction of water with the model ionic liquid [bmim][BF4]: Molecular dynamics simulations and comparison with NMR data. *J Phys Chem B*. 2008;112(26):7826-7836. doi:10.1021/jp800383g

187. Karmakar A, Chandra A. Water in Hydration Shell of an Iodide Ion: Structure and Dynamics of Solute-Water Hydrogen Bonds and Vibrational Spectral Diffusion from First-Principles Simulations. Published online 2015. doi:10.1021/jp510714e

188. Cha S, Kim D. Anion exchange in ionic liquid mixtures. *Phys Chem Chem Phys*. 2015;17(44):29786-29792. doi:10.1039/c5cp04276c

189. Gotze W, Sjogren L. Relaxation processes in supercooled liquids. *Reports Prog Phys*. 1992;55(3):241-376. doi:10.1088/0034-4885/55/3/001

190. Xu Y, Lin WJ, Gliege M, et al. A Dual Ionic Liquid Based Low-Temperature Electrolyte System. *J Phys Chem B*. 2018;122:acs.jpcb.8b08815. doi:10.1021/acs.jpcb.8b08815

191. Penev E, Kratzer P, Scheffler M. Effect of the cluster size in modeling the H2 desorption and dissociative adsorption on Si(001). *J Chem Phys*. 1999;110(8):3986-3994. doi:10.1063/1.478279

192. A. Murray C, D. Elliott S, Hausmann D, Henri J, LaVoie A. Effect of Reaction Mechanism on Precursor Exposure Time in Atomic Layer Deposition of Silicon Oxide and Silicon Nitride. *ACS Appl Mater & Interfaces*. 2014;6(13):10534-10541. doi:10.1021/am5021167

193. Huang L, Han B, Fan M, Cheng H. Design of efficient mono-aminosilane precursors for atomic layer deposition of SiO2 thin films. *RSC Adv*. 2017;7(37):22672-22678. doi:10.1039/c7ra02301d

194. Shoemaker J, Burggraf LW, Gordon MS. An ab initio cluster study of the structure of the Si(001) surface. *J Chem Phys*. 2000;112(6):2994-3005. doi:10.1063/1.480930

195. Warschkow O, McDonell TL, Marks NA. NH3 on Si(0 0 1): Can Gaussian cluster and planewave slab models agree on energetics? *Surf Sci*. 2007;601(14):3020-3033. doi:10.1016/j.susc.2007.05.017

196. Huang L, Han B, Han B, et al. Density functional theory study on the full ALD

process of silicon nitride thin film deposition via BDEAS or BTBAS and NH 3. *Phys Chem Chem Phys*. 2014;16:18501. doi:10.1039/c4cp02741h

197. Huang L, Han B, Han B, et al. First-Principles Study of a Full Cycle of Atomic Layer Deposition of SiO2 Thin Films with Di(sec-butylamino)silane and Ozone. *J Phys Chem C*. 2013;117(38):19454-19463. doi:10.1021/jp405541x

198. Triolo A, Russina O, Bleif HJ, Di Cola E. Nanoscale segregation in room temperature ionic liquids. *J Phys Chem B*. 2007;111(18):4641-4644. doi:10.1021/jp067705t

199. Inoue T, Dong B, Zheng LQ. Phase behavior of binary mixture of 1-dodecyl-3-methylimidazolium bromide and water revealed by differential scanning calorimetry and polarized optical microscopy. *J Colloid Interface Sci*. 2007;307(2):578-581. doi:10.1016/j.jcis.2006.12.063

200. Perlt E, Ray P, Hansen A, Malberg F, Grimme S, Kirchner B. Finding the best density functional approximation to describe interaction energies and structures of ionic liquids in molecular dynamics studies. *J Chem Phys*. 2018;148:193835. doi:10.1063/1.5013122